Development of a differential mobility particle sizer applied to industrial gas phase synthesis processes for nanoscaled powders

Von der Fakultät für Ingenieurwissenschaften
der Universität Duisburg-Essen
zur Erlangung des akademischen Grades eines

Doktors der Ingenieurwissenschaften

genehmigte Dissertation

von

Petra Magdalena Müschenborn
aus
Rheinhausen jetzt Duisburg

Referent: Priv. Doz. Dr.-Ing. F. E. Kruis
Korreferent: Prof. Dr. M. Winterer
Tag der mündlichen Prüfung: 26.01.2007

Content

1 Introduction

Nanotechnology is considered to be one of the key technologies of the future. In contemporary research and development the efforts towards nanoscaled structures as to their synthesis and analysis play an important role in engineering sciences. Disciplines like electrical and mechanical engineering as well as chemistry and biology, especially genetic engineering, expect innovative impulses from the skill to precisely handle dimensions in the nanometer range even down to the sizes of molecules and atoms. The intentions are to realize high functional densities for example in semiconductor technology, or to understand and to intervene in biological mechanisms, for example the channelling of medical substances through the membranes of human cells.

One of the driving forces behind the rapid development of nanotechnology is that materials show completely different physical properties when they appear as clusters of a few molecules or atoms. This phenomenon has lead to new approaches for instance in optoelectronics, because the wavelength of lasers or the characteristics of optical filters or resonators are adjustable by the particle size. Even in every day life nanotechnology has long since entered. New ceramics, lubricants, or lacquers have been created using powders with grains (particles) in the nanometer size range.

Nanoscaled particles and molecular clusters can be produced either in the liquid phase (suspensions) or in the gas phase (aerosols). Advantages of gas phase synthesis are:

- high purity
- continuous processing
- high degree of crystallinity by means of high temperature annealing
- direct control of the process
- low costs.

Gas phase synthesis in industrial scale is applied among others for the production of titanium dioxide (TiO_2), aluminium oxide (Al_2O_3), silicon dioxide (SiO_2), or carbon black (C). As powders these materials are used as pigments, adhesives, or additives for countless products (lacquers, lipsticks, toothpaste, tyres, ...). A decisive criterion for their purpose is the size of their constituting primary particles, aggregates, and agglomerates (see chapter 2.2). An example for properties of powders which depend on the particle size is the colour appearance.

In order to produce well-tailored nanoscaled powders it is necessary to understand growth and formation mechanisms of primary particles, aggregates, and agglomerates. Essential information for a profound understanding of the particle generation for different stages of the processes is the particle size distribution (PSD) (Hinds [24]).

Although for measurements of number size distributions several methods have been developed and commercial systems are available, there is none which can cope with the rather harsh conditions coming along with industrial powder production.

The subject of this thesis is the development and realization of a new system, which on the one hand is able to sample and "freeze" the product particles in the gas phase at different stages of the production process and on the other to determine the number size distribution of the sample.

In chapter 2 a closer look is taken at typical industrial processes for the production of nanoscaled powders and the measurement quantities particle size and particle number size distribution are discussed. The requirements of a new measurement system are deduced form the particular process conditions and principles for the determination of particle sizes at powder synthesis processes are introduced. It is described, why the differential mobility analysis is the most suitable to fulfil the requirements.

The theoretical basis of differential mobility analysis and the differential mobility particle sizer (DMPS) is given in chapter 3. In chapter 4 the development of a new DMPS and its experimental characterization are described. Chapter 5 describes the application of the new DMPS to three different industrial powder synthesis plants under various process conditions. A conclusion and an outlook as to future improvements in chapter 6 finish the work.

2 Powders and need of powder size characterization

2.1 Industrial gas phase synthesis processes for powders in the nanometer size range

Powders are very important materials which function as source material or additive for a number of highly mechanized products. Actually more than 60% of chemical products are in form of powders. An outstanding role play oxides like TiO_2, Al_2O_3, or SiO_2. The list of applications is very long. TiO_2 is used for example as pigments, additive for sun blockers, or material for optoelectronic devices. Al_2O_3 is a raw material for tailored ceramic products. SiO_2 is used as source material for electronic devices as well as for toothpaste or for example as additive to adjust many properties like the shear- and tensile modules of polymers, the rheology of powders and liquids, etc., to name only a few. Also sulphides or elementary materials are processed as powders like for example lead sulphide (PbS), indium sulphide (InS), carbon black (C), etc. Many properties of powders do depend on the particle size and there is a growing interest to exploit these properties by tailoring the particle size of powders.

One of the most important powders is silica (SiO_2). In 1990 about 1 billion kg was produced in the western hemisphere. The gas phase flame hydrolysis is by far the most important method for the production of silica powder (Michael *et al.* [50]). The flame hydrolysis of silica is illustrated in figure 2.1.1. The gas phase synthesis processes of other oxides like aluminium oxide (Al_2O_3) or titanium dioxide (TiO_2) are similar.

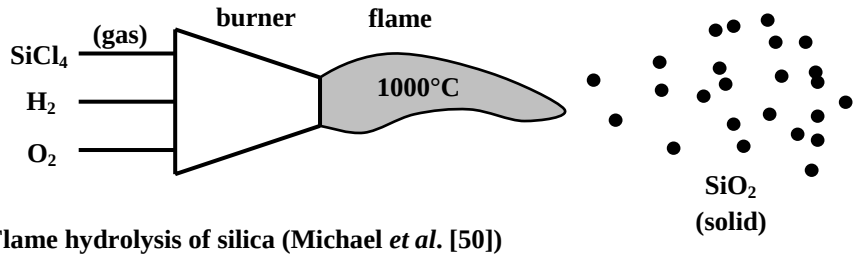

Figure 2.1.1: Flame hydrolysis of silica (Michael *et al.* [50])

SiO_2 synthesis is ruled by the following chemical reactions:

$$2H_2 + O_2 \rightarrow 2H_2O$$
$$SiCl_4 + 2H_2O \rightarrow SiO_2 + 4HCl$$

respectively TiO_2 by:

$$2H_2 + O_2 \rightarrow 2H_2O$$
$$TiCl_4 + 2H_2O \rightarrow TiO_2 + 4HCl$$

The water synthesis supplies the heat for the reaction. A side product of the silica hydrolysis as well as of the TiO_2 hydrolysis is hydrochloric acid (HCl). The latter of course is a great problem for any measurement

instrument, especially since also water (H_2O) is present and the combination of H_2O and HCl is extremely corrosive.

The particle formation process within the reactor is a very complicated process and ruled by the interaction of nucleation (formation of particles out of a supersaturated vapour), condensation and evaporation, coagulation (formation of particles by particle collisions), sintering, and transport mechanisms such as convection, diffusion (by Brownian motion), and thermophoresis (motion of particles caused by a temperature gradient). Process parameters which influence the particle size of powders formed by gas phase synthesis are the concentrations of the reactants, the flame temperature, the pressure, and the residence time of the silica in the reactor.

In order to tune the particle size by these parameters and to reveal the effects of different unit operations, for example coolers, acid absorbers, cyclones, filters, sampling, etc. on the particle size, representative sampling of the particles in the gas phase at different stages of the process and rapid measurement of number size distribution density are essential. Methods which are used up to now to measure the particle size in the industrial synthesis processes do neither provide number size distributions of aggregates and agglomerates nor allow representative sampling (chapter 2.4).

2.2 Primary particles, agglomerates, and aggregates

Before particle size and particle size distribution are discussed in chapter 2.3, it is necessary to define the term particle. Particles can differ in shape, structure, density, morphology, porosity, etc. Particles can coagulate and form bigger particles. In case that the particle material is in the liquid phase, two droplets can form one larger droplet. In case of solid material, agglomerates or aggregates are generated. For solid particles it has to be distinguished between primary particles and agglomerates or aggregates. For primary particles the generation and growth mechanisms are nucleation, condensation, sintering, and chemical reactions. Within an agglomerate or aggregate a primary particle is the smallest identifiable unit.

Agglomerates and aggregates are generated due to random collisions between particles and adhesive forces causes the particles to stick together. The adhesion comes by van der Waals forces (agglomerates) and by ionic or covalent bounds (aggregates). The difference between agglomerates and aggregates is that for agglomerates the primary particles are bonded together rather weakly, for aggregates rather strongly. The distinction however is not definite. Agglomerates can be cracked by strong mechanical forces or by agitation in a liquid (Michael *et al.* [50]). An important property of agglomerates is that their surface is not considerably smaller than the sum of the surfaces of the constituting primary particles (VDI [77]).

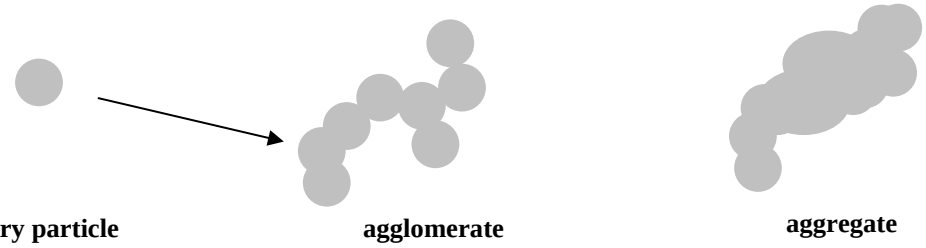

Figure 2.2.1: Primary particle, agglomerate, and aggregate

Depending on which growth mechanisms are predominant the particles appear as single particles, as agglomerates, or as aggregates. For the many applications it is the agglomerate and aggregate size which is a characteristic feature of a powder. Examples of properties which depend on the agglomerate or aggregate size are the rheology (Michael *et al*. [50]) or optical properties (Tishkovets *et al*. [74]).

In figure 2.2.1 the primary particle is assumed to have a spherical shape, which in general is not the case. Depending on the material and particle generation dynamics particles also can appear rectangularly, as fibre, tube, be regular or irregular. Consequently the agglomerates and aggregates also appear variously (VDI [77]).

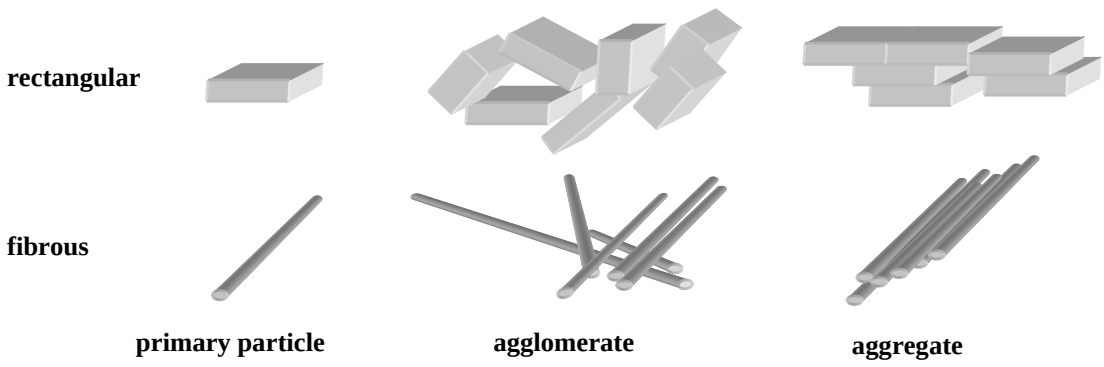

Figure 2.2.2: Non spherical primary particles, agglomerate, and aggregate (VDI [77])

For SiO_2 hydrolysis and furnace synthesis the primary particles are approximately spherical. The agglomerates and aggregates resemble those suggested by figure 2.2.1. In figure 2.2.3 a transmission scanning electron microscopy (TEM) image of SiO_2 particles is shown. The particles have been synthesized by a furnace reaction. For the TEM imaging a sample has to be taken from a filter, dispersed in a liquid and dried on a substrate. This preparation can change the agglomerates because of the rather weak bonds between the primary particles.

All the techniques so far used to determine the sizes of agglomerates fail for nanoparticles and when fast measurement is needed (see chapter 2.4). They also fail because sampling and sample preparation change the

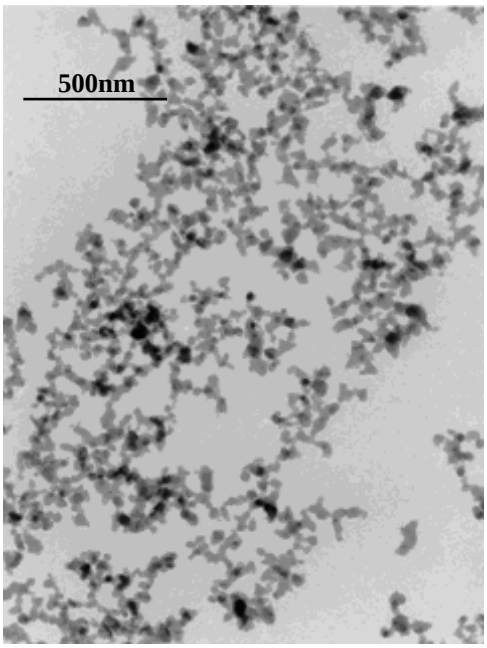

Figure 2.2.3: TEM image of SiO_2 particles (source: Degussa)

particles e.g. by the formation of large agglomerates on filters or substrates. In order to fill this gap a technique of sampling and size measuring is needed, which does not change the particles by coagulation or by forces which can break agglomerates. One method which does not change the sample particles is the differential mobility analysis (chapter 3) because the particles remain gas borne.

The differential mobility analysis does not determine primary particle sizes but the sizes of aggregates and agglomerates. Therefore it is a favourable measurement principle, since important physical properties (optical, electrical, rheologic, hydrophobic, etc.) depend on the sizes of aggregates and agglomerates.

2.3 Particle size and particle size distribution

2.3.1 Particle size

The term particle size implies that the size of a particle can simply be given by a number and a unit. That is unambiguous only in case all particles have the same shape, in the simplest case when all particles are spherical. As discussed in chapter 2.2 this is in general not given. In order to give the particle size by one quantity despite of different shapes, requires the introduction of an equivalent diameter (Hinds [24]). An equivalent diameter is the diameter of a sphere which has a certain size- depending property with the particle in common. This property depends on the principle used for the determination of the particle size and on whether this property well characterizes the particle with respect to a certain application.

In aerosol technology several equivalent diameters are used. This can be for example the diameter of a sphere of which the projected area equals the one of the respective particle (typical by TEM image analysis). The equivalent diameter is called *equivalent circle diameter* (ECD).

The *aerodynamic diameter* is the diameter of a sphere which has the same settling velocity as the particle and a density of 1g cm^{-3}. The *Stokes diameter* is the one of a sphere with the same settling velocity and the same density as the respective particle (Kodas *et al*. [37]). These two are used when the particle inertia plays an

important role or when gravitation is the dominant force. The aerodynamic diameter is used in case that the material and therefore its density is unknown.

With mobility analysis the particle size is represented by the size of a sphere with the same mobility as the particle. The equivalent diameter is called the *mobility diameter*. In the sub micrometer range gravitation and inertia are negligible. Therefore the velocity of a particle is independent of its mass.

Differential mobility analysis determines the electrical mobility of a particle. The electrical mobility is the relation between the magnitude of an electrical field E and the particle velocity v which is constant when the drag force F_D and the Coulomb force F_C are of the same magnitude (figure 2.3.1.1). Differential mobility analysis provides particles having a certain charge Q.

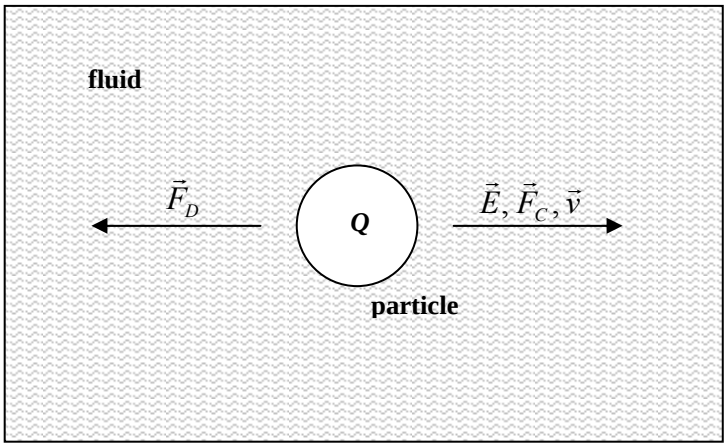

Figure 2.3.1.1: Balance of drag force F_D and Coulomb force F_C used by differential mobility analysis

From the mentioned equivalent diameters in the nanometer size range only the mobility diameter and the ECD characterize the particle size appropriately, because the particles have quasi no mass and no inertia. Since the ECD suffers from problems of sampling, long analysis times, and from high financial, working and laboratory expenses, it is but consequent to extend the applicability of differential mobility measurements to synthesis processes of powders.

2.3.2 Particle size distribution

Aerosol sizing instruments present a continuous size distribution by m discrete successive size intervals yielding m numbers N_k for $1 \le k \le m$ with the total concentration

$$N_{tot} = \sum_{k=0}^{m} N_k \ . \qquad (2.3.2.1)$$

For the most of natural and artificial generation processes, e.g. combustion and furnace processes, the size distribution is lognormal (Hinds [24], Friedlander [19], Kodas *et al*. [37]). The lognormal distribution size distribution for discrete size channels $D_{P,k}$ is defined by

$$\frac{dN}{dD_P} = \frac{N_{tot}}{\sqrt{2\pi} D_{P,k} \ln \sigma_g} \exp\left(- \frac{\left(\ln D_{P,k} - \ln D_g\right)^2}{2\left(\ln \sigma_g\right)^2} \right) \tag{2.3.2.2}$$

In many cases it is desirable to give the size distribution in terms of an average size and a spread. For aerosols with a lognormal distribution the geometric mean size D_g is widely used defined by

$$\ln D_g = \frac{\sum_{k=0}^{m} N_k \ln D_{P,k}}{N_{tot}} \tag{2.3.2.3}$$

with the geometric standard deviation σ_g, defined by

$$\ln \sigma_g = \sqrt{\frac{\sum N_k \left(\ln D_{P,k} - \ln D_g\right)^2}{N_{tot}}} \; . \tag{2.3.2.4}$$

Certain properties of aerosols are proportional to a power of the particle size as for example surface $\left(\propto {D_P}^2\right)$ area or mass concentration $\left(\propto {D_P}^3\right)$ (Kodas *et al*. [37]). The properties are obtained by integration of the size distribution, weighted by the appropriate power of the size over the entire size range, in general expressed by the *j*th moment

$$M_j = \sum_{k=0}^{m} N_k {D_{P,k}}^j \; . \tag{2.3.2.5}$$

The moments are useful in defining aerosol properties, production criteria and average particle sizes obtained from weighted distributions as for example the total number concentration M_0, the total particle surface πM_2, the total volume $\frac{\pi M_3}{6}$, the powder production rate $\frac{\pi \rho_P M_3 \dot{V}}{6}$, the specific surface area $\frac{6 M_2}{\rho_P M_3}$, the mass mean diameter $\frac{M_4}{M_3}$, or the surface mean diameter $\frac{M_3}{M_2}$ (Kodas *et al*. [37]).

2.4 Methods for the measurement of size distributions of submicron powders

The main methods which are used up to now for the size characterization of submicron particle sizes of powders are the TEM image analysis and the determination of the specific surface area (chapter 2.4.2). Further methods of particle size determination of industrial powders exist (Batel [3]). These methods base on

the sieve analysis and fail, when the particle sizes are in the nanometer size range. Size measurements on powders so far are done mainly on the final product, on material sampled by sieves and filters (Michael [50]) but not within synthesis processes.

2.4.1 Electron microscopy

The analysis of scanning or transmission electron microscopy (SEM, TEM) images is a common method to determine the sizes of primary particles and with restrictions the sizes of aggregates and agglomerates. The accuracy of number size distributions obtained by electron microscopy image analysis is rather poor. Electron microscopy is expensive and takes a long time. The major problem of electron microscopy is to get the particles onto a suitable substrate. The most common way is to disperse the product into a liquid and to pour it onto a TEM suitable substrate. This on the one hand is only possible for the end or near end product because it is difficult to sample out of the process, on the other can change the particles. Köylü *et al*. [39] proposed a pneumatic apparatus to shortly expose substrates to the aerosol inside particle generation processes. The mechanism by which the particles are driven onto the substrate is thermophoresis. A further sampling method is the usage of micropore polycarbonate filters (Nucleopore, Corning Costar Corp., MA, USA) in connection with a highly diluting sampling probe as introduced in chapter 4.2. The micropore filters are suitable for scanning electron microscopy imaging. The pore size is 400nm. The particles can be sampled out of the generation process directly.

Figures 2.4.1.1 to 2.4.1.3 show SiO_2 particles out of a furnace process (Degussa hot wall reactor) by three different sampling methods (identical process and product).They illustrate how much the appearance of the particles on the substrates depend on the way of sampling. All methods suffer from artefacts due to several particle- particle and particle- substrate interactions. These interactions can be of electrical, chemical, or physical nature.

Diffusion, impaction, and the charging of the particles by thermal emission are phenomena which distort a representative distribution of particles on the substrate surface. In figure 2.4.1.3 it is obvious, that particles on the filter are mainly deposited around the holes. This is caused by the gas flow field and enhanced by the charges on the particles since an oppositely charged particle rather will meet another charged particle, one with the same charge rather will go through the hole. As a consequence there is a certain probability of the generation of agglomerates on the surface of the substrate and subsequently a shift of the number size distribution towards a bigger particle size. This could be shown by measurements at powder synthesis processes presented in chapter 5. Also the electron microscopy itself affects the analysis result. It requires high vacuum causing liquid material to evaporate. Sample preparation (for example gold vapour deposition) and adjustments as to brightness, contrast, etc. depend on the experience of the operator of the instrument and influences the result.

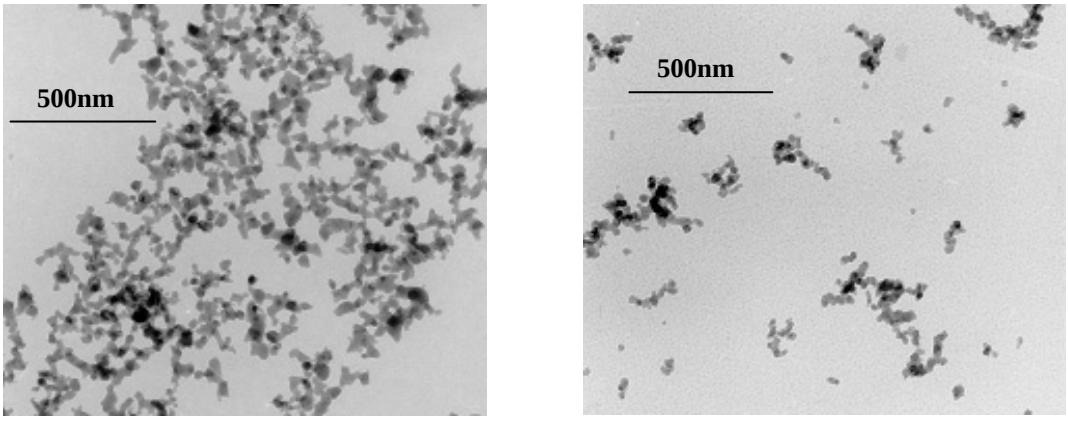

Figure 2.4.1.1a, b: SiO_2 particles from isopropanol dispersion (TEM: Degussa AG)

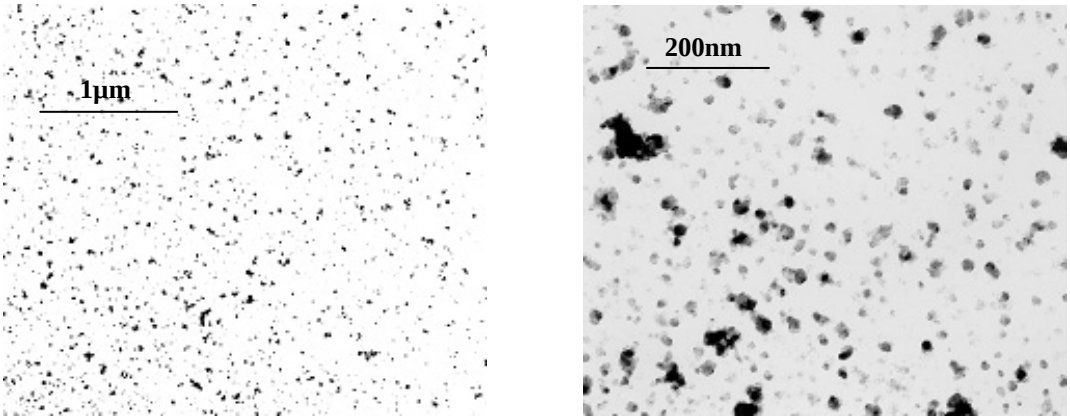

Figure 2.4.1.2a, b: SiO_2 particles by direct sampling on a substrate (TEM: Degussa AG)

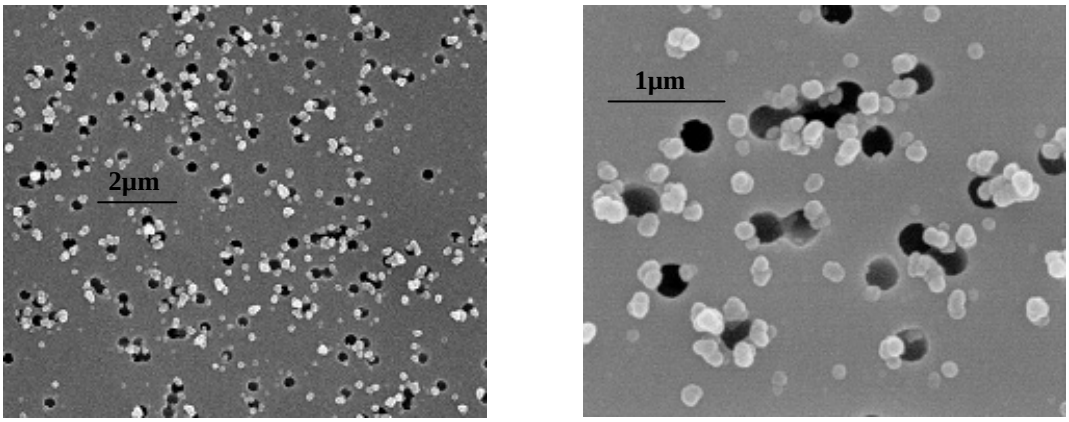

Figure 2.4.1.3a, b: SiO_2 particles sampled by a micropore filter (SEM: Degussa AG)

The analysis on the digitalized image can be performed by special software. It helps to decide whether a spot on the substrate has to be considered as particle or not by adjustable criteria (e.g. thresholds of contrast and brightness). Particle sizes can be estimated from the projected areas.

Electron microscopy is reliable for size primary particles. However it is not suitable to survey powder synthesis processes because it is too slow. Furthermore it is very expensive and suffers from the lack of appropriate sampling. A representative high dilution sampling is necessary which avoids coagulation on the grid. For aggregates and agglomerates sizing is uncertain because it is difficult to separate them from primary particles when they once are deposited on a grid or micropore filter.

2.4.2 The specific surface area

Up to now the most important method used method to characterize powders as to their size is the measurement of the specific surface area (surface related to mass). The specific surface A_{SS} area depends on the 2nd and 3rd moments of the size distribution by $A_{SS} = \frac{6M_2}{\rho_P M_3}$.

The specific surface area is measured by determing the amount of gas (e.g. nitrogen) which is adsorbed by the powder at low temperatures (Brunauer *et al*. [7]). The surface area depends on the porosity of the particle material. Thus for size measurements a calibration by electron microscopy is necessary. The specific surface area is a powder property that can be used for the estimation of primary particle sizes since the cross section areas of the interconnections between the primary particles are comparatively small. It delivers no size distribution but an average only.

2.4.3 Optical methods for the determination of submicron particle sizes

Optical methods play an increasingly important role because of the progress in laser technology, optical sensoring and digital data processing. To optical methods belong light scattering (Mölter *et al*. [53, 54]), photon correlation spectroscopy (Pecora [59]), laser induced incandescence (Filipov *et al*. [13]), or x-ray diffraction (Als-Niesen *et al*. [1]), Brumberger [6]). Instruments exploiting one of these phenomena are commercially available.

Light scattering instruments can deliver size distributions of submicron aerosols in situ. The decisive disadvantage is the restriction of the size range to small particle sizes. The contemporary type WELAS 1100 by PALAS for example has a size range from 180nm to 40µm.

Photon correlation spectroscopy (PCS) determines particle sizes by detecting fluctuations of light frequency due to Brownian motion. PCS is applied to the measurement of an average particle size and a measure of the broadness of the size distribution of particles dispersed in liquids. It is applicable to particle sizes ranging from a few nanometers to about 1 micrometer (ISO [31]).

The laser induced incandescence (LII) is a promising technique and has been applied by Bockhorn *et al*. [5] for size measurements in powder synthesis processes. LII measures the energy emission of particles after a laser pulse. It can yield number size distributions of primary particles but is not able to determine the sizes of agglomerates.

X-ray diffraction (XRD) like laser techniques benefits from progress in optoelectronics and is an important tool in characterising solid state materials for semiconductor processing. Powder XRD can provide information about crystalline structure in a sample even when the crystallite size is too small for single crystal x-ray diffraction. XRD is expensive as to costs and sample preparation and much too slow to monitor particle sizes in processes.

Small Angle X-Ray Scattering (SAXS) is used for probing large length scale structures such as high molecular weight polymers, biological macromolecules (proteins, nucleic acids, etc.), and self-assembled superstructures. It can be used to determine the size, the shape, the distribution, orientation, and correlation of nanoparticles present in solids or solutions (Hyeon-Lee *et al*. [28]).

2.4.4 Particle sizing due to diffusion, inertia, or mobility

(Small) particles can be separated according to their diffusivity. Diffusion batteries are devices of a serial or parallel arrangement of different pipes or ducts able to yield diffusivity information between 2 and 200 nm. The information is not very size selective and difficult to transform into size distributions (Hinds [24]). Fierz *et al*. [12] presented an electrically enhanced diffusion battery with a time resolution of a few seconds but however poor size resolution.

Particle inertia is used for size fractionation by cyclones and impactors. These instruments expose the particles to a centrifugal force by a curvilinear motion of the gas. Sequential impactors with contiguous cut off sizes can yield cumulative size distributions by the aerodynamic diameter. Impactors commonly are used for long term average size distribution measurements for large particle sizes. They offer only poor size resolution. Improvements have been proposed by Keskinen *et al*. [35]. They developed an electrical low pressure impactor (ELPI) consisting of 13 contiguous stages feeding 12 electrometer. The instrument is fast and suitable for low pressure applications but suffers from poor size resolution (factor 10 compared to SMPS, see below).

Particle inertia is also used by the particle mass spectrometer (PMS) (Roth *et al*. [62]). The principle of the PMS is the electrostatic lateral deflection of a particle beam in vacuum similar to the deflection of electrons in a cathode ray tube. Like the differential mobility analysis it requires particles to carry a known charge. Depending on the geometry, particle sizing down to molecular size is possible. Roth *et al*. [62] determined the diameter of silver particles from a few nanometers up to 60nm. The PMS is suitable for low pressure applications, as the aerosol has to be transferred into vacuum in form of a beam.

The relationship between a force on a particle and the particle velocity in a fluid is called mechanical mobility. The velocity depends on particle size. The force can be gravitation, then particles can be separated according to their settling velocity. The same principle is exploited by the differential mobility analysis (Knutson *et al.* [36], Liu *et al*. [44]). Here the driving force is the Coulomb force on charged particles by an electrical field. With differential mobility analysis particles are separated by their velocity. Only those of a certain velocity are withdrawn out of the ensemble. In theory the deviation around a mean velocity can be infinitively small.

Differential mobility is the most common principle to measure submicron aerosol size distributions between 1nm and 1µm. The great advantages of the differential mobility analysis are that the particles remain gas borne without any effect from sample preparation and that it offers high size resolution. Automatic aerosol sizing instrumentation has been developed using the differential mobility analysis like the differential mobility particle size DMPS (Keady *et al*. [34], Fissan *et al*. [15]) and derivates like the electrical aerosol sizer EAS (Tammet *et al.* [71]) and the scanning mobility particle sizer SMPS (Wang *et al*. [79]).

A lot of work has been done to overcome problems in the nanometer size range (Rosell-Llompart *et al*. [61], Hummes *et al*. [26]). Innovations have been presented to modify DMPS instrumentation with respect to particle size range (Müschenborn *et al*. [56]) and pressure (Seto *et al*. [65]). Still there is no DMPS instrumentation able to deliver size distributions of agglomerates and aggregates for various low pressures under high concentrations and presence of hydrochloride and water as prevailing in powder synthesis processes.

2.5 Requirements of a size distribution measurement system at industrial powder synthesis processes

In 1997 the Deutsche Forschungsgemeinschaft DFG established a Schwerpunktprogramm SPP1062 ”handling of highly dispersed powders” to close the gap between the demands of modern material sciences for powders of nanoscaled particles and the classical possibilities of mechanical process engineering. A broad community out of material sciences, process engineering, physical chemistry, or theoretical physics was addressed (Müller *et al*. [55]). Cooperation between DFG and the Degussa AG followed leading to the “Projekthaus Nanomaterialien”. The idea was to illuminate aspects of the processing of nanoscaled powders.

A basic demand in order to judge on the success of new ways in powder processing has been a technology which is able to deliver highly resolved size distributions at any point in the chain of unit operations.

The requirements for a measurement system for size distribution measurements at industrial powder synthesis processes have been derived by theoretical considerations of the conditions prevailing in the plants of Degussa. The system has to cope with:

1. Number concentrations in the range between $10^8 cm^{-3}$ and $10^{14} cm^{-3}$.

2. Particle (aggregate) size range from 10nm to 500nm.

3. Temperatures between 1000°C and 2000°C.

4. Highly corrosive gases. A side product of the hydrolysis of chlorides such as $TiCl_4$ or $SiCl_4$ is hydrochloric acid. Since water is present, this mixture is highly corrosive.

5. Sub-atmospheric pressures, e.g.in the hydrolysis of TiO_2 as low as 50mbar.

6. The application of a radioactive source for the particle charging is impossible due to corrosion of the material containing the radioactive source and the risk of contamination of a whole industrial plant.

7. Fluctuations of pressure and concentrations.

From the methods for the measurement of size distributions of submicron powders given in chapter 2.4 only the differential mobility analysis (Knutson *et al.* [36]) and the particle mass spectrometry (Roth *et al*. [62]) in connection with high dilution sampling are capable to fulfil the requirements given above. PMS is an elegant and sophisticated method to determine size distributions. Differential mobility analysis is comparatively simple and a lot of experience of application already exists. Therefore the differential mobility analysis is favoured for a new size distribution measurement system at industrial powder synthesis processes.

3 Measurement of number size distributions by the differential mobility analysis

3.1 Differential mobility analysis

3.1.1 Principle

A particle property which is size dependent and can be used to judge on the particle size D_P is the mechanical particle mobility B. The mechanical mobility is a measure for the resistance against a movement in a fluid. In case of constant velocity v the drag force F_D is given by Stokes' law:

$$F_D = 3\pi \cdot \eta \cdot D_P \cdot v \tag{3.1.1.1}$$

where η is the dynamic viscosity of the fluid. Equation 3.1.1.1 is valid provided that:

1. The particles are spherical.
2. $D_P >> \lambda$,with λ the mean free path of the molecules of the fluid.

Millikan [51] showed that small oil droplets in air move faster than predicted by Stokes' law. This can be explained by the fact that for small particles the relative movement is ruled by collisions between the droplets (particles) and the molecules of the fluid. Particle movement is characterized by the dimensionless Knudsen number $Kn = \frac{\lambda}{R_P} = \frac{2\lambda}{D_P}$. For $Kn < 0.01$ the flow can be assumed to be continuous and the drag force follows equation 3.1.1.1. For $Kn > 10$ the flow is called free molecular and the drag force is smaller than given by Stokes' law. The range of validity of equation 3.1.1.1 has been extended by the Cunningham "slip" correction factor **(**Hinds [24])

$$C_C(D_P, p) = 1 + \frac{\lambda(p)}{D_P} \cdot \left(2.514 + 0.8 \cdot \exp\left(-0.55 \cdot \frac{D_P}{\lambda(p)} \right) \right). \tag{3.1.1.2}$$

Kn depends on the gas. C_C depends by means of the mean free path $\lambda(p)$ on the pressure p. The expression for the drag force corrected by particle slip becomes

$$F_D = \frac{3\pi \cdot \eta \cdot D_P \cdot v}{C_C(D_P, p)}. \tag{3.1.1.3}$$

The pressure dependency of C_C will be discussed in chapter 3.4.

The mechanical mobility B is the ratio of the particle velocity and the sum of all acting forces. In the case of a linear motion

$$B = \frac{v}{\sum_i F_i} . \tag{3.1.1.4}$$

When the velocity is constant there is a balance of the forces $\sum_i F_i = F_D$ and B can be expressed by

$$B = \frac{C_C(D_P, p)}{3\pi \cdot \eta \cdot D_P} . \tag{3.1.1.5}$$

In case that the Coulomb force $F_c = Q \cdot E$ (Q: electrical charge, E: electrical field strength) is the only contribution to F_i, the electrical mobility Z_P is defined by

$$Z_P = \frac{v}{E} = \frac{Q \cdot C_C(D_P, p)}{3\pi \cdot \eta \cdot D_P} \tag{3.1.1.6}$$

which relates the particle velocity v to the electrical field strength E.

In the sub micrometer particle size range particle inertia and gravitation play no role and the Coulomb force is the only one to be considered. The time $t = \frac{b}{v}$ which is necessary for a charged particle to travel a certain distance b in a homogeneous electrical field is

$$t = \frac{b}{Z_P \cdot E} = \frac{3\pi \cdot b \cdot \eta \cdot D_P}{Q \cdot C_C(D_P, p) \cdot E} . \tag{3.1.1.7}$$

A DMA exposes particles to an electrical field E. It lets only those particles pass which travel a certain distance b within a certain time t. The exposition time t is determined by a clean gas flow perpendicular to the electrical field. Figure 3.1.1.1 illustrates the principle of a DMA with a rectangular duct.

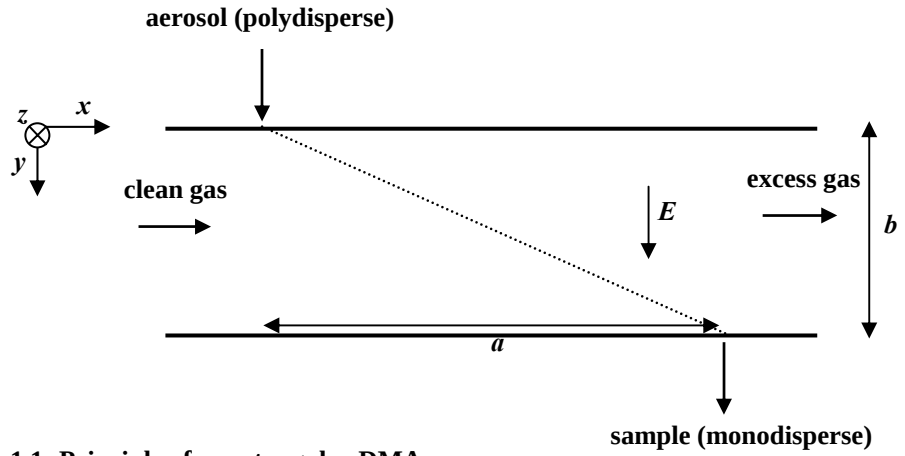

Figure 3.1.1.1: Principle of a rectangular DMA

All particles travel the distance a in the time $t_x = \frac{a \cdot b \cdot c}{\dot{V}_a + \dot{V}_c}$, where $\dot{V}_a$ and $\dot{V}_c$ denote the aerosol- and clean gas volume flows. c is the extension of the duct in z-direction. Only those particles reach the outlet for which

$$t_x = t_y = \frac{b}{Z_P \cdot E} = \frac{a \cdot b \cdot c}{\dot{V}_a + \dot{V}_c} \tag{3.1.1.8}$$

where t_x and t_y are the times in x- and y- directions leading to

$$Z_P = \frac{\dot{V}_a + \dot{V}_c}{a \cdot c \cdot E} . \tag{3.1.1.9}$$

With $U = E \cdot b$ the voltage between the top and the bottom electrode:

$$Z_P = \frac{\left(\dot{V}_a + \dot{V}_c\right) \cdot b}{a \cdot c \cdot U} \tag{3.1.1.10}$$

and

$$D_P = \frac{a \cdot c \cdot Q \cdot C_C(D_P, p) \cdot U}{3\pi \cdot \left(\dot{V}_a + \dot{V}_c\right) \cdot b \cdot \eta} \quad . \tag{3.1.1.11}$$

D_P depends on the voltage U and on the charge Q only, since the remaining quantities usually are kept constant.

Equation 3.1.1.11 must be solved iteratively because the slip correction C_C is a function of D_P.

In general the DMA is used to separate particles of a given size from a polydisperse aerosol. In that case the voltage between the electrodes of the (rectangular) DMA has to be

$$U = \frac{3\pi \cdot D_P \cdot \left(\dot{V}_a + \dot{V}_c\right) \cdot b \cdot \eta}{a \cdot c \cdot Q \cdot C_C(D_P, p)} . \tag{3.1.1.12}$$

3.1.2 Designs of differential mobility analyzers (DMA)

For practical applications a rectangular DMA design as sketched in figure 3.1.1.1 is not suitable because edge effects would cause inhomogeneities of the gas flow or the electrical field. The most common type used in particle sizing instruments is the cylindrical DMA (CDMA) sketched in figure 3.1.2.1. It consists of two coaxial cylindrical electrodes between which the clean gas flows and a homogeneous electrical field is applied. The aerosol is tangentially introduced via a circular gap at the outer electrode. Particles with a charge of the appropriate sign travel toward the inner electrode and, assumed they have the mobility determined by the volume flow and the voltage, enter a gap in the inner electrode and leave the instrument via the sample outlet. The midpoint mobility of the particles which pass the gap in the inner electrode is given by (Knutson *et al*. [36]):

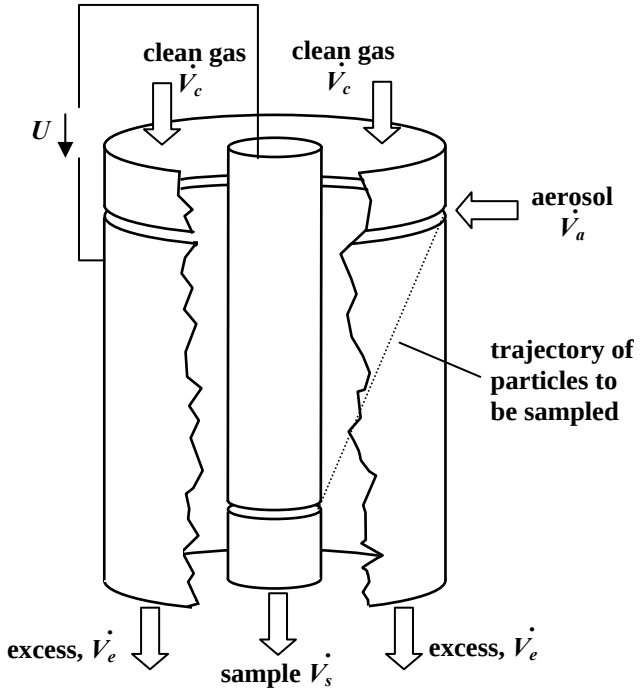

Figure 3.1.2.1: Cylindrical DMA, principle

$$Z_P^* = \frac{\dot{V}_c + \dot{V}_e}{4\pi \cdot l \cdot U} \ln\left(\frac{R_2}{R_1}\right) \qquad (3.1.2.1)$$

where R_1 and R_2 are the radii of the inner and outer electrode, l the axial distance between in- and outlet gap, $\dot{V}_e$ the excess gas volume flow, and U the electrical voltage between the electrodes.

The second DMA type is the radial DMA (RDMA) as shown in figure 3.1.2.2. It consists of a parallel arrangement of two circular, even electrodes. In contrast to the CDMA, the electrical field is homogeneous but the gas velocity depends on the radial position. For the RDMA the midpoint mobility Z_P^* is determined by (Zhang *et al*. [86])

$$Z_P^* = \frac{\left(2\dot{V}_c + \dot{V}_a - \dot{V}_s\right) \cdot b}{2 \cdot \pi \cdot \left(R_2^{\,2} - R_1^{\,2}\right) \cdot U} \qquad (3.1.2.2)$$

respectively

$$Z_P^* = \frac{\dot{V}_c \cdot b}{\pi \cdot \left(R_2^{\,2} - R_1^{\,2}\right) \cdot U} \qquad (3.1.2.3)$$

for $\dot{V}_a = \dot{V}_s$.

R_1 and R_2 denote the radii of the out- and inlet. b is the axial distance between the electrodes.

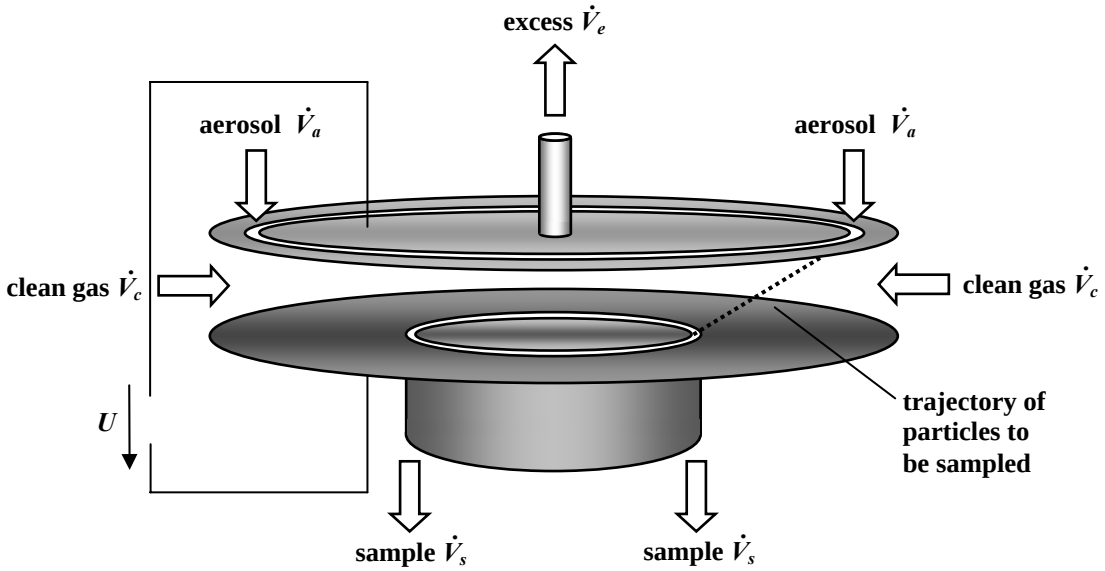

Figure 3.1.2.2: Radial DMA, principle

The midpoint mobility Z_P^* can be compared to the centre frequency of an electrical filter since a DMA lets a certain mobility *spectrum* pass. The specific filter characteristic of a DMA is determined by the DMA transfer function (chapter 3.1.3).

Although in the literature and for practical applications mostly the cylindrical type is used the two types of DMA operate analogously. For the CDMA the gas flow field in axial direction is constant and the electrical field has a $\frac{1}{r}$ dependency. For the RDMA it is vice versa.

3.1.3 The DMA transfer function

Knutson *et al*. [36] introduced the transfer function $\Omega(Z_P)$ as the probability that a particle of a certain mobility Z_P which enters the DMA, leaves the device via the sampling flow $\dot{V}_s$. They showed that in case no diffusion is effective and no particles are deposited on the walls of the DMA (cylindrical or radial), the transfer function is a trapezoid given by

$$\Omega(Z_P) = \frac{1}{\dot{V}_a} \cdot \max\left(0, \min\left(\dot{V}_a, \dot{V}_s, \left(\frac{1}{2} \cdot \left(\dot{V}_a + \dot{V}_s\right) - \left|2\pi \cdot Z_P \cdot \Delta\phi + \frac{1}{2}\left(\dot{V}_e + \dot{V}_c\right)\right|\right)\right)\right) \qquad (3.1.3.1)$$

with $\Delta\phi = \int_{inlet}^{outlet} \vec{E} d\vec{s}$ the potential difference between the in- and the outlet of the DMA. $\Delta\phi = \frac{l}{\ln\left(\frac{R_2}{R_1}\right)} \cdot U$ for the CDMA and $\Delta\phi = \frac{{R_2}^2 - {R_1}^2}{2b} \cdot U$ for the RDMA. Figure 3.1.3.1 shows the transfer function for both types for the case of no diffusion.

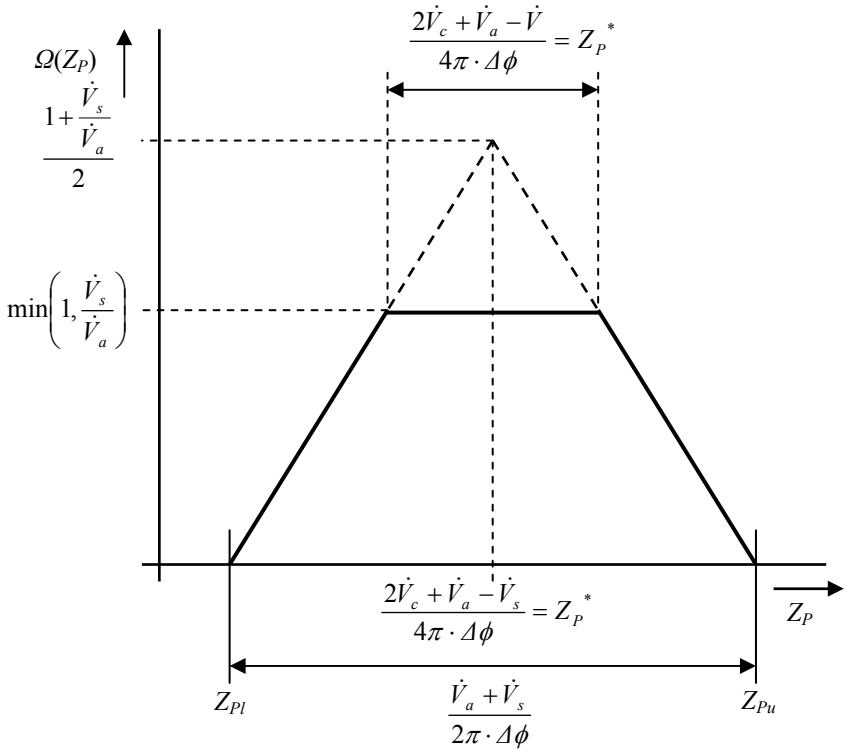

Figure 3.1.3.1: Transfer function for CDMA and RDMA

Z_{Pl} is the lower, Z_{Pu} the upper limit of the mobility range. Usually a DMA is operated with matched flows $\dot{V}_a = \dot{V}_s$ and $\dot{V}_c = \dot{V}_e$ because the gas flows are easy to control. Clean and excess gas flows $\dot{V}_c$ and $\dot{V}_e$ then can be provided by a closed loop arrangement using a particle filter. The half width $\beta_{Z_P} = \frac{\dot{V}_a + \dot{V}_s}{\dot{V}_c + \dot{V}_e}$ with $Z_{Pl} = {Z_P}^*(1 - \beta_{Z_P})$ and $Z_{Pu} = {Z_P}^*(1 + \beta_{Z_P})$. In case of matched flows the trapezoid is a triangle with $\beta_{Z_P} = \frac{\dot{V}_a}{\dot{V}_c}$.

Two phenomena influence the shape of the transfer function:

1. The diffusion of particles caused by Brownian motion.

2. The loss of particles inside the DMA due to diffusion, distortions of the electrical field or the gas flow field at inlet and outlet.

The loss of particles inside the DMA leads to $\Omega < 1$ at the midpoint mobility Z_P^* and to a reduced height of the transfer function. Assuming a triangular shape the transfer function can be described by its half width β_{Z_P} and the height α_{Z_P} of the triangle.

Diffusion on the one hand enhances particle losses, on the other reduces the DMA resolution because particles are spread around the particle trajectories determined by the fluid flow and the electrical field lines. Subsequently β_{Z_P} increases and α_{Z_P} decreases. Since the effect of diffusion increases with decreasing particle size, deviations from the ideal, flow-determined transfer function are the greater the smaller the particles are (figure 3.1.3.2). Particle losses occur especially at the DMA in- and outlet because of distortions of the electrical field and the gas flow field. Another reason for particle losses can be the presence of isolating parts inside the DMA, because they can acquire charges and distort the electrical field. A measure for particle losses inside the DMA is the transmission efficiency η_{DMA}, which is defined as $\eta_{DMA} = \frac{\alpha_{Z_P,real}\beta_{Z_P,real}}{\alpha_{Z_P,ideal}\beta_{Z_P,ideal}}$, where $\alpha_{Z_P,real}$ and $\beta_{Z_P,real}$ have to be measured for each individual DMA, $\alpha_{Z_P,ideal} = 1$ and $\beta_{Z_P,ideal} = \frac{\dot{V}_a}{\dot{V}_c}$ for matched flows.

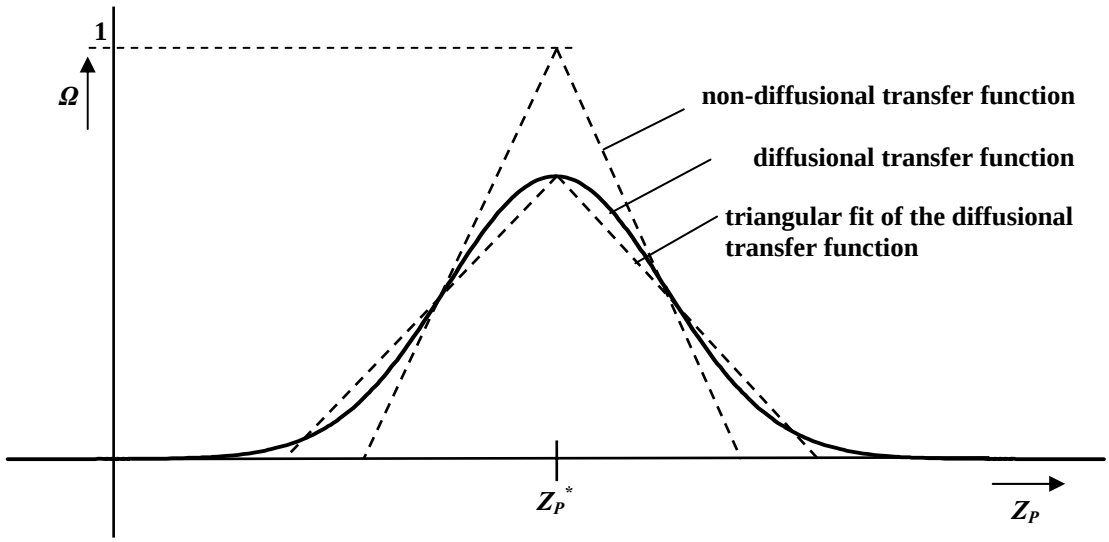

Figure 3.1.3.2: Non-diffusional and diffusional transfer functions of DMA

Stolzenburg [67] introduced a semi analytical approach to describe the diffusional effect on the shape of the transfer function and on the resolution of the DMA. He developed a description of the Gaussian shape of diffusional transfer function by means of stochastics. His approach describes the influence of diffusion on the width of the transfer function of a DMA, but is not able to take diffusionally enhanced losses into account. Stratmann *et al*. [68] introduced a method to evaluate individual DMA transfer functions experimentally. They applied an arrangement of two DMA, of which one transfer functions is unknown. As a result the diffusion- affected transfer function is represented by a triangular coextensive fit (figure 3.1.3.2) and the transfer function is given by the half width β_{Zp} and the height α_{Zp} of the fitting coextensive triangle. The method has been adopted for the determination of the transfer function of the new low pressure DMA. Figure 3.1.3.3 illustrates the experimental setup for the determination of the DMA transfer function using the method introduced by Stratmann *et al*. [68].

A DMA_1 is fed with a polydisperse aerosol with a broad distribution. The centre mobility of DMA_1 is kept constant by a constant voltage. Alternatively the concentration downstream DMA_1 can be measured to determine the transmission efficiency η_{DMA} of DMA_2. The centre mobility Z_{P2} of DMA_2 is varied by varying the applied voltage. The particle concentration behind DMA_2 is measured in dependency on Z_{P2}. The procedure corresponds to a convolution of the number distribution density dN_{DMA1}/dZ_P with the transfer function $\Omega(Z_P)_{DMA2}$.

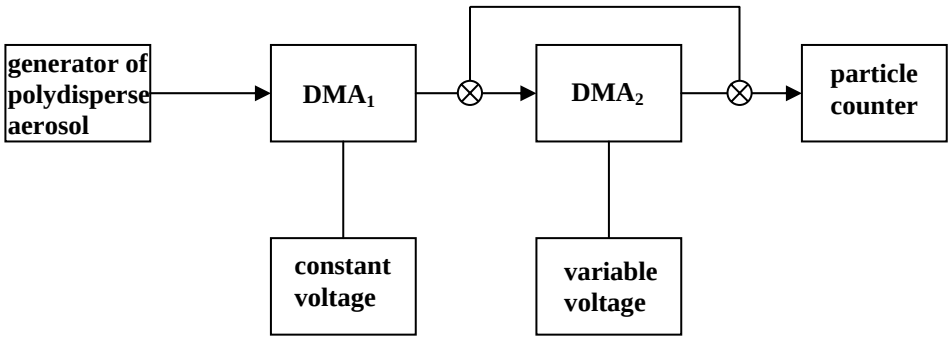

Figure 3.1.3.3: Setup for the experimental determination of DMA transfer functions

Provided that either one transfer function is known or the two DMA are of an identical type the unknown transfer function could in principle be calculated by a simple division in the Fourier regime. This operation leads to errors because the measurement results of the convolution $(dN_{DMA1}/dZ_P)*\Omega(Z_P)_{DMA2}$ in general are too noisy. Stratmann *et al*. [68] therefore proposed a numerical method which iteratively varies the transfer function until the result of the numerical convolution agrees with the result of the measurement.

For the application of a DMA as particle sizing device it is necessary to know its size resolution. Since Z_P as well as C_C depends on the particle size, the size interval around a centre mobility Z_P^* is considerably smaller

than the corresponding particle mobility interval. The particle sizes D_{Pl} and D_{Pu} corresponding to Z_{Pl} and Z_{Pu} can be calculated by:

$$D_{Pl} = \frac{Q \cdot C_C(D_{Pl})}{3\pi \cdot \eta \cdot Z_P^* (1+\beta_{Zp})} \tag{3.1.3.2}$$

respectively

$$D_{Pu} = \frac{Q \cdot C_C(D_{Pu})}{3\pi \cdot \eta \cdot Z_P^* (1-\beta_{Zp})} \tag{3.1.3.3}$$

In analogy to $\Omega(Z_P)$ a function $\Omega(D_P)$ can be defined as the probability for a particle to pass the DMA depending on the particle *size*. The function $\Omega(D_P)$ is also triangular. In case of no diffusion and matched flows this triangle can be described by a half width β_{D_P} and the height α_{D_P}. For a flow ratio $\frac{\dot{V}_s}{\dot{V}_c} = \frac{1}{10}$ and no diffusion $\beta_{Z_P} = \beta_{Z_P,\text{ideal}} = 0.1 = \text{const}$ whereas $\beta_{D_P,\text{ideal}}$ asymptotically approaches 0.05 for small particles (D_P < 10nm) and 0.1 for big particles (D_P >10µm) since β_{D_P} depends on the slip correction $C_C(D_P)$. α_{D_P} equals α_{Z_P}. Figures 3.1.3.4 shows $\beta_{D_P,\text{ideal}}$ as a function of the particle size D_P for the sub micrometer size range for matched flows and $\beta_{Z_P} = \beta_{Z_P,\text{ideal}} = 0.1$.

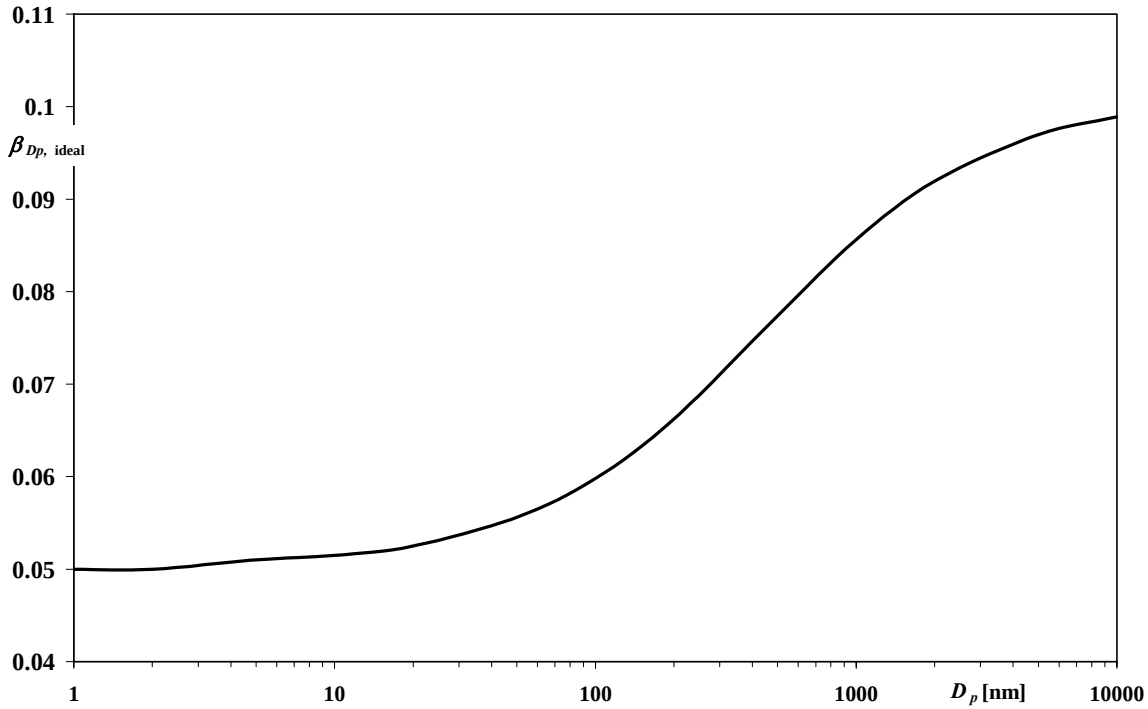

Figure 3.1.3.4: Half width $\beta_{Dp,\text{ ideal}}$ of the transfer function as a function of the particle size D_P for $\beta_{Zp,\text{ideal}}$ = 0.1

Figure 3.1.3.5 compares β_{Z_P} and β_{D_P} for the TSI Nano DMA (type 3085) for the non-diffusional case (ideal) as well as for the diffusional case (real). The Nano DMA has been used for the experimental determination of the transfer function of the new low pressure DMA.

The values for $\beta_{Z_P,\text{real}}$ for the TSI Nano DMA have been experimentally determined by Hummes *et al*. [27]. In figure 3.1.3.5 it can be seen that for increasing particle sizes the curves for β_{Z_P} and β_{D_P} (ideal and real) coincide. The diagram reveals that the two effects molecular slip and diffusion compensate each other more or less because the slip leads to a narrower, the diffusion to a wider size interval around D_P*.

With respect to the DMA size resolution $\frac{1}{\beta_{D_P,real}}$ however there is a maximum (minimum of $\beta_{D_P,real}$). The position on the size axis is characteristic for each DMA design.

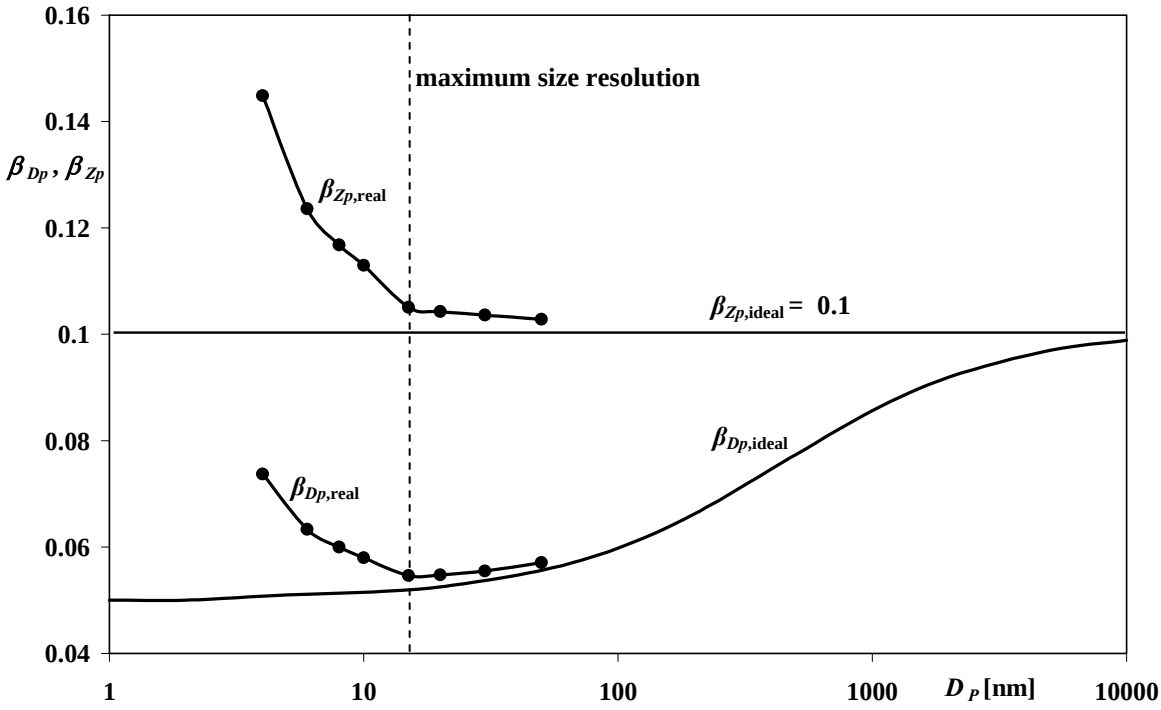

Figure 3.1.3.5: β_{Dp} and β_{Zp} as a function of the particle size D_P for the DMA type TSI 3085 for $\beta_{Zp,\text{ideal}}$ = 0.1. The values for $\beta_{Zp,\text{real}}$ are from Hummes *et al.* [27]. The values for β_{Dp} have been calculated using equation 3.1.3.2 and 3.1.3.3

A restriction as to the particle size range is given by the geometric dimensions of the DMA. The particle size range a DMA can handle, is limited by the diffusivity of small particles, by the maximum (laminar) volume flow and by the maximum voltage. A high volume flow reduces the effect of diffusion by reducing the residence time. On the other hand it shifts the size scope towards smaller particle sizes. A decisive property

as to the particle size scope of a DMA is the distance between in- and outlet gap. It is the very property, for which commercially available DMA for different size ranges differ. The two most frequently used DMA are the types 3081 and 3085 by TSI Inc. Both are cylindrical DMA, but differ in length. The 3081 has an axial distance between in- and outlet of 444.4mm and is designed to cover the size range from 10nm to 1000nm. The 3085 offers classification between 2nm and 150nm with comparable performance concerning efficiency and resolution. DMA for ultra fine particles (<10nm) furthermore need a very careful design of the inlet because small distortions of the laminar gas flow can gravely increase particle losses (Chen *et al*. [9]).

The choice of the volume flows and the flow ratio is a compromize between a high resolution (small β_{Zp} and β_{Dp}) and a sufficient high sample volume flow downstream of the DMA. For practical applications the volume flows depend also on pumps and instrumentation. If as particle detector a condensation nucleus counter is used, the sample flow can be either 0.3l/min or 1.5l/min (TSI model 3025A). For most cases (atmospheric aerosols, industrial powders) a flow ratio $\frac{\dot{V}_s}{\dot{V}_c} = \frac{1}{10}$ yields sufficiently resolved number size distributions leading to clean gas volume flows of either 3l/min or 15l/min.

3.2 Particle charging

3.2.1 Charging principles

The differential mobility analysis requires that particles are charged and a technique is necessary to imprint a known charge on a particle of a certain size. Gas borne particles can be charged either by collisions with ionized gas molecules or by the ionization of particles. Ionization of gas can be achieved by α-, β-, or γ-irradiation (Liu *et al*. [45], Kulkarni *et al.* [40]) or by corona discharge (Hinds [24]). A simple way to ionize gas is the exposure to the irradiation from a radioactive isotope like Kr^{85} or Am^{241}. The ionization generates positive and negative ions to approximately equal amounts and leads to a stable bipolar charging with a mean charge of zero (charge equilibrium) (Fuchs [20]).

Immediate ionization of particles can be achieved by ultra violet irradiation or by high temperatures (McClelland [49], Maisels *et al.* [46, 47]). The irradiation by ultra violet light (photo charging) is an effective method to charge particles. It avoids the risk of contamination with radioactive material but in general does not generate a steady state bipolar charge distribution (Burtscher *et al*. [8]). Photo charging depends on the number concentration of particles, on the material, the pressure, etc. (Maisels *et al.* [47], Seto *et al.* [65]). It is a dynamic process which is ruled by interactions between gas- and particle ions. The complex interaction between gas ions and particles and the influences of several physical properties on particle ionization make this mechanism difficult to model. Ionization of the gas also can be achieved by corona discharge which leads to unipolar charging. Unipolar charging can be very effective but does not lead to stable charge-distributions (Hinds [24]). Corona discharge is difficult to control and to model.

In the atmosphere particles acquire charge equilibrium because of the presence of ions due to cosmic irradiation. This process typically takes about 100 minutes. The use of α, β, or γ sources accelerates the charging of an aerosol. A 2mCi Kr-85 source charges aerosols within about one second and leads to a stable charge equilibrium. Therefore the process is also called neutralization.

In natural environment many investigations as to the bipolar charge equilibrium have been carried out. Nolan [57] hypothesized, that the charge distribution must be Boltzmann-distributed analogue to the energy distribution of the ions undergoing Brownian motion. Gunn [22] and Fuchs [20] modelled the particle charging taking into account the different mobility and concentrations of positive and negative gas ions (Gunn [22]) respectively different diffusion coefficients, mean free paths, velocities, and ion masses (Fuchs [20]). Wiedensohler [81] has modified the Fuchs theory for the bipolar diffusion charging of nanoparticles by varying the ion parameters in the Fuchs theory in order to fit his experimentally found data.

The knowledge of the probability or fraction $f(D_P,q)$ of a particle with the size D_P to have q elementary charges is essential for the calculation of number size distributions from DMPS raw data. In chapter 4.4 a model will be presented which is determines $f(D_P,q,t)$ numerically by solving population balance equations.

3.2.2 Photonic charging of particles

The photonic charging of particles is illustrated in figure 3.2.2.1. Photonic charging of particles is guided by two mechanisms: Ionization of particles (1) and recombination of gas (nitrogen) ions with particles enhanced by diffusion (3). The ionization of nitrogen is caused by free electrons from the particle surface (2). A certain amount of nitrogen ions go to the walls of the irradiated volume (4). Multiple charged particles occur due to a multiple excitation by several photons (positive) or an attachment of several nitrogen ions (negative). All nitrogen ions are assumed to be singly negative (Maisels *et al.* [47]). Positive nitrogen ions do not occur because of the high work function of the nitrogen. Saturation is acquired when a balance between ionization rate and the recombination rate is reached. If the irradiation is turned off, diffusion is the only (dis-)charging mechanism leading to an attachment of gas ions to particles (recombination). Steady state is acquired when the irradiation has been turned off and all gas ions have recombined with particles or are gone to the walls. Since only particle surface molecules are concerned by photo excitation, the rate of electron emission depends on particle size.

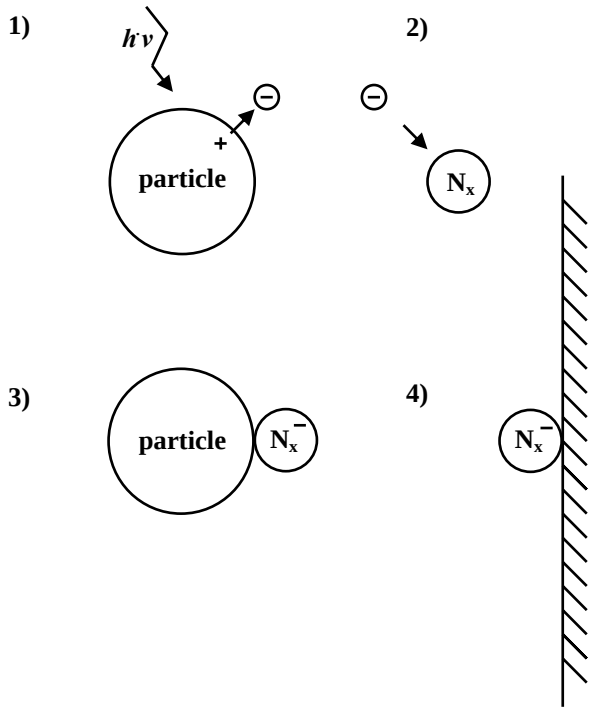

Figure 3.2.2.1: Mechanisms of photonic charging of nitrogen borne particles: 1) ionization of particles by photons 2) ionization of nitrogen molecules by collisions with electrons 3) recombination between particles and nitrogen ions 4) loss of nitrogen ions to the walls of the irradiated volume

The probability of ionization of particles is high when the photon energy Φ_{photon} of the exciting light is higher than the work function Φ_∞ of the particle material where the photon energy $\Phi_{\text{photon}} = \frac{h \cdot c_0}{\lambda_P}$ with $h = 6.626 \cdot 10^{-34}\,\text{Js}$ the Planck's constant, $c_0 = 2.998 \cdot 10^8 \frac{\text{m}}{\text{s}}$ the vacuum light velocity, and λ_P the wavelength of the exciting light. A critical wavelength λ_c is given by $\lambda_c = \frac{h \cdot c_0}{\Phi_\infty}$ which for SiO_2 (Φ_∞ = 5.0eV (von Ardenne [78], Fomenko [18])) leads to λ_c = 208nm.

The dynamic balance of the number concentration of negative ions n_i between photonic ionization and recombination can be expressed by (Maisels *et al.* [47])

$$\frac{\mathrm{d}n_i}{\mathrm{d}t} = \sum_{C_m} \sum_{R_P=R_{P\min}}^{R_{P\max}} \sum_{q=q_{\min}}^{q_{\max}} \left(\underbrace{\alpha_{q,R_P,C_m}^{q\to q+1} N_{q,R_P,C_m}}_{\text{photo charging}} - \underbrace{n_i \beta_{q,R_P,C_m}^{q\to q-1} N_{q,R_P,C_m}}_{\text{recombination}} \right) - \underbrace{\Delta_i}_{\substack{\text{ion losses} \\ \text{to the walls}}} \qquad (3.2.2.1)$$

where C_m represents a particle material, R_P the particle radius, q the number of elementary charges, N_{q,R_P,C_m} the number concentrations of particles in the fractions indicated by q, R_P, and C_m. Δ_i counts for diffusional ion losses to the walls. $\alpha_{q,R_P,C_m}^{q\to q+1}$ is the combination coefficient for photo charging from charge level q to $q+1$, $\beta_{q,R_P,C_m}^{q\to q-1}$ the combination coefficient for diffusion charging from charge level q to $q-1$.

The balance of the number concentration N_{q,R_P,C_m} of particles can be expressed by Maisels *et al.* [47]

$$\begin{aligned}\frac{\mathrm{d}N_{q,R_P,C_m}}{\mathrm{d}t} = &\underbrace{\alpha_{q-1,R_P,C_m}^{q-1\to q} N_{q-1,R_P,C_m} - \alpha_{q,R_P,C_m}^{q\to q+1} N_{q,R_P,C_m}}_{\text{photo charging}} \\ &+ \underbrace{n_i\left(\beta_{q+1,R_P,C_m}^{q+1\to q} N_{q+1,R_P,C_m} - \beta_{q,R_P,C_m}^{q\to q-1} N_{q,R_P,C_m}\right)}_{\text{diffusion charging}} .\end{aligned} \tag{3.2.2.2}$$

The combination coefficient $\alpha_{q,R_P,C_m}^{q\to q+1}$ for a spherical particle is given by (Burtscher *et al.* [8])

$$\alpha_{q,R_P,C_m}^{q\to q+1} = K_C\left(h\nu - \Phi^{q\to q+1}\right)^b \frac{I\pi R_P^2}{h\nu} \tag{3.2.2.3}$$

where K_c and b are a material dependent empirical constants, v the frequency of the light, and I the light intensity. b =2 is assumed for metal particles and particles from combustion processes.

For a spherical particle the work function $\Phi^{q\to q+1}$ is given by (Wood [84])

$$\Phi^{q\to q+1} = \Phi_\infty + \frac{e^2(q+1)}{4\pi\varepsilon_0 R_P} - \frac{5}{8}\cdot\frac{e^2}{4\pi\varepsilon_0 R_P} \tag{3.2.2.4}$$

where Φ_∞ is the work function of a plane surface, e the elementary charge and ε_0 the vacuum permittivity.

The ion attachment coefficient $\beta_{q,R_P,C_m}^{q\to q-1}$ is calculated by (Fuchs [20])

$$\beta_{q,R_P,C_m}^{q\to q-1} = \frac{4\pi R_P D_i}{\dfrac{4R_P D_i}{\delta^2 \overline{\nu}_i \alpha_{coll}}\cdot\exp\left(\dfrac{\phi(\delta,q)}{k_B T}\right) + \displaystyle\int_0^{\frac{R_P}{\delta}} \exp\left(\dfrac{\phi\left(\dfrac{R_P}{y},q\right)}{k_B T}\right) dy} . \tag{3.2.2.5}$$

D_i is the ion diffusion coefficient, $\overline{v}_i$ the mean thermal ion velocity, α_{coll} the collision probability (Wiedensohler [81]), T the gas temperature, and k_B the Boltzmann constant, δ is the radius of the absorbing sphere (Fuchs [20])

$$\delta = \frac{R_P}{Kn_i^{\,2}}\left(\frac{(1+Kn_i)^5}{5} - \frac{\left(1+Kn_i^{\,2}\right)(1+Kn_i)^3}{3} + \frac{2\left(1+Kn_i^{\,2}\right)^{\frac{5}{2}}}{15}\right) \tag{3.2.2.6}$$

with $Kn_i = \frac{2\lambda_i}{D_P}$ the Knudsen number for ions, λ_i the mean free path of the ions.

The electrical potential $\phi(l,q)$ between a particle and an ion is determined by Coulomb- and image charges

$$\phi(l,q) = \frac{e^2}{4\pi\varepsilon_0}\left(\underbrace{\frac{q}{l}}_{\text{Coulomb}} - K(l)\underbrace{\frac{R_P^3}{2l^2\left(l^2-R_P^2\right)}}_{\text{image}}\right). \tag{3.2.2.7}$$

ε_0 is the vacuum permittivity, l the distance between particle and ion. $K(l)$ is the dielectric correction factor depending on ε_r of the particle material (Wiedensohler [81]).

3.2.3 Thermionic charging of particles

For thermionic charging the dynamic balance between ionization and recombination can be expressed by

$$\frac{\mathrm{d}n_i}{\mathrm{d}t} = \sum_{C_m}\sum_{R_P=R_{P\min}}^{R_{P\max}}\sum_{q=q_{\min}}^{q_{\max}}\left(\underbrace{\upsilon_{q,R_P,C_m}^{q\to q+1}N_{q,R_P,C_m}}_{\text{thermionic charging}} - \underbrace{n_i\beta_{q,R_P,C_m}^{q\to q-1}N_{q,R_P,C_m}}_{\text{recombination}}\right) - \underbrace{\Delta_i}_{\substack{\text{ion losses}\\ \text{to the walls}}} \tag{3.2.3.1}$$

respectively

$$\begin{aligned}\frac{\mathrm{d}N_{q,R_P,C_m}}{\mathrm{d}t} &= \underbrace{\upsilon_{q-1,R_P,C_m}^{q-1\to q}N_{q-1,R_P,C_m} - \upsilon_{q,R_P,C_m}^{q\to q+1}N_{q,R_P,C_m}}_{\text{thermionic charging}} \\ &+ \underbrace{n_i\left(\beta_{q+1,R_P,C_m}^{q+1\to q}N_{q+1,R_P,C_m} - \beta_{q,R_P,C_m}^{q\to q-1}N_{q,R_P,C_m}\right)}_{\text{recombination}}.\end{aligned} \tag{3.2.3.2}$$

$\upsilon_{q,R_P,C_m}^{q\to q+1}$ is the coefficient for thermionic charging. Coming from the Richardson – Dushman formula (Ibach *et al*. [29]) it can be shown that

$$j = R^* T^2 \exp\left(-\frac{\Phi^{q\to q+1}}{k_B T}\right) \tag{3.2.3.3}$$

with the current area density j, the effective Richardson constant R^*. The coefficient for thermionic charging thus can be calculated for a particle with the surface area $\frac{\pi \cdot D_P{}^2}{4}$ by

$$\upsilon_{q,R_P,C_m}^{q\to q+1} = \frac{\pi}{4e} \cdot D_P{}^2 R^* T^2 \exp\left(-\frac{\Phi^{q\to q+1}}{K_B T}\right). \tag{3.2.3.4}$$

R^* depends on the material by the effective electron mass m_e^* and is given (Ibach *et al.* [29]) by $R^* = R_{\text{theor}} \cdot \frac{m_e^*}{m_{e0}}$, with $R_{\text{theor}} = \frac{2\pi \cdot e \cdot m_{e0} \cdot k_B{}^2}{h^3} = 1.2017 \cdot 10^6 \frac{\text{A}}{\text{m}^2\text{K}^2}$.

Table 3.2.3.1 gives the effective electron mass for several semiconductors.

Table 3.2.3.1: Effective electron mass for several semiconductors and oxides (Sze, [69])

material	m_e^* / m_{e0}
Si	**0.36**
Ge	**0.55**
GaAs	**0.067**
ZnO	**0.19**
SiO_2	**0.50**
Al_2O_3	**0.47**

3.3 Measurement of particle number concentrations with an electrometer

The measurement of number concentrations of aerosols in the sub micrometer range can be realized either by a condensation nucleus counter (CNC) (Argarwal *et al.* [2]) or by an electrometer. The process of evaporation and condensation coming along with a CNC requires laboratory conditions as to temperature and pressure. The main disadvantage of the electrometer compared to the CNC is a higher detection limit. A CNC is able to detect single particles. The detection limit of an electrometer is some orders of magnitude higher. Therefore the application of an electrometer as a particle counter requires comparatively high concentrations. High concentrations on the other hand are disadvantageous for the CNC because errors due to particle coincidence occur. Considering the conditions of industrial synthesis processes the measurement of particle concentrations can be performed by an electrometer only because it is not affected by the gas pressure and because the actual concentrations are very high. Furthermore an electrometer can rather easily be designed resistant against corrosion.

Within the electrometer the aerosol is passed through a filter which is electrically isolated against the housing and which is encapsulated by a conductive grid (figure 3.3.1).

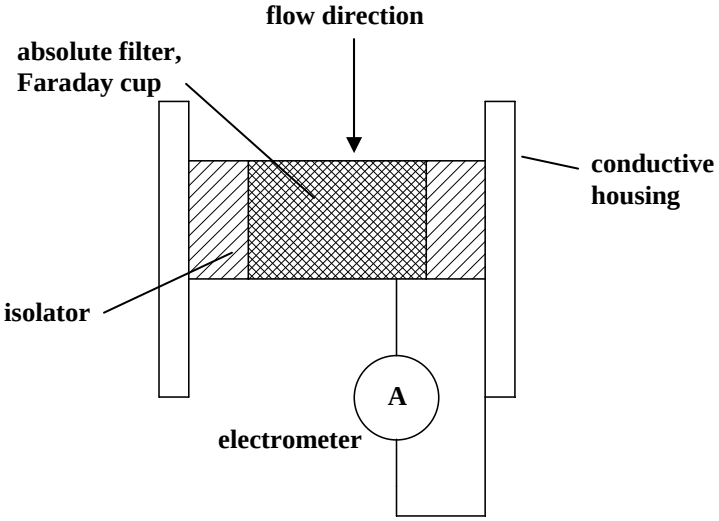

Figure 3.3.1: Electrometer for aerosols, principle

The filter itself does not have to be conductive because a change of the space charge inside a closed envelope leads to a change of the displacement density perpendicular to the enveloping surface after Maxwell's equation

$$\oiint_A \vec{D} \cdot \vec{n} \cdot \mathrm{d}A = \iiint_V \rho \cdot \mathrm{d}V \tag{3.3.1}$$

($\vec{D}$: electrical displacement vector, A: surface, ρ: space charge density V: volume)

Vice versa if the potential of the conductive envelope is kept constant, a compensating current can be measured. Depending on the concentration, the current is low. 1000 singly charged particles (one elementary charge) per cm^3 with a volume flow of 0.3l/min represent an electronic current of $8.04 \cdot 10^{-16}$ A.

A major requirement for an aerosol electrometer is a high sensitivity. Since the electrometer converts the input current to an output voltage the sensitivity S_{elec} can be defined as $S_{elec} = \frac{dU_{out}}{dI_{in}}$ where I_{in} and U_{out} represent the input current and the output voltage. In terms of the sample volume flow $\dot{V}_s$, the number of elementary charges q on the particles and the particle number concentration N_s of the sample gas the current equals $I_{in} = q \cdot \dot{V}_s \cdot N_s$ leading to $S_{elec} = \frac{1}{q \cdot \dot{V}_s} \cdot \frac{\mathrm{d}U_{out}}{\mathrm{d}N_{in}}$ for constant q and $\dot{V}_s$. It is appropriate to measure the electrometer sensitivity with an aerosol of which the charge and volume flow are known because on the one hand very small electronic currents can be realized and on the other because influences of the isolation and imperfections of the electronic devices thus are taken into account.

3.4 Differential mobility analysis under process conditions

3.4.1 Influence quantities

In principle four quantities can affect or impede the application of differential mobility analysis at powder synthesis processes:

1. Pressure
2. Concentration
3. Temperature
4. Humidity

The effects of temperature and humidity can be neglected because of the high dilution factor of the aerosol sampling.

3.4.1.1 Influence of pressure

The pressure is the most important influence quantity for the DMPS. Whereas the effects of concentration, temperature, and humidity are weakened by the sampling probe, this is not possible for the pressure since the pressure inside the DMA is equal to the process pressure. In the new LPDMPS the pressure has to be monitored and its influence has to be calculated. The pressure influences the mean free path λ between the gas molecules and subsequently the slip correction C_C, diffusional particle losses, particle coagulation, and the DMA transfer function. The pressure affects the maximum particle size the DMA can fractionate since the breakthrough voltage depends on pressure. The DMA volume flows depend on the pressure since for the new LPDMPS the gas flows are controlled by critical orifices and mass flow controllers.

3.4.1.1.1 Influence of pressure on particle slip

The slip correction

$$C_C = 1 + \frac{\lambda}{D_P} \cdot \left(2.514 + 0.8 \cdot \exp\left(-0.55 \cdot \frac{D_P}{\lambda} \right) \right) \qquad (3.4.1.1.1.1)$$

depends on the pressure by

$$\lambda(p) = \lambda_0(p_0) \cdot \frac{p_0}{p} \cdot \frac{T}{T_0} \cdot \frac{1 + \frac{S}{T_0}}{1 + \frac{S}{T}} \qquad (3.4.1.1.1.2)$$

with λ_0 = 66nm, p_0 = 1013mbar, T_0 = 273K. S is the Sutherland constant, which depends on the gas.

$$\lambda(p) = \lambda_0 \cdot \frac{p_0}{p} \qquad (3.4.1.1.1.3)$$

in case that $T = T_0$ with the pressure p, and the known mean free path λ_0 at $p = p_0$. Figure 3.4.1.1.1.1 gives the slip correction for various pressures.

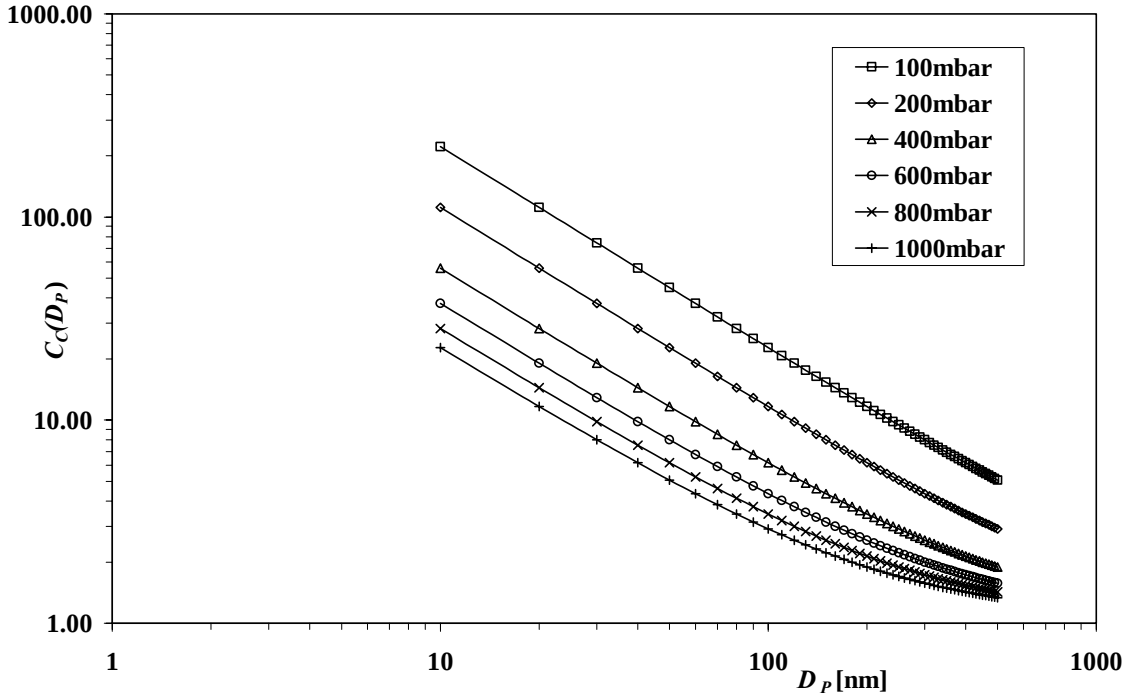

Figure 3.4.1.1.1.1: Slip correction as function of particle size for various pressures for nitrogen (λ_0 = 66nm and T = 273K) calculated with equations 3.4.1.1.1.1 and 3.4.1.1.1.2.

The following quantities and dependencies are affected by $\lambda(p)$:

1. The relationship between DMA voltage and particle size since the drag force $F_D \propto \frac{1}{C_C(D_P, p)}$.

2. The diffusion coefficient $D \propto C_C(D_P, p)$

3. The coagulation coefficient $K_A \propto C_C(D_P, p)$

Since the new LPDMPS will need considerable length of connection tubing, the effect of diffusional losses and coagulation has to be considered. Both mechanisms depend on the pressure and the particle size.

3.4.1.1.2 Influence of pressure on diffusional particle losses

Diffusion is the description of a transport along a concentration gradient of gas borne particles caused by random collisions with gas molecules. The particle flux J with the unit $\frac{1}{\mathrm{cm}^2 \cdot \mathrm{s}}$ is given by Fick's first law of diffusion

$$J = -D\frac{dN}{dx} \tag{3.4.1.1.2.1}$$

where D is the diffusion coefficient and $\frac{dN}{dx}$ the particle concentration gradient. In terms of the Boltzmann constant k_B, the temperature T, the slip correction C_C, the dynamic viscosity η and the particle size D_P, the diffusion coefficient D is determined by (Hinds [24])

$$D = \frac{k_B \cdot T \cdot C_C(D_P, p)}{3\pi \cdot \eta \cdot D_P}. \tag{3.4.1.1.2.2}$$

Walls of pipes are a particle sink causing a concentration gradient and a particle flux in radial direction of the pipes.

In Hinds [24] an analytical description for particle losses along a pipe is given for atmospheric pressure. Depending on the dimensionless parameter

$$\mu = \frac{D \cdot l_P}{\dot{V}} \tag{3.4.1.1.2.3}$$

the fraction P of particles passing the pipe can be calculated by

$$P = 1 - 5.5\mu^{\frac{2}{3}} + 3.77\mu \quad \text{for} \quad \mu < 0.007 \tag{3.4.1.1.2.4}$$

respectively

$$P = 0.819\exp(-11.5\mu) + 0.0975\exp(-70.1\mu) + 0.0325\exp(-179\mu) \quad \text{for} \quad \mu > 0.007 \tag{3.4.1.1.2.5}$$

with l_P the length of the pipe and $\dot{V}$ the aerosol volume flow through pipe. The fraction P of particles passing the pipe decreases with decreasing pressure. P is independent from the diameter of the pipe. Figure 3.4.1.1.2 shows the fraction $P(D_P)$ of particles which pass a pipe with a length of 1m for various size D_P and pressure p as calculated with equations 3.4.1.1.2.2 to 3.4.1.1.2.5.

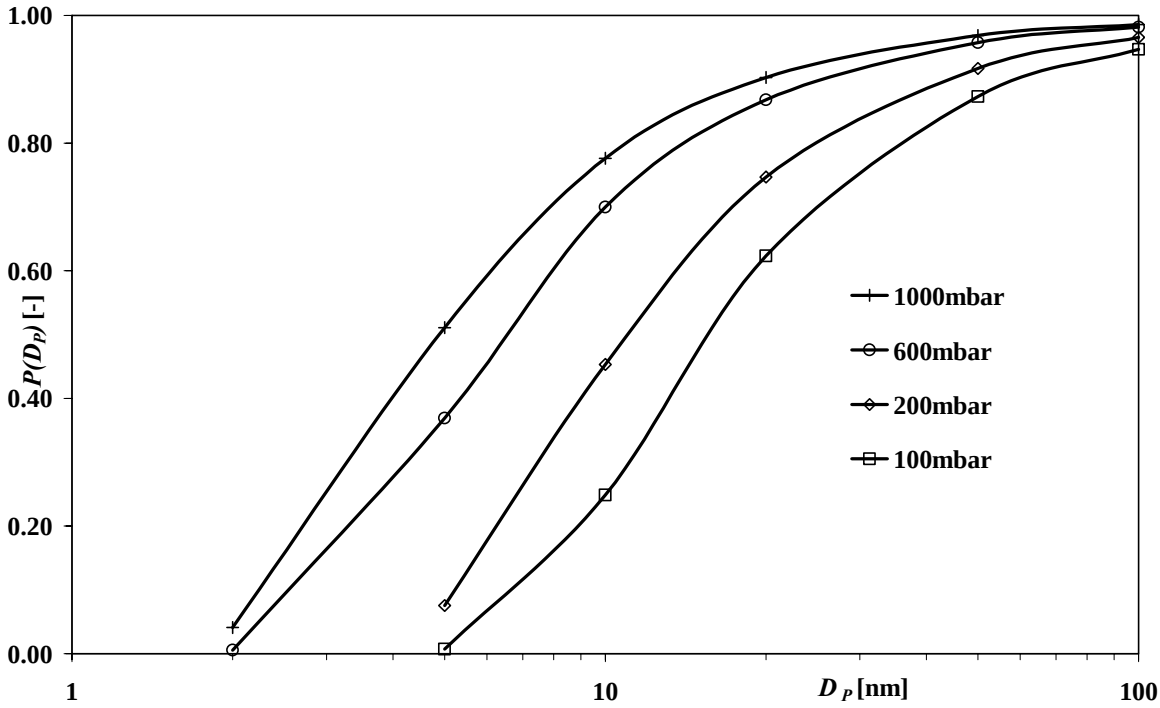

Figure 3.4.1.1.1.2: Fraction $P(D_P)$ of particles passing a pipe with a length of 1m for various size D_P and pressure p as calculated with equations 3.4.1.1.2.2 to 3.4.1.1.2.5

3.4.1.1.3 Influence of pressure and concentration on coagulation

Particle coagulation is the growth of particles by particle collisions. It leads to an increase of the mean particle diameter and simultaneously to a decrease of the concentration. For coagulation, forces must be present which cause a relative movement among the particles. If external forces, e.g. gravitation or coulomb forces are absent, the relative movement is only due to diffusion and is called thermal coagulation. It is assumed that diffusion is the only mechanism driving the coagulation, because gravitation is negligible and because the mean charge of the particles is zero. An expression for the time depending concentration $N(t)$ and the particle diameter $D_P(t)$ for a monodisperse aerosol is given by (Hinds [24])

$$N(t) = \frac{N_0}{1 + N_0 \cdot K_A \cdot t} \tag{3.4.1.1.3.1}$$

respectively

$$N_0 = \frac{N(t)}{1 - N(t) \cdot K_A \cdot t} \tag{3.4.1.1.3.2}$$

and

$$D_P(t) = D_{P0} \cdot \sqrt[3]{\frac{N_0}{N(t)}} \tag{3.4.1.1.3.3}$$

where $K_A = \frac{4\pi \cdot D_P \cdot D}{\frac{D_P}{D_P + g} + \frac{4D}{c \cdot D_P}}$ is the coagulation coefficient with $g = \left(\frac{(D_P + l)^3 - \left(D_P{}^2 + l^2\right)^{\frac{3}{2}}}{3D_P \cdot l} - D_P \right)$, $l = \frac{8D}{\pi \cdot c}$, $c = \sqrt{\frac{8k_B \cdot T}{\pi \cdot m_m}}$, and m_m the molecular mass (Flagan *et al*. [16]). N_0 is the initial concentration and D_{P0} the initial size. Pressure dependency comes by the diffusion coefficient $D = f(C_C)$. If for example N_0 = $10^6 \mathrm{cm}^{-3}$, D_P = 100nm, p = 600mbar, t = 29.8s (typical for the new LPDMPS) the agglomeration coefficient $K_A = 4.21 \cdot 10^{-16} \frac{\mathrm{m}^3}{\mathrm{s}}$, the decrease of the concentration is 1.24 % and the increase of the size of the particles 0.42%. K_A is assumed to be constant. The impact on the concentration will be considered in the calculation of the number size distribution. The particle size shift will be neglected.

3.4.1.1.4 Influence of pressure on DMA transfer function

The half width β_{Z_P} of a DMA is determined by the dimensionless Peclet number *Pe* which is the ratio of particle convective to diffusive transport inside the DMA (Flagan [17]).

$$Pe = \frac{v_E b}{D} \tag{3.4.1.1.4.1}$$

where v_E is the particle velocity due to the electrical field, b the distance between the electrodes, and D the particle diffusion coefficient. For the RDMA

$$v_E = \frac{\left(\dot{V}_c + \dot{V}_e\right)}{2\pi\left(R_2{}^2 - R_1{}^2\right)} \tag{3.4.1.1.4.2}$$

leading to

$$Pe_{RDMA} = \frac{b\left(\dot{V}_c + \dot{V}_e\right)}{2\pi\left(R_2{}^2 - R_1{}^2\right)} \cdot \frac{1}{D} \tag{3.4.1.1.4.3}$$

The Peclet number allows comparing DMA of different designs for different flow rates, voltages, and particle size ranges. Flagan [17], Fissan *et al.* [15], and Rosell-Llompart *et al.* [61] have shown that β_{Z_P} depends on *Pe* no matter of the DMA type and dimensions. Figure 3.4.1.1.4.1 shows β_{Z_P} as a function of *Pe* for a radial DMA (SMEC) and a cylindrical DMA (TSI-short) as determined by Fissan *et al*. [14].

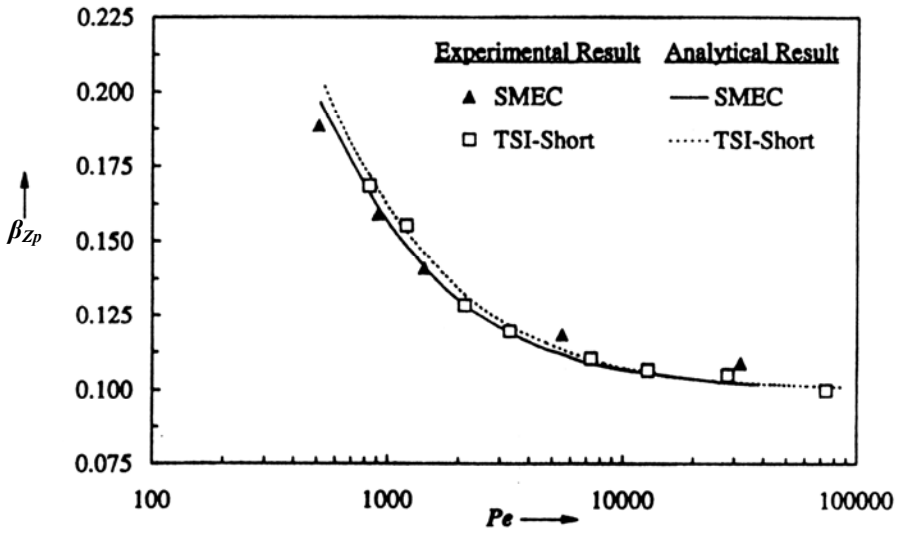

Figure 3.4.1.1.4.1: β_{Zp} as a function of *Pe* for a radial DMA and a cylindrical DMA (Fissan *et al.* [14])

Karlsson *et al.* [33] presented an analytical expression for $\beta_{Z_P}(Pe)$ assuming a triangular transfer function considering diffusional broadening.

$$\beta_{Z_P} = \frac{\dot{V}_a}{\dot{V}_c}\sqrt{1+\left(\frac{1}{0.15\left(1.69\left(1-\exp\left(-\left(\frac{Pe}{105}\right)^{0.33}\right)\right)-0.69\right)^2}-1\right)\left(\frac{0.15\dot{V}_c}{\dot{V}_a}\right)^2} \qquad (3.4.1.1.4.4)$$

For the TSI short $\beta_{Z_P}(Pe)$ has been calculated by equation 3.4.1.1.4.4 and compared to the experimental data of Fissan *et al.* [14]. Good agreement has been achieved. The result is shown in figure 3.4.1.1.4.2. In the free molecular regime (*Kn*>>1) the particle diffusion coefficient *D* is inversely proportional to the pressure (Kousaka *et al.* [38], Seto [65]).

$$D = D_{ref}\frac{p_{ref}}{p} \qquad (3.4.1.1.4.5)$$

where D_{ref} is a known diffusion coefficient at the known pressure p_{ref}. In the transient regime ($Kn \approx 1$) $D \propto C_C(p)$ leading to

$$D = D_{ref}\frac{C_C(p_{ref})}{C_C(p)} \qquad (3.4.1.1.4.6)$$

which is pressure dependent.

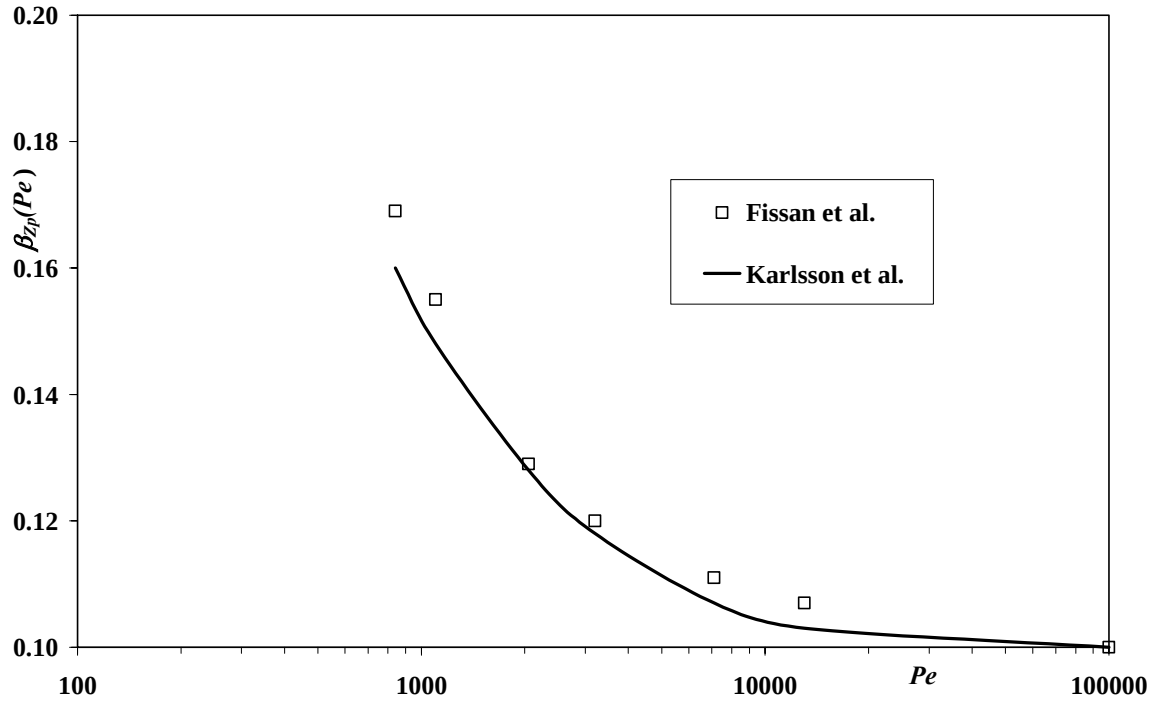

Figure 3.4.1.1.4.2: β_{Zp} as a function of *Pe* as calculated by equation 3.4.1.1.4.4 compared to experimental results for the TSI short by Fissan *et al.* [14]

To theoretically investigate the influence of the pressure on the transfer function, the Peclet number has been calculated for the physical DMA dimensions given in chapter 4.5 and the volume flows $\dot{V}_c = \dot{V}_e = 3.0\mathrm{l\,min^{-1}}$ for various pressures using equation 3.4.1.1.4.4. The result is given in figure 3.4.1.1.4.3.

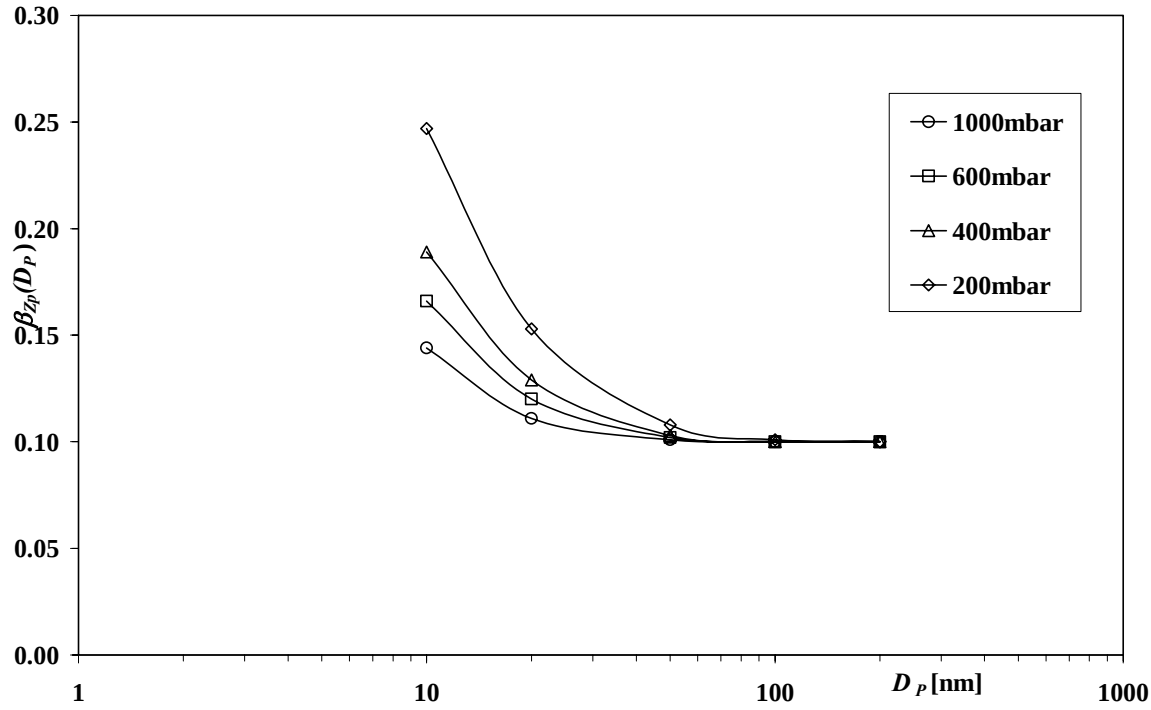

Figure 3.4.1.1.4.3: β_{Zp} as a function of the particle size for different pressures calculated by equation 3.4.1.1.4.4 (Karlsson *et al.* [33])

Karlsson *et al.* [33] have shown that size dependent diffusional particle losses in the DMA can be treated as particle losses in a pipe when the DMA is represented by a characteristic length l_{DMA}. This characteristic length l_{DMA} can be determined by a single measurement of diffusional particle losses in the DMA for one particle size. Karlsson *et al.* [33] found a good accuracy by application on 4 different types of DMA.

In order to estimate the influence of the pressure on the transmission efficiency η_{DMA} (chapter 3.1) and the height of the transfer function α_{Z_P} the Vienna DMA (Winklmayr *et al.* [82]) has been taken as an example. Karlsson *et al.* [33] determined a characteristic length of 4.6m to characterize the diffusional losses for the Vienna DMA. The transmission efficiency η_{DMA} has been calculated by equations 3.4.1.1.2.2 to 3.4.1.1.2.5. From the transmission efficiency η_{DMA} the height of the transfer function α_{Z_P} has been calculated by $\alpha_{Z_P} = \frac{\eta_{DMA}\dot{V}_a}{\beta_{Z_P}\dot{V}_c}$. Figure 3.4.1.1.4.4 and figure 3.4.1.1.4.5 show the results of the calculations for η_{DMA} and for α_{Z_P}.

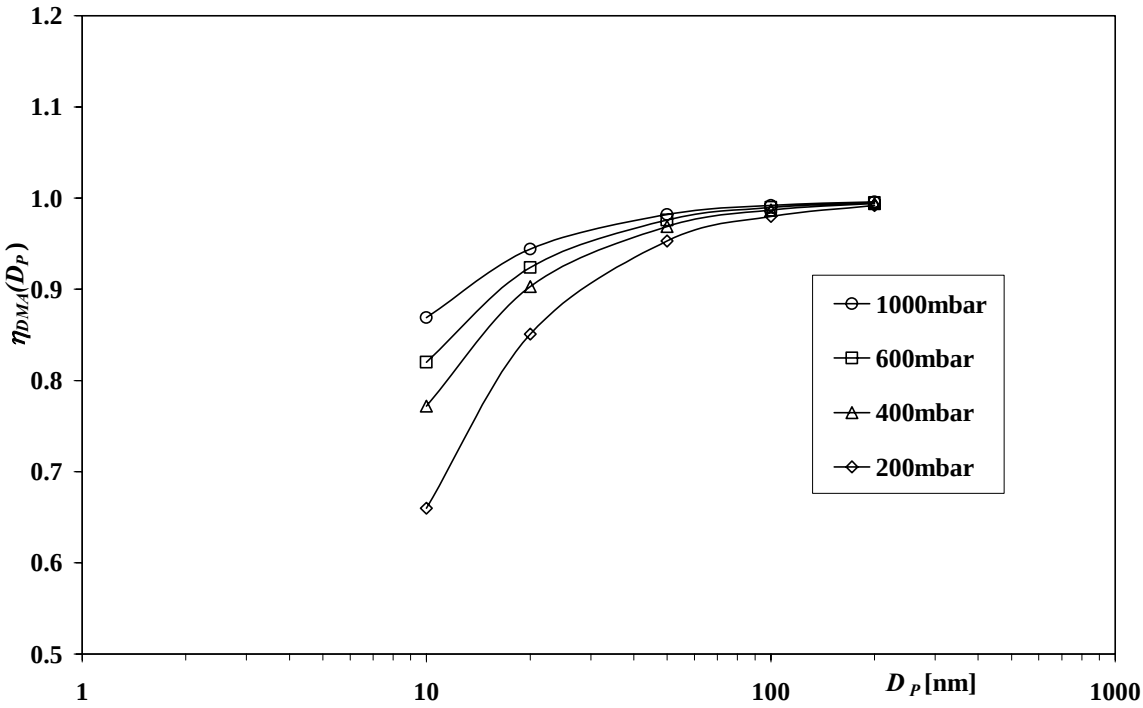

Figure 3.4.1.1.4.4: η_{DMA} as a function of the particle size for different pressures calculated by equation 3.4.1.1.2.2 to 3.4.1.1.2.5 for the Vienna DMA (Karlsson *et al.* [33])

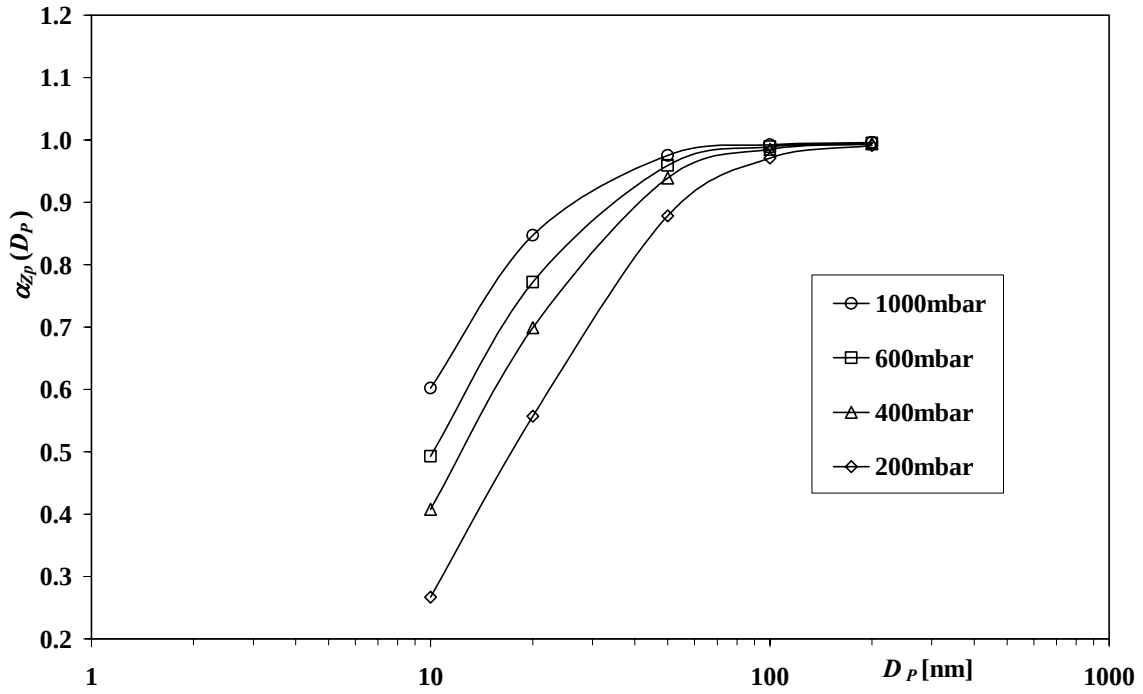

Figure 3.4.1.1.4.5: α_{Zp} as a function of the particle size for different pressures calculated by equation 3.4.1.1.2.2 to 3.4.1.1.2.6 for the Vienna DMA (Karlsson *et al.* [33])

The calculations of the transfer function imply that for decreasing pressures reduced resolution and transmission efficiency have to be expected. For example for $D_P = 10\text{nm}$ a reduction of the pressure from 1000mbar to 400mbar leads to an increase of β_{Z_P} of 20%, a decrease of α_{Z_P} of 26%, and a decrease of η_{DMA} of 11%. A remedy against reduced resolution and transmission efficiency could be to increase the DMA gas volume flows for reduced pressures (keep mass flows constant). Since the LPDMPS shall be used for various pressures and the gas flows are controlled by critical orifices which lead to constant volume flows, a reduced DMA resolution is preferred to an exchange of the critical orifices for any pressure as will be discussed in chapter 4.

3.4.1.2. Influence of temperature and breakthrough voltage on particle size range

The maximum voltage which can be applied at the electrodes of the DMA is restricted by the voltage at which ionization of the gas occurs. The corresponding electrical field strength depends on the distance between the electrodes and the pressure.

Under standard conditions for a static homogeneous electrical field and a distance of 15mm between the electrodes the breakthrough field strength E_{bth} is about 31KV/cm (Hasenpusch [23]). The dependency on temperature and pressure is given by (Hasenpusch [23])

$$E_{bth}(p,T) = \frac{31\text{KV}}{\text{cm}} \cdot \frac{p}{p_0} \cdot \frac{T_0}{T} . \qquad (3.4.1.2.1)$$

The electrical breakthrough limits the upper particle size to be fractionated. The maximum particle size is the particle size corresponding to the breakthrough voltage.

The influence pressure on the maximum particle size is not by the breakthrough voltage only, but furthermore by a change of the viscosity and slip correction. Thus the pressure gravely reduces the upper particle size limit of the DMA.

3.5 Differential mobility particle sizer (DMPS)

A DMPS is an instrument which automatically measures particle size number distributions of aerosols. Its basic principle is the differential mobility analysis. It consists of the components introduced in the preceding chapters. The entire DMPS is sketched in figure 3.5.1.

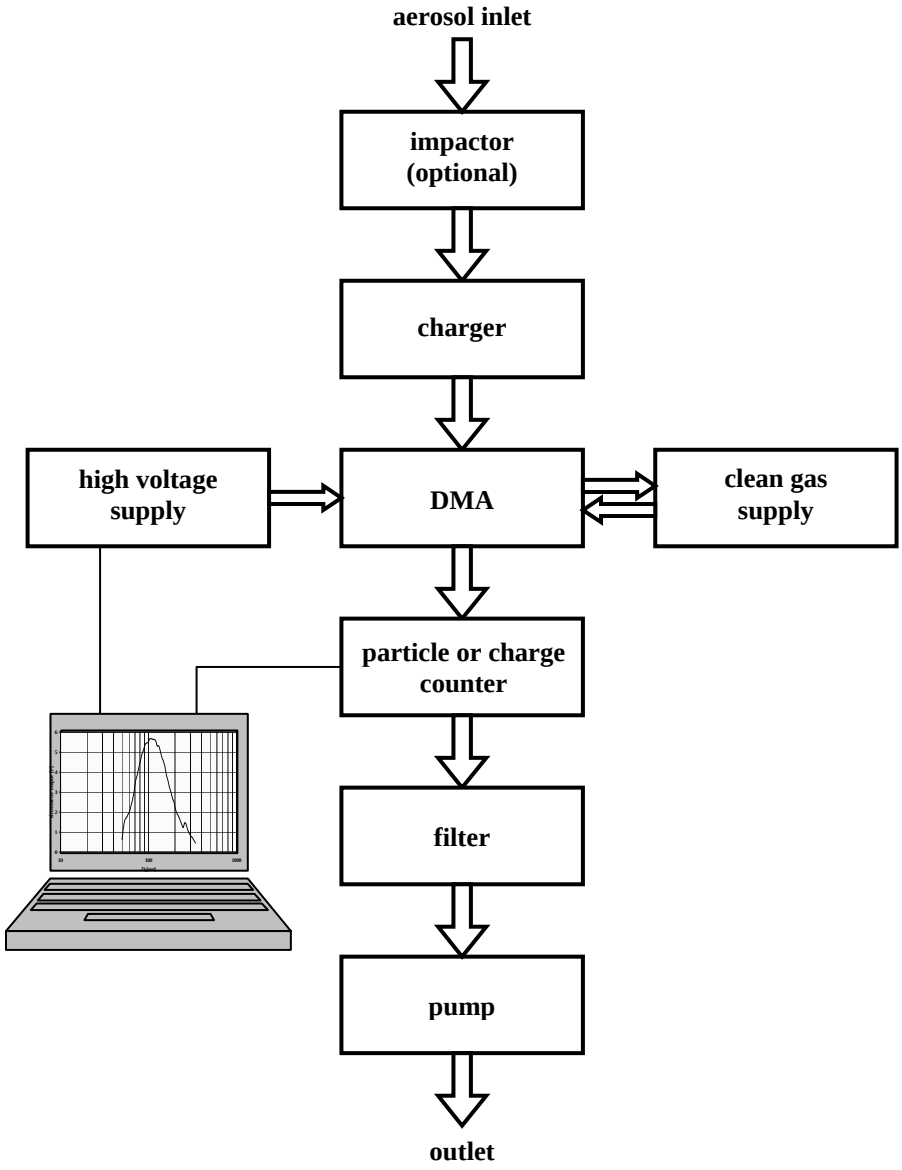

Figure 3.5.1: Components of a differential particle sizer (DMPS)

Particle sizing by the differential mobility analysis goes back to work by Knutson *et al*. [36] who introduced a system consisting of a Kr-85 neutralizer, a DMA and an electrometer for size distribution measurements of aerosols. In 1984 TSI Inc. presented a commercial, automatic DMPS measurement setup (Keady *et al*. [34]).

The main task of the computer is to adjust the DMA high voltage and to record the corresponding detector signal. DMPS are commercially built for example by TSI^{Inc} or Grimm GmbH. State of the art in particle size analysis of submicron aerosols is the scanning mobility particle sizer (SMPS) by TSI^{Inc}. Its major innovation of the scanning mobility particle sizer (SMPS) compared to the DMPS is the correction for the delay time

between DMA voltage and detector response by the computer thus realizing a faster measurement time. Depending on the aerosol to be measured an impactor is used to remove particles above the size range of the DMA, because otherwise no proper consideration of multiple charges is possible (chapter 4.7). In case that the aerosol does not contain particles above the upper size limit an impactor is not necessary. The sample gas flow usually is provided by a pump at the end of the chain of components. For a new measurement instrument a technique has to be applied which continuously pulls out a high diluted sample of the process aerosol without changing the pressure. This is realized by a new sampling probe, which is an important modification of customary measurement instrumentation (chapter 4.2).

In this chapter the basic mechanisms of charger, DMA, and detector are introduced and the effects of the process conditions on the physical mechanisms concerning the differential mobility analysis are pointed out. The development and characterizations of the components for the new LPDMPS are presented in chapter 4.

4 Development of a DMPS for industrial powder synthesis processes

4.1 Components of a DMPS for industrial powder synthesis processes

Measurements of particle number size distributions in particle synthesis processes need several operations for which convenient methods have to be found or realized by new physical components. Examples are the measurement and control of volume flows or the adaptation of particle charging and counting techniques to process conditions. A sample has to be taken from the process, while a high grade dilution is necessary in order the stop chemical reactions and particle coagulation. Therefore a sampling and dilution probe has been developed. The measurement system requires several gas volume flows. These flows are small and have to be very stable. Since the concerned synthesis processes show considerable fluctuations of the pressure, the task to stabilize and control the gas flows under the given conditions is not trivial.

For the charging of the particles the irradiation by ultra violet light has been chosen since it avoids the risk of radioactive contamination of the process from a radioactive source. The charge distributions of the ultra violet irradiation unit are determined by numerical solution of ion population balance equations as proposed by Maisels *et al*. [47].

The fractionation of the charged particles is realized by a DMA which has been newly designed and investigated in the laboratory. The detection of the fractionated particles is performed by an electrometer especially designed for the given conditions.

For the calculation of number size distributions out of the raw data (data inversion) the properties of the charger, the DMA, and the electrometer have to be known. Therefore detailed investigations of these components are necessary. For the calculation a personal computer equipped with additional hardware is used. Software has been developed which controls the sequence of the measurement and performs the calculation. Data inversion (chapter 4.7) is an outstanding problem for particle size measurements and has been subject of many publications. Therefore the calculation of number size distributions out of DMPS raw data is of special interest.

The realization of the components of a new low pressure DMPS (LPDMPS) and its operation is described in chapters 4.2 to 4.7.

4.2 Sampling probe

The purpose of the sampling probe is to sample and to dilute at the same time. The sampling probe has to provide a constant stream of aerosol for the time necessary to perform the measurement of the size distribution (about five minutes). The particle concentrations within industrial reactors for the synthesis of nanoscale powders are in the range of $10^8 cm^{-3}$ to $10^{14} cm^{-3}$, the temperatures up to 1200°C. A high grade of dilution is necessary to stop chemical reactions and particle coagulation (Lesniewski *et al*. [42], Biswas [4]). Therefore a jet pump has been constructed which is driven by nitrogen. The jet pump provides locally a lower pressure in the contraction of the flow and thus causing a certain amount of gas being withdrawn out of the process and diluted (Figure 4.2.1). Immediate dilution with nitrogen is provided at the entrance of the probe so that the jet pump draws in an already diluted sample. In principle with a cascade of jet pumps any dilution ratio is possible (figure 4.2.2). The probe has been crafted out of Hastelloy C4 to avoid corrosion by HCl. The probe has to fit into standard connections used at synthesis reactors, which lead to the design shown in appendix A2. The major part of the sampled aerosol is abandoned and flows back into the process. The nitrogen flows which determine the dilution are controlled by mass flow controllers.

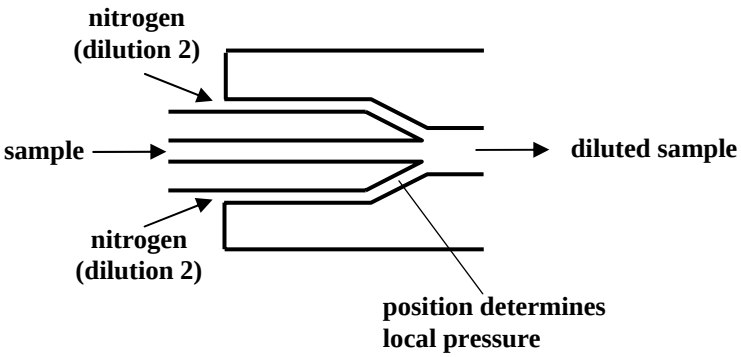

Figure 4.2.1: Jet pump, principle. The length of the insert determines the dilution ratio of the jet pump.

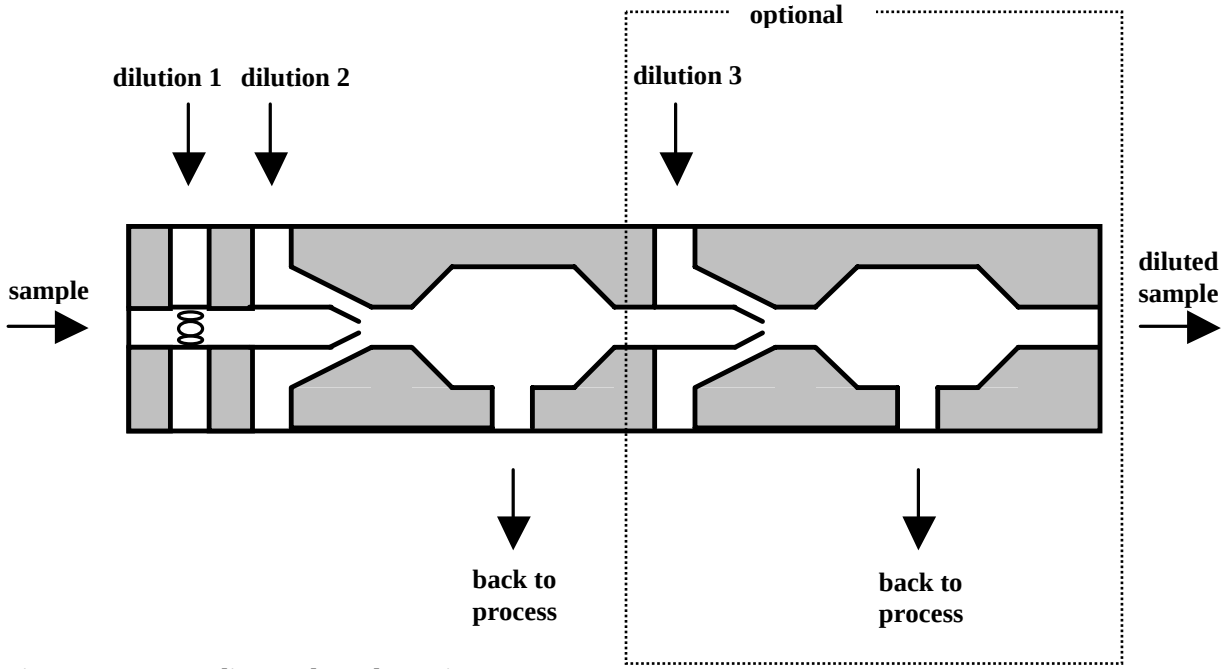

Figure 4.2.2: Sampling probe, schematic

It is not possible to predict the dilution factor of the jet pump out of the geometry because the dimensions within the probe are so small and fabrication imprecision causes too large uncertainties. The gap of the jet pump which determines the velocity of the nitrogen measures only a few tenths of millimeter. Since the probe had to be crafted in two parts, the amount of withdrawn gas can be varied by using different inserts as sketched in figure 4.2.3 with different lengths l_i. The inserts end at positions with different pressures. The dilution of the jet pump in connection with the inserts has been investigated experimentally. The setup for the measurement of the dilution ratios for the different inserts is sketched in figure 4.2.4.

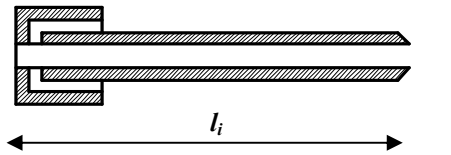

Figure 4.2.3: Insert for the sampling probe

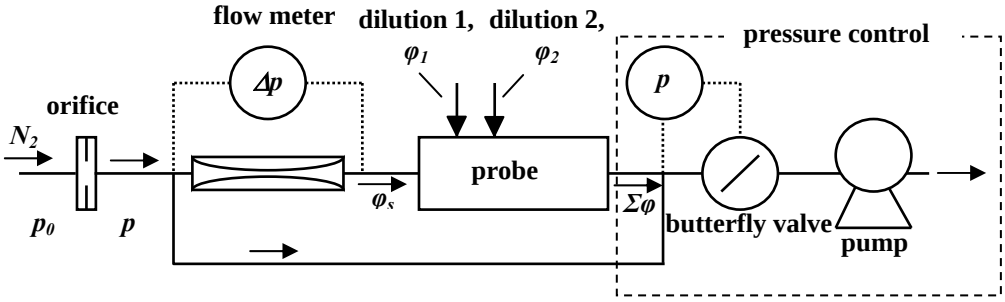

Figure 4.2.4: Setup for the investigation of the dilution ratio for the different inserts for various pressures

φ_s denote the sampled flow into the sampling probe, φ_1 the flow of dilution 1, φ_2 the flow of dilution 2. Σ_φ is the sum of the φ_s, φ_1, and φ_2. With the setup in figure 4.2.4 the amount of gas which is drawn has been determined by the probe using inserts with different lengths. The purpose of these experiments has been to find the insert with the optimum dilution ratio.

The amount of gas sampled by the jet pump has been measured by measuring the pressure loss in a capillary tube with a differential pressure gauge, which had been calibrated for several pressures. The transition into the low pressure region has been realized by an orifice. The pressure has been controlled by a vacuum pump and a butterfly valve in connection with an absolute pressure gauge. The surplus of gas flows through a bypass. The sum $\varphi_s + \varphi_1$ depends on φ_2 and is constant for constant φ_2. φ_s cannot exceed a threshold $\varphi_{th} = \varphi_s + \varphi_1 = \varphi_1\big|_{\varphi_s=0}$. Under process conditions φ_{th} can be determined by increasing φ_1 until no particles are detected by the electrometer when the DMA voltage is constant. Then $\varphi_{th} = \varphi_1\big|_{\varphi_s=0}$ can be read from the mass flow controller for φ_1. In order to compare the sampled gas flow φ_s all flows are given in standard liters per minute (slm). The unit slm denotes volume flows related to atmospheric (standard) pressure p_0 at

standard temperature (T_0=20°C) $\left(\dot{V}[\text{slm}] = \dot{V}[\text{l min}^{-1}] \cdot \frac{p}{p_0}\right)\Big|_{T=T_0}$. For the inserts with the lengths 31.4mm and 31.6mm φ_{th} (φ_2) is given in figures 4.2.5 and 4.2.6.

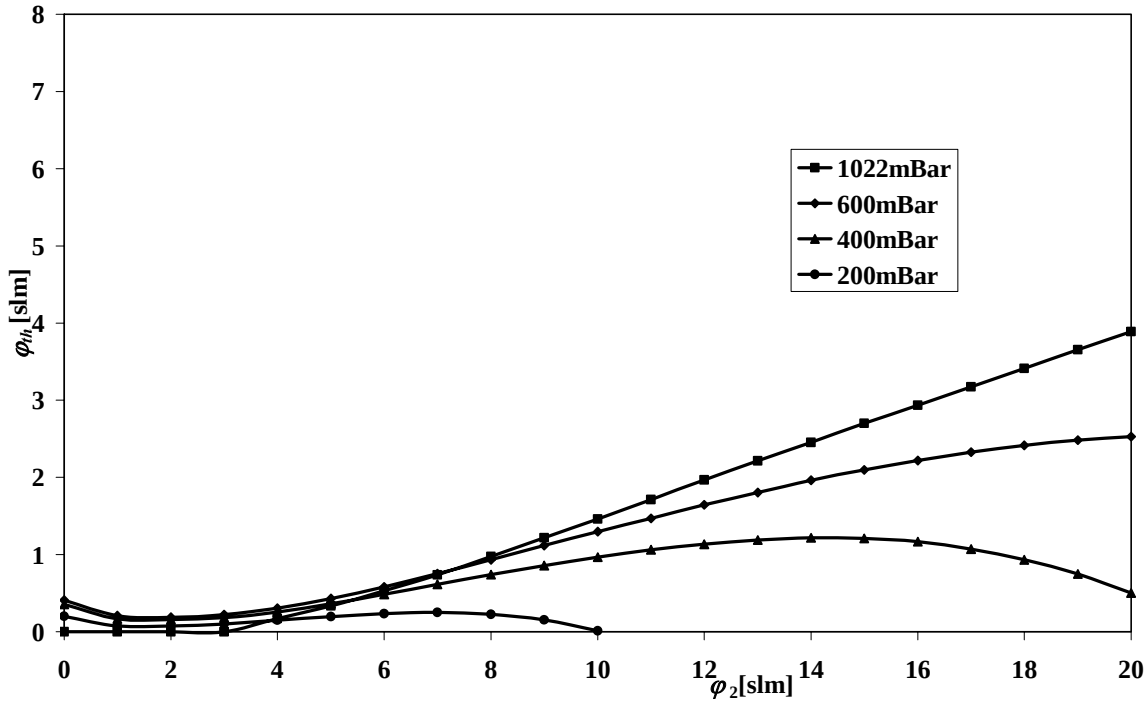

Figure 4.2.5: φ_{th} as a function of φ_2 for l_i = 31.4mm.

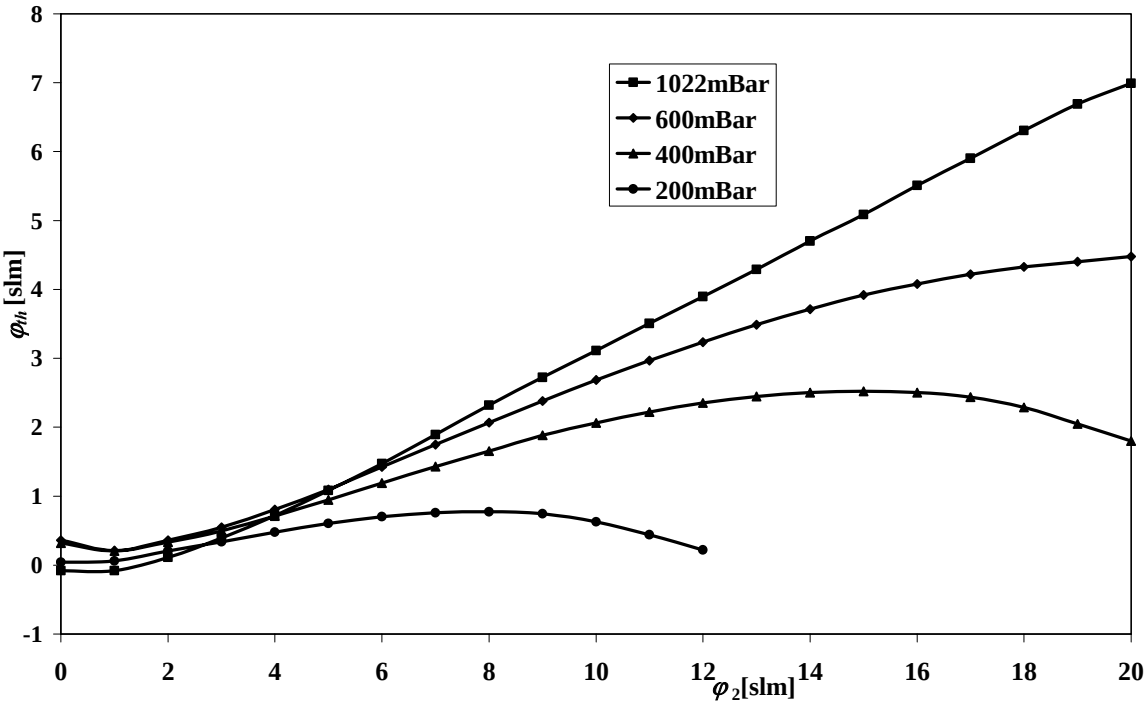

Figure 4.2.6: φ_{th} as a function of φ_2 for l_i = 31.6mm.

The dilution ratio of the sampling probe D_{SP} is given by

$$D_{SP} = \frac{\varphi_s}{\varphi_s + \varphi_1 + \varphi_2} = \frac{\varphi_{th} - \varphi_1}{\varphi_{th} + \varphi_2}. \qquad (4.2.1)$$

Cleaning of the probe

Application of the probe showed that deposition of particles on the walls more and more narrows the drilling of the probe. In order to free the probe, a magnetic valve is used to apply backwards pressure pulses of nitrogen. This magnetic valve is activated before each measurement. In every case 5 pulses with duration of 200ms and a pressure of 5bar could free the probe from deposited material.

4.3 Control of DMA volume flows

An accurate determination of number size distributions by differential mobility analysis requires defined gas flows because the gas volume flows determine the DMA transfer function (equation 3.1.3.1). The synthesis processes the new LPDMPS shall be applied to, come along with various pressures, pressure fluctuations, and acid compounds which complicate the control of the flows. The flows to be controlled are the four dilution flows and the four DMA flows. For DMA theory particle velocity plays a major role, therefore the gas flows are given in terms of volume flow rates $\dot{V}$ [lmin^{-1}]. $\dot{V}_a$ and $\dot{V}_c$ flow into the DMA , $\dot{V}_e$ and $\dot{V}_s$ flow out of the DMA as illustrated in figure 4.3.1. $\dot{V}_c$ is controlled by a mass flow controller which ensures constant mass flow. Since the pressure inside the LPDMPS is monitored, $\dot{V}_c$ can be calculated out of the clean gas mass flow. $\dot{V}_s$ and $\dot{V}_e$ cannot be controlled by mass flow controllers because of the presence of HCl but are controlled by critical orifices (chapter 4.3.1). The aerosol flow must not be controlled since $\dot{V}_a = \dot{V}_e + \dot{V}_s - \dot{V}_c$.

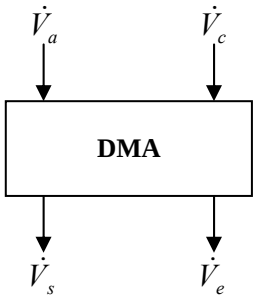

Figure 4.3.1: DMA volume flows

4.3.1 Critical orifices for the control of the DMA gas flows

The DMA aerosol and sheath gas are controlled by two critical orifices and a mass flow controller. An orifice is called critical, when the gas velocity v_g equals the sonic speed v_s, which it cannot exceed and which for air is 344m/s and for nitrogen 348 m/s at $T = 293$K and $p = p_0 = 1013$mbar.

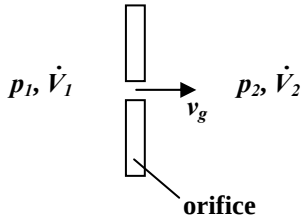

Figure 4.3.1.1: Critical orifice

The critical pressure p_c depends on the pressure p_1 upstream of the orifice and the adiabatic coefficient κ

$$p_c = p_1 \cdot \left(\frac{2}{\kappa + 1} \right)^{\frac{\kappa}{\kappa - 1}} . \tag{4.3.1.1}$$

For air $\kappa = 1.40$ leading to $p_c = 0.53 \cdot p_1$. The critical mass flow $\dot{m}_c$ for a gas passing a critical orifice is given by (Wutz *et al.* [85])

$$\dot{m}_c = A_{CO} \cdot p_1 \cdot \left(\frac{2}{\kappa + 1} \right)^{\frac{1}{\kappa - 1}} \cdot \sqrt{\frac{2\kappa}{\kappa + 1} \cdot \frac{M_{mol}}{R_{gas} \cdot T}} \tag{4.3.1.2}$$

with A_{co} the cross sectional area of the orifice, M_{mol} the mole mass, $R_{gas} = 8.314 \frac{\text{Pa} \cdot \text{m}^3}{\text{mol} \cdot \text{K}}$ the general gas constant and T the temperature. The critical mass flow $\dot{m}_c$ is the maximum mass flow which can pass an orifice. As long as $p_2 \le p_c$ $\dot{m}_c$ is independent from p_2. For air and nitrogen the diameter $d_{co} = \sqrt{\frac{4A_{co}}{\pi}}$ necessary to obtain a flow rate $\dot{V}_1$ (upstream the orifice) can be calculated by

$$d_{co} = \sqrt{\frac{4\dot{V}_1 \cdot \rho_{gas}}{\pi \cdot p_0 \cdot \left(\frac{2}{\kappa + 1} \right)^{\frac{1}{\kappa - 1}} \cdot \sqrt{\frac{2\kappa}{\kappa + 1} \cdot \frac{M_{mol}}{R_{gas} \cdot T}}}} \tag{4.3.1.3}$$

since the mass flow depends on the volume flow, density, and pressure by $\dot{m} = \dot{V}_1 \cdot \rho_{gas} \cdot \frac{p_1}{p_0}$. For nitrogen ($M_{mol}$ 28.02kg/kmol, ρ_{gas} = 1.250kg/m^3) d_{co,N_2} can be calculated by

$$d_{co,N_2} = \sqrt{112.757 \cdot 10^{-9} \cdot \frac{\dot{V}_1}{1\,\mathrm{l\,min^{-1}}}}\,\mathrm{m} \qquad (4.3.1.4)$$

assuming p_0 = 1013mbar and T = 293K. The values for d_{co,N_2} are 183.92µm for $\dot{V}_1 = 0.30\,\mathrm{l\,min^{-1}}$ and 581.61µm for $\dot{V}_1 = 3.0\,\mathrm{l\,min^{-1}}$.

The orifices, which have been machined, have approximate diameters of 0.2mm and 0.6mm. The actual cross sectional areas could not be determined in lack of an accurate measuring method. The volume flows have been measured under atmospheric pressure using a Gillibrator™ standard flow meter. The measured volume flows for $\dot{V}_1$ have been 0.27l/min respectively 2.40l/min which lead to an ideal (non diffusional) half width $\beta_{Zp,\mathrm{ideal}} = 0.1125$.

4.3.2 Measurement of the aerosol volume flow

The aerosol volume flow under process conditions has to be monitored out of two reasons: 1. For the balancing of the DMA volume flows under process conditions. 2. To make sure that during the size distribution measurement a constant aerosol flows is provided. A gas volume flow can be measured by measuring the pressure drop along a pipe. In case of laminar flow the pressure drop Δp along a pipe is given by (Stöcker [66])

$$\Delta p = \frac{8 \eta l_P \dot{V}}{\pi \cdot r_P^4} \qquad (4.3.2.1)$$

in terms of the dynamic viscosity η, the length of the pipe l_P, the volume flow $\dot{V}$, and the radius of the pipe r_P. For the measurement of the aerosol volume flow a pipe with a length of l_P = 100mm and a radius r_P = 1.5mm has been used in connection with a sensitive differential pressure gauge (µbar range). The instrument has been calibrated for different pressures in the laboratory. For $\dot{V}_a = 0.3\,\mathrm{l\,min^{-1}}$, $\eta = 17.8 \cdot 10^6$ Pas (N_2, 293K), equation 4.3.2.1 leads to Δp = 44.8µbar, the measurement (p=1018mbar) has revealed a pressure drop of 53µbar.

4.3.3 Equalization of aerosol flow

It turned out that fluctuations of the pressure inside the reactor can cause fluctuations of the gas flow downstream the probe. It even occurred that gas flows backwards to the reactor. Therefore the aerosol flow coming out of the sample probe had to be equalized. Analogous to RC-low pass filter in electrical engineering a low pass filter consisting of a flow resistance and storage can be used to equalize gas flows (figure 4.3.3.1).

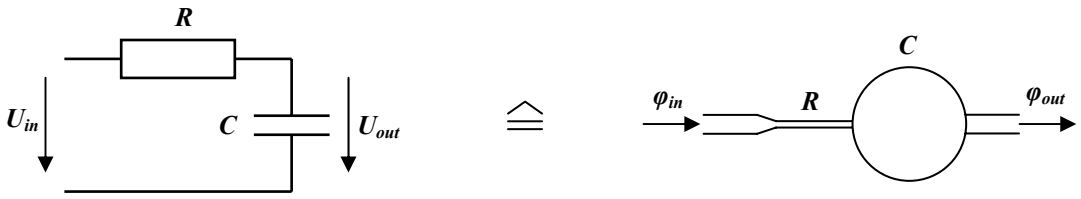

Figure 4.3.3.1: RC filter for the equalization of the diluted sample flow downstream the probe

Measurements at pilot and production reactors have revealed that a capillary tube with a length of 10cm and an inner radius of 0.5mm in connection with the volume of the instrumentation has been a good remedy to sufficiently block fluctuations of the pressure inside the reactors. The mean pressure difference over the capillary calculated with equation 4.3.2.1 for nitrogen is 3.63mbar. The effect of the capillary tube is illustrated in figure 4.3.3.2. However pressure fluctuations over a longer time period still can affect the measurements (chapter 5).

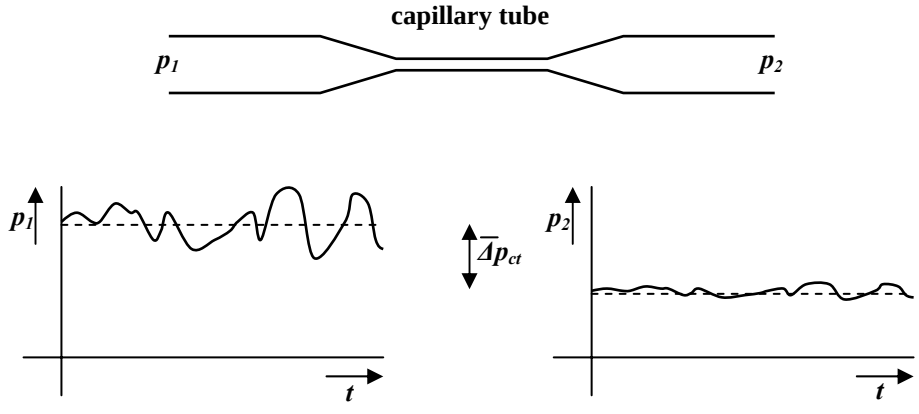

Figure 4.3.3.2: Effect of the capillary tube for the pressure equalization

The contribution of diffusional particle losses of the capillary tube is minor. For 10nm particles 94.7%, for 100nm particles 99.7% pass the capillary tube (p=1000mbar).

4.3.4 Balancing the volume flows

The balance of the flows under process conditions is checked by the following procedure (see functional scheme, appendix A1):

1. Clean gas and excess gas flows $\dot{V}_c$ and $\dot{V}_e$ are set to zero (valve 9 and 25 are closed) and the aerosol flow $\dot{V}_a$ is measured with the differential pressure gauge.

2. $\dot{V}_c$ and $\dot{V}_e$ are switched on, $\dot{V}_c$ is varied until the differential pressure gauge indicates the same value for $\dot{V}_a$ as in 1.

4.4 Charging process

4.4.1 Ultra violet irradiation unit

In order to imprint a known charge distribution on the particle collective, radioactive sources or corona discharger are not suitable because of the low pressures and the presence of corrosive gases in particle synthesis processes. So uv irradiation generated by a commercially available excimer radiator (Matter Engineering AG, Switzerland, type 990810) is favoured. Its principle is the excitation of encapsulated gas by a high frequency alternating electrical field. The decay of the gas ions into the ground state generates photons (Matter [48]). The frequency of the a.c. field determines the number of photons per time unit and thus the intensity of the emitted light. The wavelength of the emitted light is determined by the encapsulated gas. A KrCl type with a wavelength λ_P = 222nm (Φ_{photon} = 5.56eV) and a XeCl type with a wavelength λ_P = 172nm (Φ_{photon} = 7.18eV) are available. The KrCl respectively XeCl is separated from the process gas by a quartz glass tube, which is transparent for ultra violet light.

4.4.2 Numerical simulation of charging dynamics

For the determination of the charging of the particles entering the DMA, a mathematical model is necessary which describes the dynamics of thermionic, photonic charging and recombination. It predicts the effects of various conditions as to pressure, temperature, material, and concentration on the charging of the particle ensemble. The model consists of sets of combined differential equations as proposed in chapter 3.2. Each set describes a certain stage of the charging process. These sets of equations have to be solved sequentially for various conditions. The stages in the charging process are illustrated in figure 4.4.2.1.

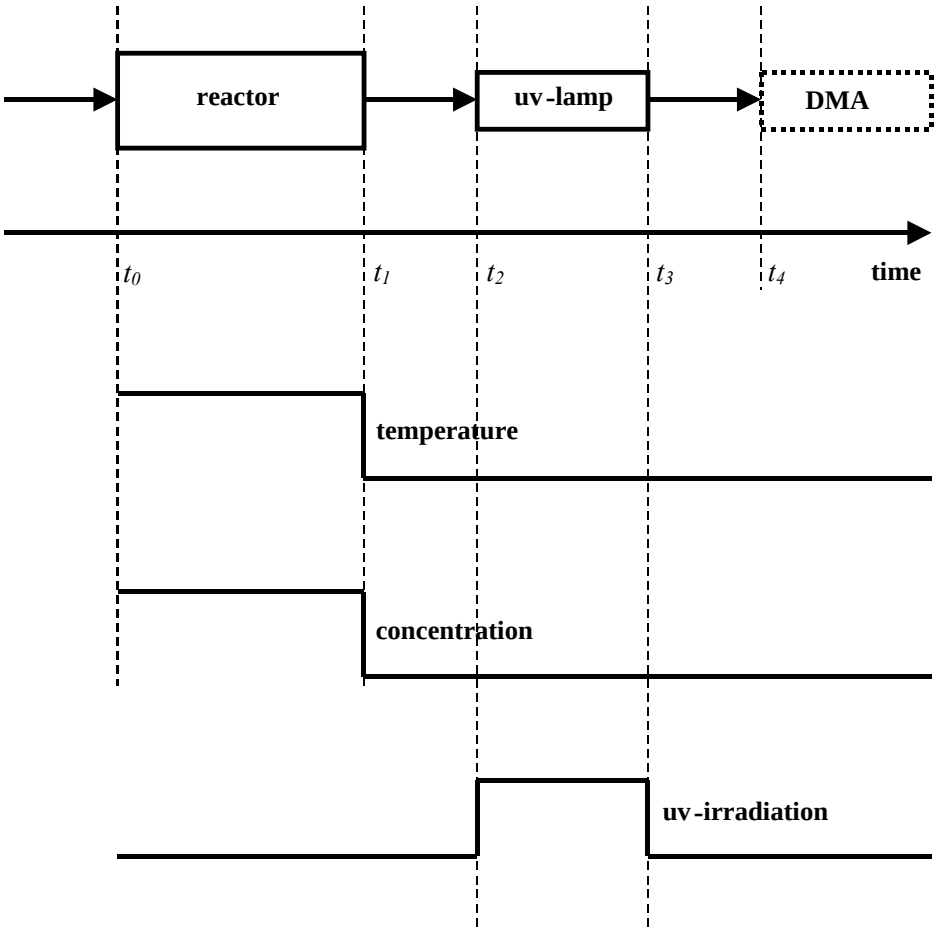

Figure 4.4.2.1: Stages of the charging process

The charging process involves thermionic charging inside the reactor, dilution, transport, and uv irradiation. It begins when particles appear in the reactor and is supposed to be finished when particles enter the DMA.

The process starts at $t = t_0$ with a certain particle number size distribution. The temperature inside the reactor is assumed to have a rectangular profile. Depending on the temperature particles acquire charge by thermionic electron emission. Particle generation dynamics (nucleation, condensation, etc.) are not considered. At $t = t_1$ a sudden dilution takes place causing reduction of temperature and concentration. At $t = t_2$ the particles enter the irradiated zone of the ultra violet irradiation unit. At $t = t_3$ the ultra violet irradiation unit is left and at $t = t_4 = t_{DMA}$ the DMA is entered. For $t_1 < t < t_2$ and $t_3 < t < t_4$ only relaxation caused by ion– particle recombination takes place. The pressures inside reactor, uv lamp, and DMA are equal. Since the LPDMPS is run with a fixed volume flow, t_1 to t_4 do not vary. When only one chemical compound is present the dynamic balances of concentrations and ions suggested by equations 3.2.2.1 and 3.2.2.2 need a classification as to particle size D_P and number of elementary charges q only. Then the aerosol can be represented by the two- dimensional matrix

$$\vec{\vec{N}} = \begin{pmatrix} N_{D_{P1},q_{\min}} & N_{D_{P1},q_{\min}+1} & \cdots & N_{D_{P1},q=0} & \cdots & N_{D_{P1},q_{\max}-1} & N_{D_{P1},q_{\max}} \\ N_{D_{P2},q_{\min}} & N_{D_{P2},q_{\min}+1} & \cdots & N_{D_{P2},q=0} & \cdots & N_{D_{P2},q_{\max}-1} & N_{D_{P2},q_{\max}} \\ N_{D_{P3},q_{\min}} & N_{D_{P3},q_{\min}+1} & \cdots & N_{D_{P3},q=0} & \cdots & N_{D_{P3},q_{\max}-1} & N_{D_{P3},q_{\max}} \\ . & & & & & & \\ . & & & & & & \\ N_{D_{P\max},q_{\min}} & N_{D_{P\max},q_{\min}+1} & \cdots & N_{D_{P\max},q=0} & \cdots & N_{D_{P\max},q_{\max}-1} & N_{D_{P\max},q_{\max}} \end{pmatrix}$$

(i ↓, k →)

where N_{D_{Pi},q_k} represents the number concentration for a size fraction D_{Pi} with q_k elementary charges. The total concentration $N = \sum_i \sum_k N_{D_{Pi},q_k}$. The charge fractions $f(D_{Pi},q_k)$ are determined by $f(D_{Pi},q_k) = \frac{N_{D_{Pi},q_k}}{\sum_k N_{D_{Pi},q_k}}$, where $\sum_k N_{D_{Pi},q_k}$ is the sum of concentrations of a certain size fraction D_{Pi} or the i^{th} line vector of $\vec{\vec{N}}$. The task of a numerical model is to calculate the concentration matrix $\vec{\vec{N}}(t)$ and the charge fractions $f(D_{Pi},q_k,t)$ for any time t, especially for $t = t_{\text{DMA}}$, when the aerosol enters the DMA. The lines

$$\begin{pmatrix} N_{D_{Pi},q_{\min}} & N_{D_{Pi},q_{\min}+1} & \cdots & N_{D_{Pi},q=0} & \cdots & N_{D_{Pi},q_{\max}-1} & N_{D_{Pi},q_{\max}} \end{pmatrix}$$

and the columns

$$\begin{pmatrix} N_{D_1,q_k} \\ N_{D_2,q_k} \\ N_{D_3,q_k} \\ . \\ . \\ N_{D_{\max},q_k} \end{pmatrix}$$

depend on each other by the balance of ions

$$\frac{\mathrm{d}n_{ions}}{\mathrm{d}t} = \sum_i \sum_k \left(\left(\alpha_{D_{Pi},q_k}^{q\to q+1} + \upsilon_{D_{Pi},q_k}^{q\to q+1} \right) \cdot N_{D_{Pi},q_k} - n_{ions} \cdot \beta_{D_{Pi},q_k}^{q\to q-1} \cdot N_{D_{Pi},q_k} \right) - \Delta_{ions}$$

and the balances of concentrations

$$\frac{\mathrm{d}N_{D_{Pi},q_k}}{\mathrm{d}t} = \left(\alpha_{D_{Pi},q-1}^{q\to q+1} + \upsilon_{D_{Pi},q-1}^{q\to q+1} \right) \cdot N_{D_{Pi},q-1} - \left(\alpha_{D_{Pi},q_k}^{q\to q+1} + \upsilon_{D_{Pi},q_k}^{q\to q+1} \right) \cdot N_{D_{Pi},q_k} + n_{ions} \cdot \left(\beta_{D_{Pi},q+1}^{q\to q-1} \cdot N_{D_{Pi},q+1} - \beta_{D_{Pi},q_k}^{q\to q-1} \cdot N_{D_{Pi},q_k} \right).$$

(See chapter 3.2) The ionization- and recombination coefficients depend on size and on charge, thus for each N_{D_{Pi},q_k} the corresponding $\alpha_{D_{Pi},q_k}^{q\to q+1}$, $\beta_{D_{Pi},q_k}^{q\to q-1}$, and $\upsilon_{D_{Pi},q_k}^{q\to q+1}$ have to be calculated as suggested in chapter 3.2. The different phases of ionization and relaxation is realized by setting $\alpha_{D_{Pi},q_k}^{q\to q+1}=0$ for times outside the uv lamp and by setting $\upsilon_{D_{Pi},q_k}^{q\to q+1}=0$ for times outside the reactor. Recombination always takes place so $\beta_{D_{Pi},q_k}^{q\to q-1}>0$ for any time *t*.

The necessary number of charge states depends on the particle size. For a particle size D_P = 10nm a minimum charge of $-3|e|$ and a maximum charge of $10|e|$ was found to be sufficient. For D_P = 100nm particles acquire more charge demanding more possible charge states $(-10\le q\le 100)$. The maximum and minimum numbers of elementary charges also depend on temperature, material, and gas pressure. If the numbers of charge states is chosen too high, $N_{D_{Pi},q\min}$ and $N_{D_{Pi},q\max}$ (and neighbouring) just remain zero. The only draw back of choosing too many possible charge states is a longer computational time. For 100 size fractions and $-10\le q\le 100=111$ possible charge states the number of combined differential equations is 11101.

The numerical calculation is performed by a Prince- Dormand 8th order Runge- Kutta method with adaptive step size control (Prince *et al.*, [60], Dormand *et al.*, [11]). Depending on particles size and concentrations on an Intel Pentium II machine the computational time for a set of 11101 differential equations is a few minutes $\left(D_P\approx 100\text{nm},\ N_{SP}\approx 10^8\,\text{cm}^{-3}\right)$.

4.4.3 Simulations of charging dynamics for various synthesis process conditions

The model presented in chapter 4.4.2 will be used to quantify the effects of pressure and concentration on the charging. It will be used to investigate on the influences of (pre-) charging by thermionic ionization, the polarity of the DMA voltage, and excimer wavelength. Although the particles are already charged when they leave the reactor, it is desirable to achieve charge distributions which are independent from thermionic charging because the influence of the conditions inside the reactor is difficult to estimate and because the effective Richardson constant R^* depends on material, temperature, and morphology (Sze, [69]). The rate of thermionic ionization furthermore is sensitive to changes of the temperature since it is proportional to T^2 (chapter 3.2.3). Also the dielectric constant strongly increases for T > 600K (Sze, [69]) and the time-temperature profile is far from a rectangular shape but depends on the actual trajectory through the reactor. The calculations follow the course illustrated in figure 4.4.2.1. Table 4.4.3.1 lists the parameters which have been used in the calculations.

For the product of $K_C \cdot I$ (equation 3.2.2.3) the empirical value of $1.76 \cdot 10^{35}\,J^{-1}m^{-2}s^{-1}$ is used (Maisels *et al.* [47]). This value has been found originally for lead sulphide. Since a variation in the order of 10^2 has shown little influence (Maisels *et al.* [47), it is used for SiO_2 also. The total number concentrations N up- and downstream of the sampling probe are indicated N_{process} and N_{SP} while the dilution ratio D_{SP} equals $D_{SP} = \frac{N_{process}}{N_{SP}}$.

Table 4.4.3.1: Parameters used in the calculations of charge distributions

parameter	**symbol**	**values**	**unit**
work function of SiO_2	ϕ_{∞,SiO_2}	5.0	eV
photon energy	ϕ_{photon}	5.56, 7.18	eV
temperature inside the reactor	T_R	1400	°C
temperature after sampling	T_S	20	°C
time of leaving the reactor	t_1	0.3	s
time of beginning of uv irradiation	t_2	21.9	s
time of end of uv irradiation	t_3	26.5	s
time of entering the DMA	t_4	34.6	s
concentration inside the process	N_{process}	10^4 to 10^8	cm^{-3}
dilution ratio	D_{SP}	120	1
pressure	p	200 to 1000	mbar
geometric standard deviation of D_P	σ_g	1.0, 1.4, 1.5, 2.0	1
mean particle size D_{P0}	D_{P0}	10 to 100	nm
effective Richardson constant	R^*	$0.01R_{theor}$ to $100R_{theor}$	$Am^{-2}K^{-2}$
relative dielectric constant	ε_{r,SiO_2}	3.9 [1)]	1

[1)] amorphous SiO_2 (Sze, [69])

The effective Richardson constant R^* is difficult to determine because apart from the effective electron mass m_{e0}, R^* also is influenced by the morphology and several physical effects (Lindsay *et al.* [43]). Deviations in the order of 10 are typical (Lindsay *et al.* [43]). A variation of R^* in the range of $0.01R_{theor}$ to $100R_{theor}$ therefore covers a variety of materials.

Figures 4.4.3.1 to 4.4.3.6 show results of calculations of the time dependent charging of monodisperse SiO_2 particles. Figures 4.4.3.1 and 4.4.3.2 give the charge distribution in terms of the arithmetic mean number of

elementary charges $q_0 = \frac{\sum_k N_{D_{Pi},k} \cdot q_k}{\sum_k N_{D_{Pi},k}}$ and the standard deviation $\sigma_q = \sqrt{\frac{\sum_k N_{D_{Pi},k} \cdot (q_k - q_0)}{\sum_k N_{D_{Pi},k} - 1}}$, figures 4.4.3.3 to 4.4.3.6 show the fractions $f(-2)$, $f(-1)$, $f(1)$, and $f(2)$ as a function of time. The curves for R_{theor} are solid to point out that the lines coincide after uv irradiation.

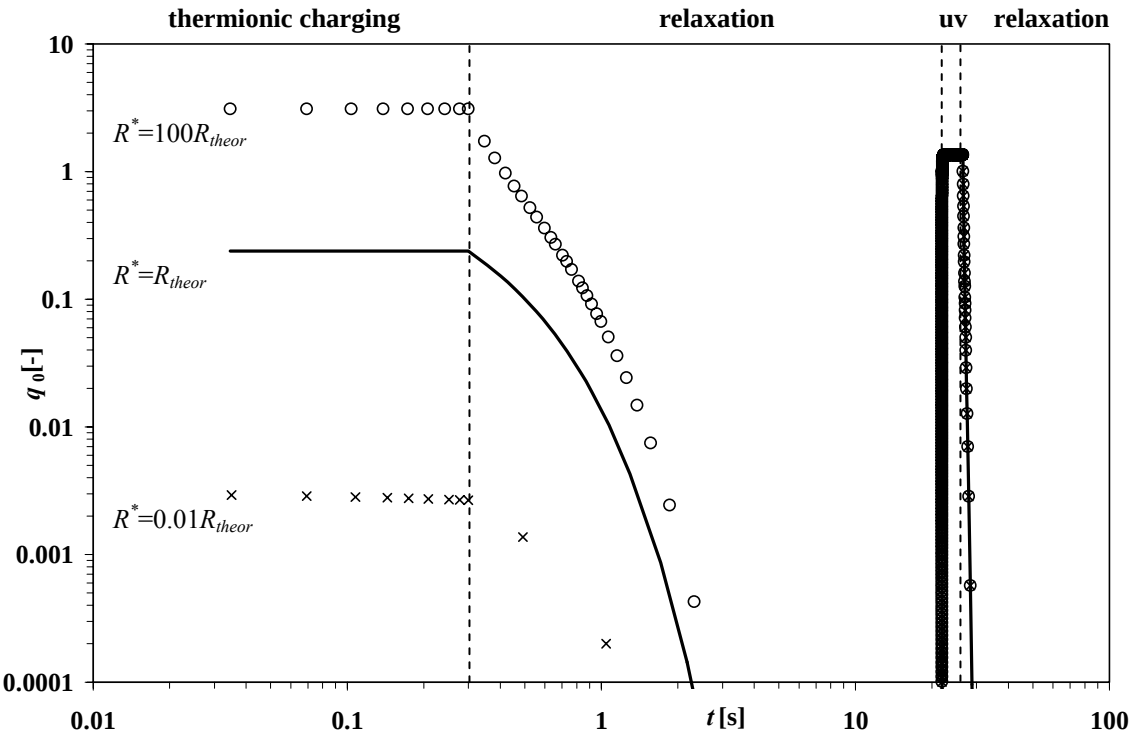

Figure 4.4.3.1: q_0 as a function of time for monodisperse SiO_2 particles calculated for various effective Richardson constants R^* (D_P = 100nm, N_{SP} = 10^6cm^{-3}, λ_P = 222nm, p = 600mbar, T_R = 1400°C)

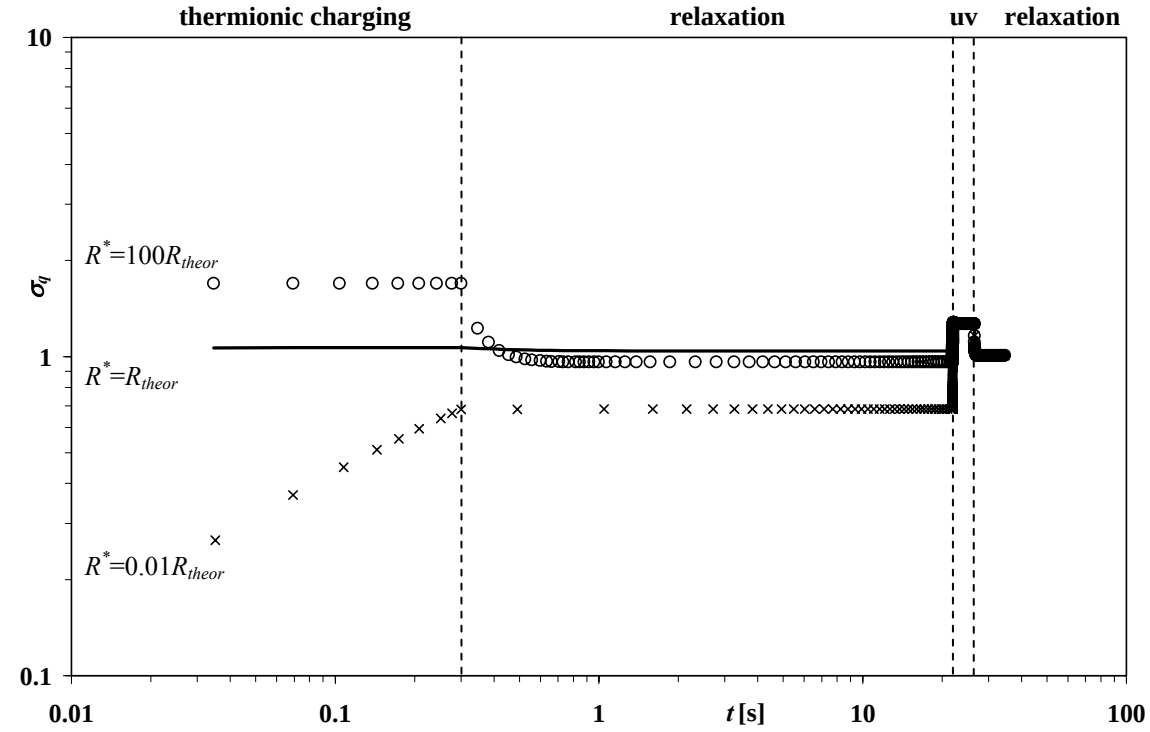

Figure 4.4.3.2: σ_q as a function of time for monodisperse SiO_2 particles calculated for various effective Richardson constants R^* (conditions as for figure 4.4.3.1)

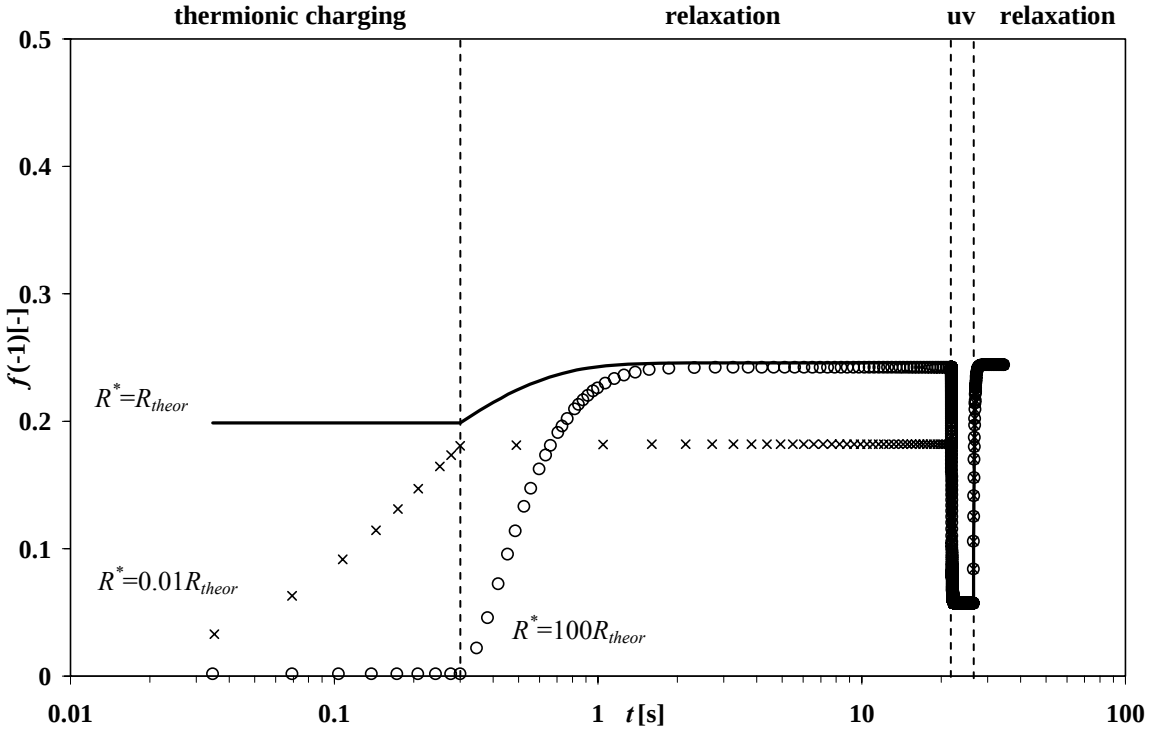

Figure 4.4.3.3: $f(-1)$ as a function of time for monodisperse SiO_2 particles calculated for various effective Richardson constants R^* (conditions as for figure 4.4.3.1)

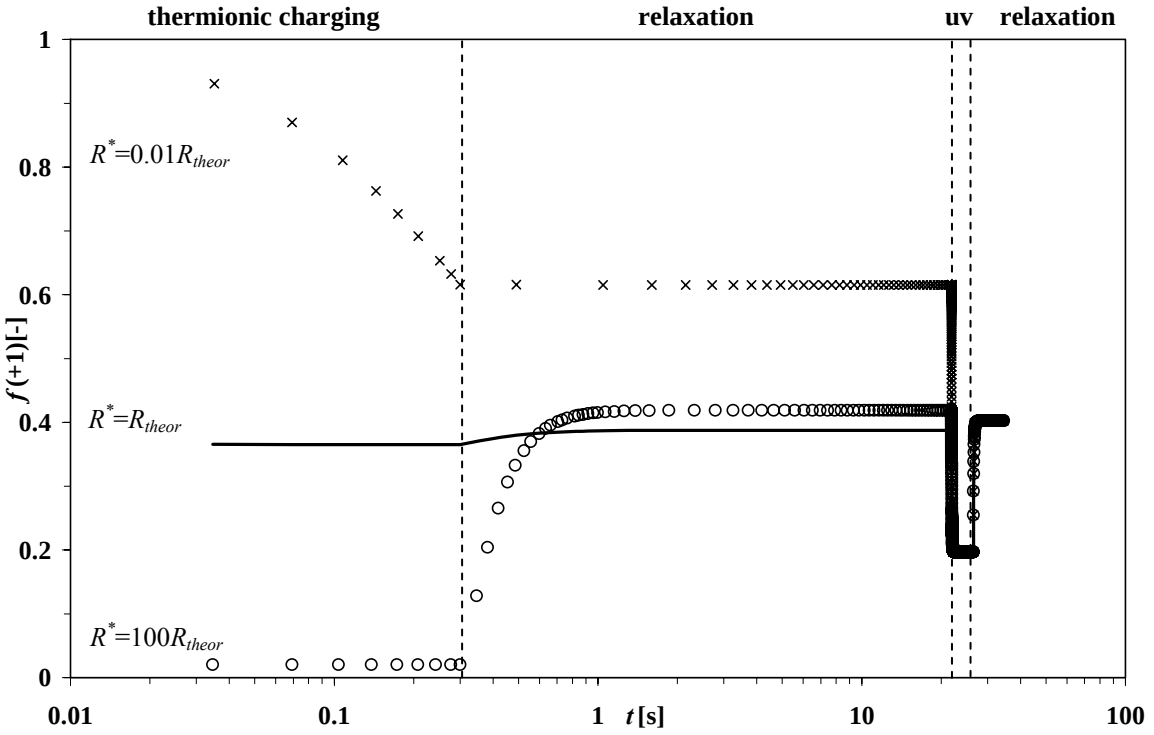

Figure 4.4.3.4: *f*(+1) as a function of time for monodisperse SiO_2 particles calculated for various effective Richardson constants R^* (conditions as for figure 4.4.3.1)

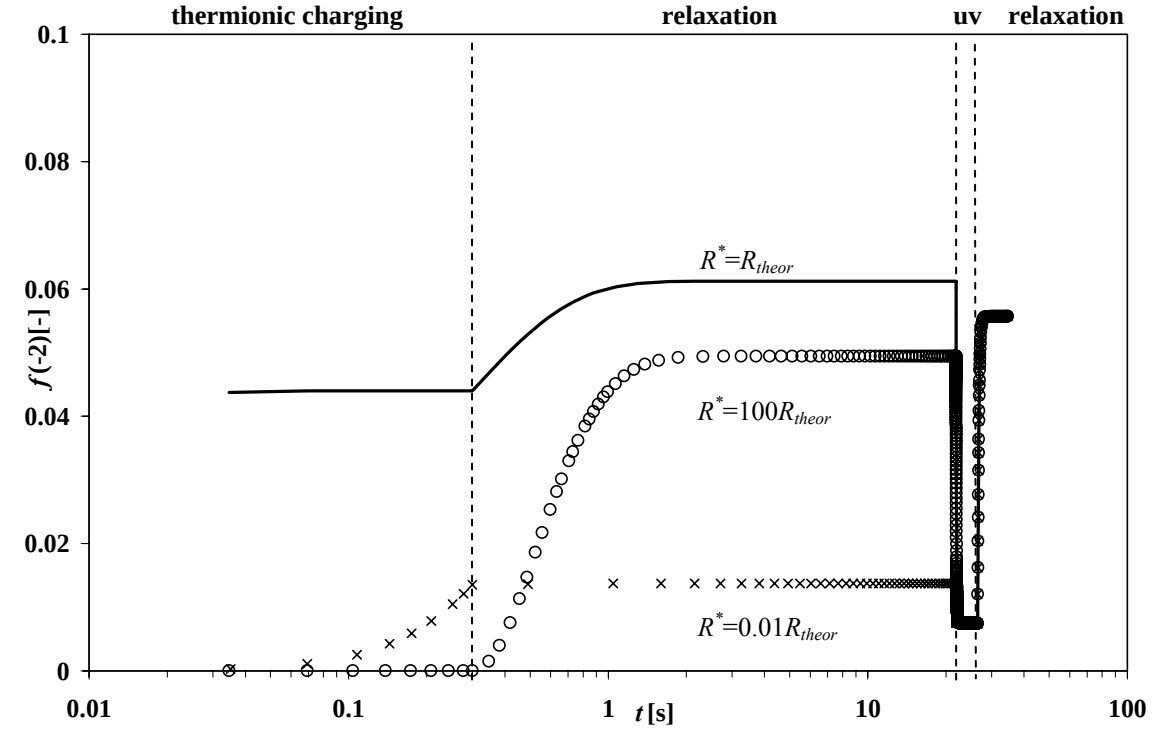

Figure 4.4.3.5: *f*(-2) as a function of time for monodisperse SiO_2 particles calculated for various effective Richardson constants R^* (conditions as for figure 4.4.3.1)

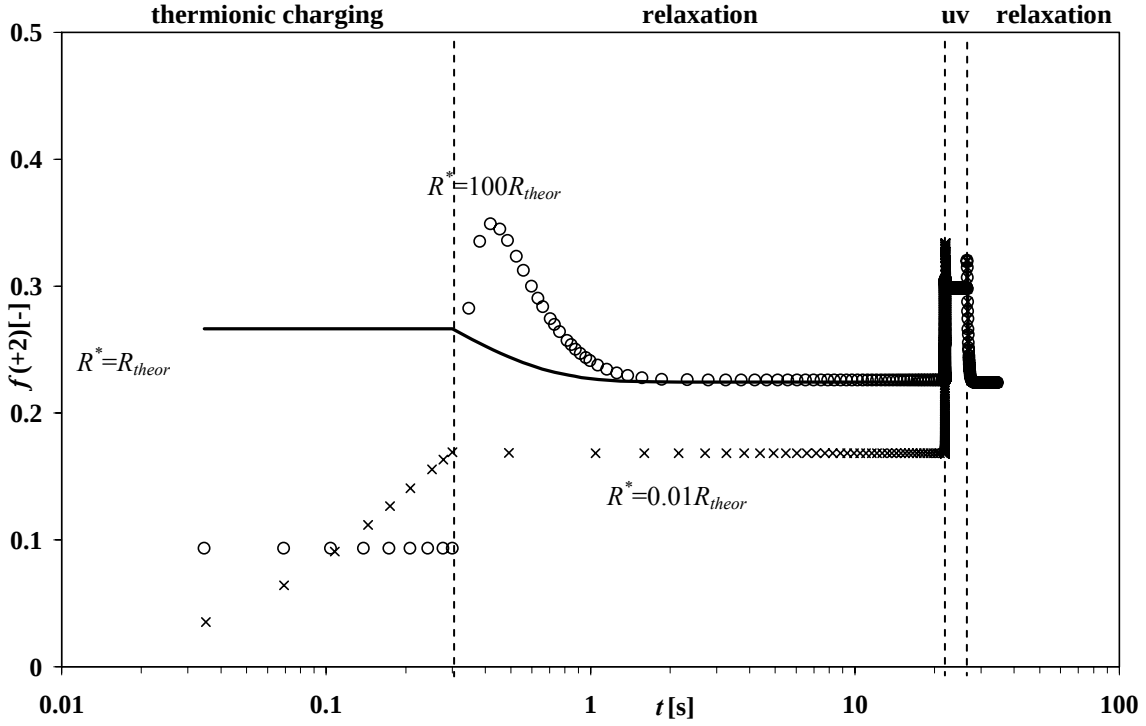

Figure 4.4.3.6: *f*(+2) as a function of time for monodisperse SiO_2 particles calculated for various effective Richardson constants R^* (conditions as for figure 4.4.3.1)

The results in figures 4.4.3.1 to 4.4.3.6 show that the uv excimer with λ_P = 222nm can equalize the effects of thermionic charging and to make the charging of particles independent from its charging history due to the fact that uv photonic charging is much more efficient than thermionic charging. Neither various Richardson constants nor reactor temperature (<2000K) does influence the charging downstream the uv lamp provided that an equalization of ionization and recombination has taken place.

A KrCl excimer with λ_P = 222nm has turned out to generate a charge distribution which in general has a smaller σ_q as the one generated with a XeCl type (λ_P = 172nm). In order to minimize the influence of multiply charged particles in the data inversion this is an advantage (chapter 4.7).

The data inversion algorithm is most sensitive against errors due to correction for multiple charges, when $f(q)\big|_{|q|=1}$ is low and the fractions $f(q)\big|_{|q|\geq 2}$ are comparatively high because the share of singly charged particles is used as an initial guess for the data inversion. Therefore it is desirable that $f(q)\big|_{|q|\geq 2}$ is small, especially since for the particle detection an electrometer is used and the multiply charged particles are weighted by their number of elementary charges and it. It turned out that for negatively charged particles

$\frac{f(q)}{f(-1)}$ in general is smaller than for positively charged ones $\frac{f(q)}{f(1)}$ therefore the more suitable DMA voltage is positive.

In table 4.4.3.2 the fractions $|q \cdot f(q)|$ of multiply charged particles are given in relation to the fraction $f(-1)$ for size distributions with different mean sizes. As a comparison in table 4.4.3.3 the values for bipolar diffusion charging (Wiedensohler [80]) are given. In contrast to bipolar diffusion charging for uv irradiation the fraction $f(D_P, q)$ for a certain D_P depends on the size distribution and on concentration. Particles with a diameter of 20nm for example will have different charge depending on whether they belong to a size distribution with a mean size of 10nm, 20nm, or 50nm. This is a challenging task for the data inversion and demands a new approach in the calculation of size distributions. The simulations reveal that for a certain particle size not only the fraction of singly charged particles rises with rising mean size, but also the relative shares $\frac{f(q)}{f(-1)}$ of multiply charged ones increase. Compared to the charged fractions for bipolar diffusion charging as calculated after Wiedensohler [80] the values are in the same order of magnitude. For the correction regarding multiple charges however, particles will be from upper size channels and charge probabilities higher than those coming with bipolar diffusion charging are to be expected.

Table 4.4.3.2: $f(-1)$ and $\frac{|q \cdot f(q)|}{f(-1)}$ for σ_g = 2.0, SiO_2, N_{SP} = $10^6 cm^{-3}$, 293.15K, 1013mbar, numerical simulation

D_P [nm]	D_{P0} [nm]	$f(-1)$ [%]	$2 \cdot f(-2)/f(-1)$ [%]	$3 \cdot f(-3)/f(-1)$ [%]	$4 \cdot f(-4)/f(-1)$ [%]
20	10	9.32	0.18	0	0
20	20	17.8	0.14	0	0
20	50	34.9	0.33	0	0
50	20	14.1	1.35	0.015	0
50	50	29.1	18.8	0.37	0
50	100	44.6	33.8	1.12	0.003
100	50	16.6	18.6	3.87	0.13
100	100	31.8	66.4	11.4	0.67
100	200	37.6	88.9	22.1	1.82

Table 4.4.3.3: $f(-1)$ and $\frac{|q \cdot f(q)|}{f(-1)}$ for bipolar diffusion charging, 293.15K, 1013mbar (Wiedensohler [80])

D_P [nm]	$f(-1)$ [%]	$2 \cdot f(-2) / f(-1)$ [%]	$3 \cdot f(-3) / f(-1)$ [%]	$4 \cdot f(-4) / f(-1)$ [%]	$5 \cdot f(-5) / f(-1)$ [%]	$6 \cdot f(-6) / f(-1)$ [%]	$7 \cdot f(-7) / f(-1)$ [%]
10	5.14	0.0	0.0	0.0	0.0	0.0	0.0
20	11.0	0.36	0.0	0.0	0.0	0.0	0.0
50	22.3	10.2	0.0	0.0	0.0	0.0	0.0
100	27.9	40.17	39.74	0.14	0.0	0.0	0.0
350	21.5	138.9	106.5	51.9	17.2	3.91	0.65

For increasing particle size the charging probabilities increase because of the greater particle surface area. For photo charging the mean charge increases since ionization depends stronger on the surface area than recombination (chapter 3.2). Figure 4.4.3.7 gives the mean number of elementary charges $q_0(t)$ for monodisperse SiO_2 particles with various sizes. Only photo charging and relaxation are focussed ($t > t_3$) since the thermionic charging is erased.

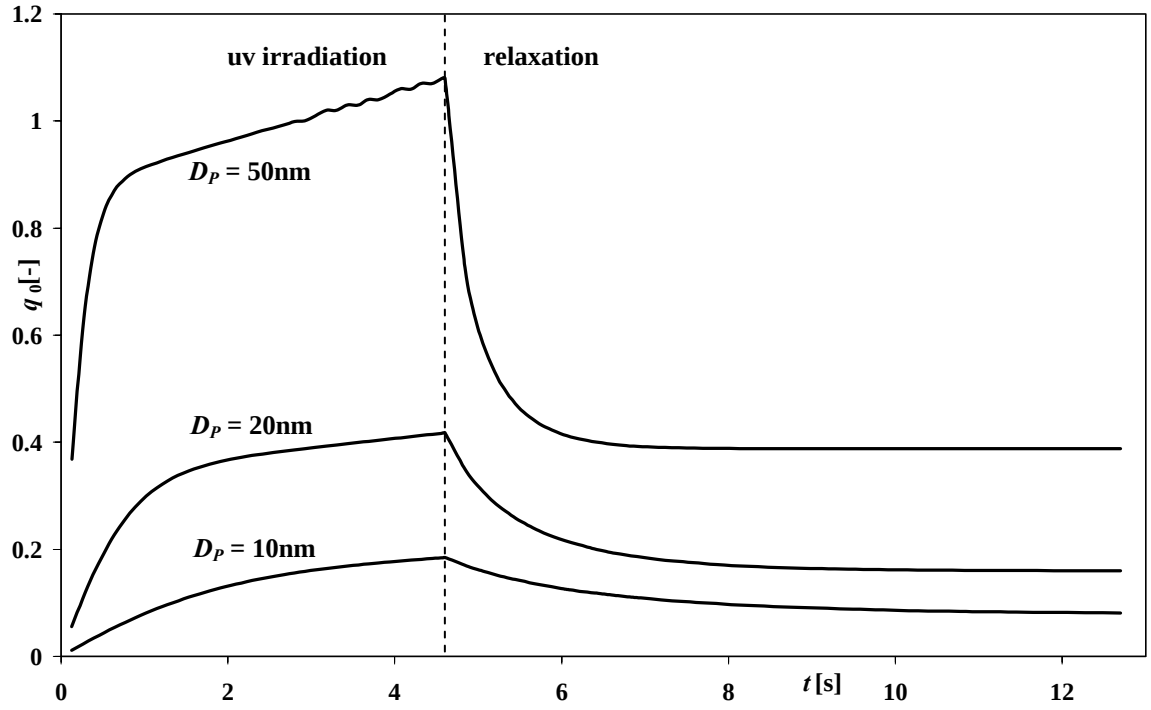

Figure 4.4.3.7: mean number of elementary charges q_0 as a function of t-t_3 (monodisperse SiO_2, N_{SP} = $10^6 cm^{-3}$, p = 1013mbar) for various D_P for the phase of uv irradiation and subsequent relaxation

A dependency of the charging on pressure is expected because the ionization and recombination coefficients $\alpha_{q,R_P,C_m}^{q\to q+1}$ $\beta_{q,R_P,C_m}^{q\to q-1}$ $\upsilon_{q,R_P,C_m}^{q\to q+1}$ depend on the pressure. A variation of the pressure in the calculation shows that the influence is small (see figure 4.4.3.8).

Since high particle concentration reduces ion losses to the walls and increases the recombination rate, for higher concentrations lower numbers of positive elementary charge are expected. In figure 4.4.3.9 $q_0(t)$ is shown as calculated for the concentrations $N_{SP} = 10^4 cm^{-3}$, $N_{SP} = 10^6 cm^{-3}$, and $N_{SP} = 10^8 cm^{-3}$. For $N_{SP} = 10^8 cm^{-3}$ the resulting charge distribution is close to zero (in agreement to Maisels *et al.* [47]).

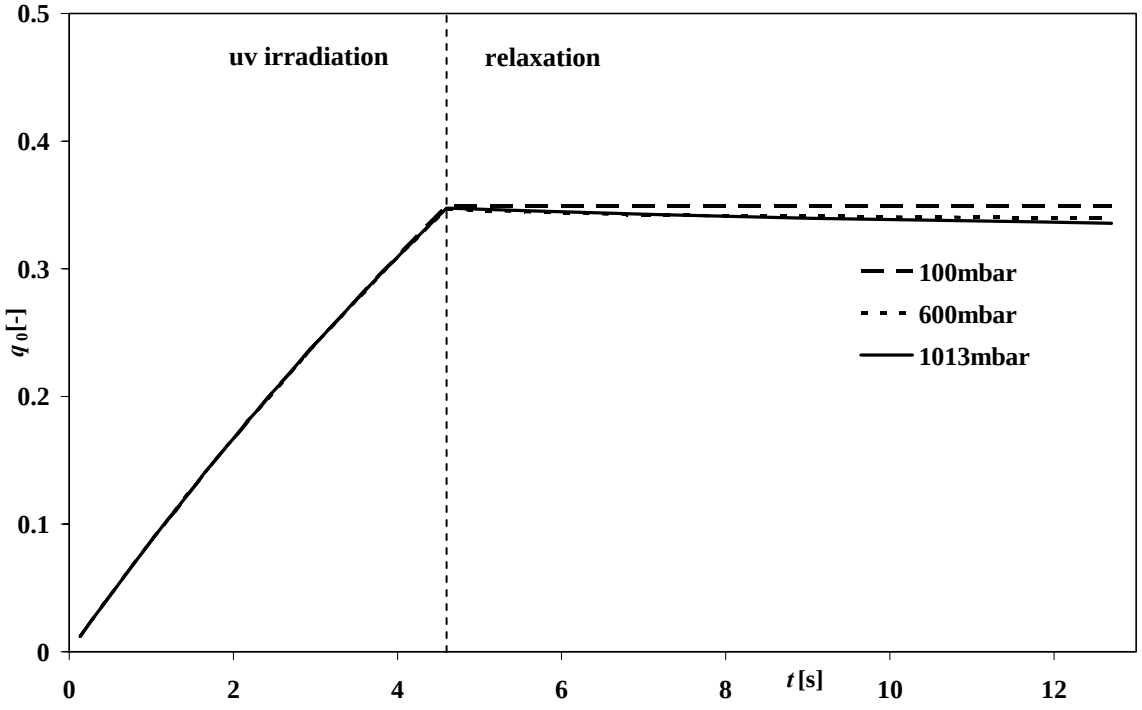

Figure 4.4.3.8: mean number of elementary charges q_0 as a function of t (monodisperse SiO_2, D_P = 10nm, $N_{SP} = 10^4 cm^{-3}$) for various p for the phase of uv irradiation and subsequent relaxation

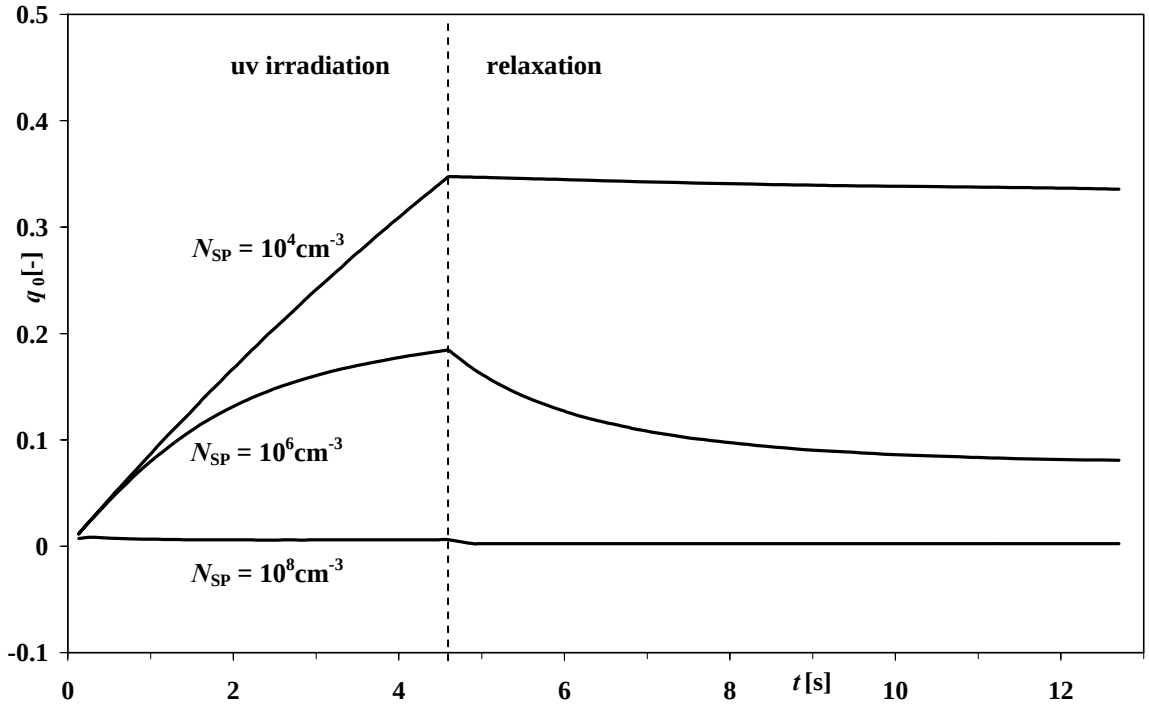

Figure 4.4.3.9: mean number of elementary charges q_0 as a function of t (monodisperse SiO_2, D_P = 10nm, p = 1013mbar) for various concentrations N_{SP} for the phase of uv irradiation and subsequent relaxation

As a conclusion of the investigations it can be stated that uv irradiation with a wavelength of 222nm is an appropriate method to charge particles for DMPS applications under conditions prevailing at the synthesis processes discussed in chapter 2. Variations of parameters (e.g. material, concentration, pressure, particle size distribution) lead to changes of the resulting charging. Nonetheless the model is able to predict particle charging by uv irradiation by taking the said quantities into account. It has to be realized that the data inversion is complicated since the charging depends on the number size distribution.

4.5 DMA

4.5.1 DMA Design

As mentioned in chapter 3.5 two different types of DMA are usually applied for the mobility fractionation of charged particles: the radial flow DMA (RDMA) and the cylindrical flow DMA (CDMA). For the application in the LPDMPS a RDMA is favoured because it can be manufactured out of HCl resistant Hastelloy C4 standard vacuum pipe- and flange components. This means a decisive reduction of crafting- and financial expenses.

The decisive quantities of RDMA geometry are the radii R_2 and R_1 of in- and outlet slits and the distance b between the electrodes. These quantities determine the particle size range the DMA can be used for.

The upper size limit is given by the breakthrough voltage, the lower size limit by the magnitude of the influence of diffusion. The size range depends on the volume flows. DMA resolution decreases gravely for $Pe < 10^4$ (chapter 3.4). In order to achieve high Peclet numbers high volume flows, a high voltage and a short travel distance are beneficial. A maximum Peclet number implies an optimum relation $\frac{b}{R_2 - R_1} = 1$ of the axial distance b between the DMA electrodes and the radial distance $R_2 - R_1$ between inlet and outlet (Rosell- Llompart *et al.* [61]). This demand is limited by the DMA voltage and by the gas flows. Additionally a large distance b would gravely increase weight and size of the DMA.

For the new LPDMPS the gas volume flows are not to be varied since otherwise the critical orifices would have to be exchanged. The gas volume flows have to be small enough to fractionate particles as large as about 500nm, also the consumption of nitrogen is to be kept in limits. Therefore gas flows of $\dot{V}_a = \dot{V}_s =$ 0.3lmin^{-1} and $\dot{V}_c = \dot{V}_e =$ 3.0lmin^{-1} corresponding to $\beta_{Z_P,\text{ideal}} = 0.1$ were initially chosen. These volume flows are typical for aerosol sizing instrumentation. The radius R_2 of the circular inlet slit is 66.5mm, the one of the outlet drilling R_1 2mm. The axial distance b between the electrodes is 15mm leading to $\frac{b}{R_2 - R_1} = 0.233$. These dimensions lead to reasonable β_{Z_P} as calculated with equation 3.4.1.1.4.4 for various pressures. The values for β_{Z_P} are given in figure 4.5.1.1. The maximum Reynolds number $\text{Re}_{\max} = \frac{D_h \cdot v_{\max} \cdot \rho_{\text{gas}}}{\eta}$ with the hydraulic diameter $D_h = 2b$ and the maximum velocity $v_{\max} = \frac{\dot{V}}{2 \cdot \pi \cdot R_1 \cdot b}$ for $\dot{V} = 3.0\text{l}\,\text{min}^{-1}$ equals $\text{Re}_{\max} = 670.7$ so no turbulent gas flow is expected ($\rho_{\text{gas}} = 1.25\text{kgm}^{-3}$, $\eta = 17.8 \cdot 10^{-6}\,Pas$).

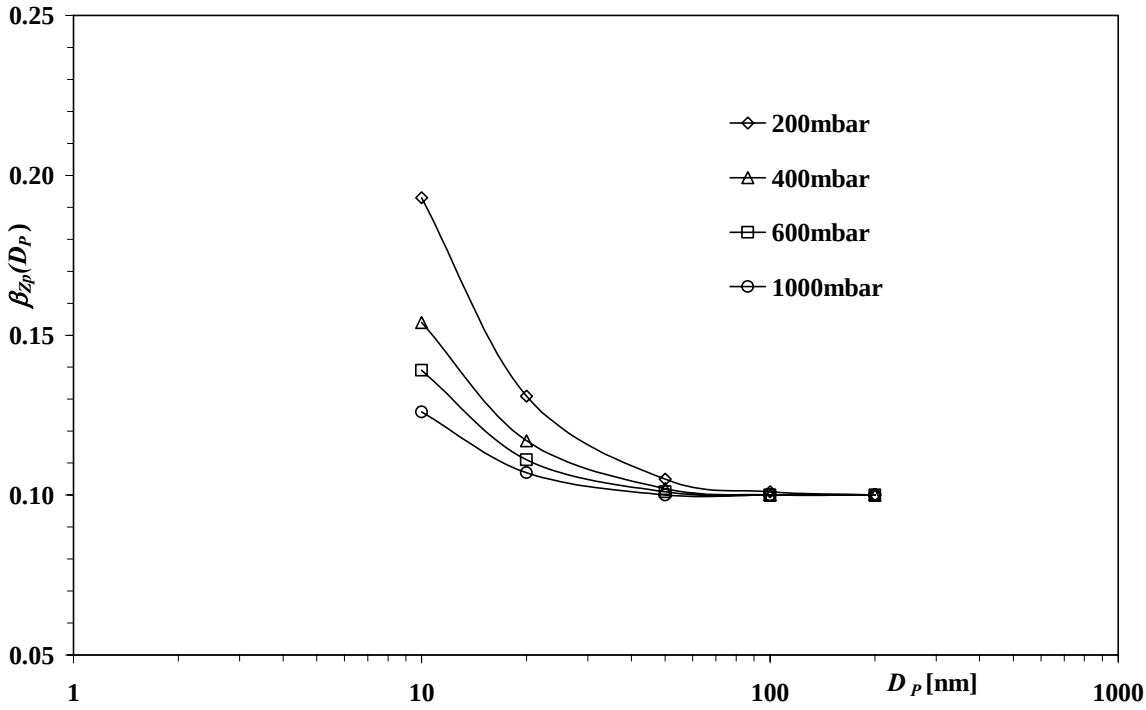

Figure 4.5.1.1: β_{Zp} as a function of D_P for the new DMA calculated with equation 3.4.1.1.4.4 for various pressures

A voltage of 20kV can be handled without too much equipment and precautions with respect to safety, isolation, cable, and electrical breakthrough. Theoretically the breakthrough voltage should be 45kV (chapter 3.4.1.2). In experiments in the laboratory electrical breakthroughs inside the new LPDMA under atmospheric pressure occurred at about 17kV. For $\dot{V}_c = 3.0\text{lmin}^{-1}$ this corresponds to a maximum particle size of 417nm (nitrogen, p=1013mbar).

The design of the new LPDMA shows modifications compared to already existing RDMA as to the aerosol, the clean and excess gas lines. In summary the innovations of the new LPDMA are:

1. Usage of Hastelloy C4 standard components.

2. The new LPDMA has four radially distributed clean gas inlet connections in order to supply a homogeneous clean gas flow.

3. The path which leads the aerosol to the DMA fractionation zone of the DMA is (nearly) rotationally symmetric in order to provide homogeneous flow. Existing RDMA in contrast only have a pipe which leads the aerosol into the fractionating zone thus generating a azimuthal flow component of the aerosol.

For details of the geometry see appendix A3.

4.5.2 Experimental determination of the DMA transfer function

The purpose of the new LPDMPS is the measurement of particle number size distributions. Particle number size distributions relate particle numbers to particle size intervals. The charge number concentration indicated by the electrometer has to be corrected for particle losses in the DMA which are mainly caused by diffusion. The particle size interval the indicated particle number has to be related to, depends on the DMA. Both quantities, the losses within the DMA and the particle size interval are implied by the transfer function of the DMA (chapter 3.1.3). Since the transfer function is gravely affected by diffusion, it depends on the particle size and on the pressure. The transfer function of the new LPDMA has been experimentally determined with the method proposed by Stratmann [68] (chapter 3.1.3) with a modified setup in order to apply various pressures. The modified setup is illustrated in figure 4.5.2.1.

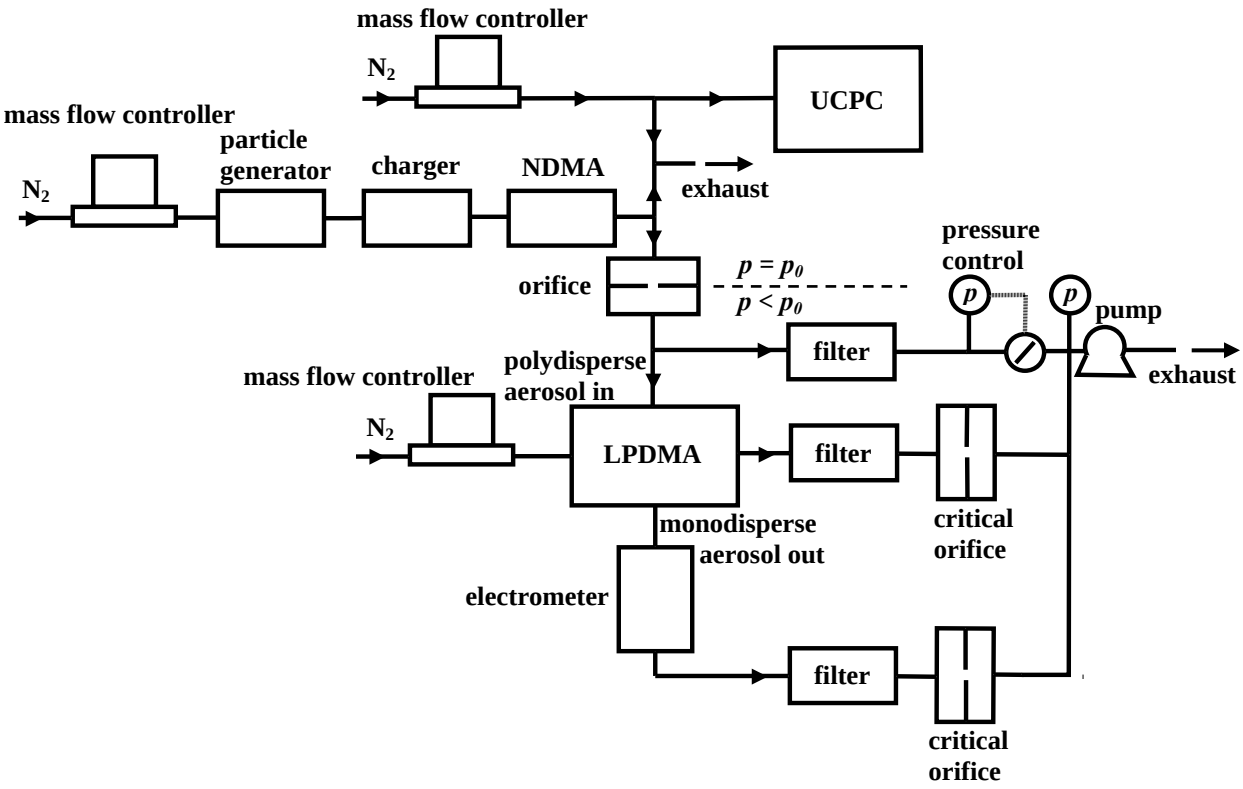

Figure 4.5.2.1: Experimental setup for the determination of DMA transfer functions for various pressures

The aerosol is generated by an evaporation- condensation process described by Scheibel *et al*. [63]. The generator consists of a tube furnace which contains NaCl or Ag. The material is evaporated at temperatures between 750°C and 1050°C. The furnace is flushed with nitrogen. Downstream the furnace the nitrogen vapour mixture is diluted and cooled with nitrogen which causes the vapour to condense and form lognormally size- distributed solid particles. Depending on the temperature and the material, the mean

particle size ranges from below 10nm to about 100nm. A TSI nano DMA type 3085 (NDMA) is used to cut a well defined narrow fraction out of the lognormal particle size distribution of the generator under atmospheric pressure. The transfer function of the NDMA is known (Hummes *et al.* [27]). The particle number concentration is measured by a TSI UCPC type 9025A under atmospheric pressure. The UCPC can handle a maximum concentration of $10^5 \mathrm{cm}^{-3}$. The aerosol sampled by the UCPC is diluted by nitrogen controlled by a mass flow controller. The transition into low pressure is realized by an orifice in connection with a pressure- controlled valve and a vacuum pump. The concentration of the aerosol drops with falling pressure since the gas volume increases but the particle number remains constant. Since the UCPC runs under atmospheric pressure only, the particle counting downstream the DMA under test had to be realized by an electrometer. Actually it is the one developed for the new LPDMPS. The performance of the electrometer will be described in chapter 4.6.

Because the concentration of particles drops by the transition to low pressure, upstream of the orifice it has to be comparatively high, especially because of the application of an electrometer as particle counter which has a low detection limit compared to the UCPC. The LPDMA clean gas flow is controlled by a mass flow controller, the DMA excess gas flow and the LPDMA sample gas flow are controlled by critical orifices described in chapter 4.3.1. The aerosol flow through the NDMA has been 1.5l/min as well as the flow through the UCPC. The clean gas flow through the NDMA has been 15l/min. For these flows, the transfer function of the NDMA has been presented by Hummes *et al.* [27].

The voltage of the LPDMA is slowly swept over a small range around the voltage corresponding to the mean particle size of the test aerosol upstream of the NDMA. The voltage ramp consists of 300 points. After having recorded the LPDMA voltage and the corresponding electrometer response, the electrometer signal is low pass filtered (figure 4.5.2.2) and converted into a normalized concentration as a function of the normalized mobility $\frac{N(Z_P)}{N(Z_P^*)}$, where $N(Z_P^*)$ is the concentration at the midpoint mobility Z_P^*. Low pass filtering is necessary for an unambiguous assignment of the concentration maximum to a DMA voltage respectively particle mobility. The calculation of the transfer function out of the low pass filtered, normalized electrometer signal is executed as proposed by Stratmann *et al.* [68] (chapter 3.1.3).

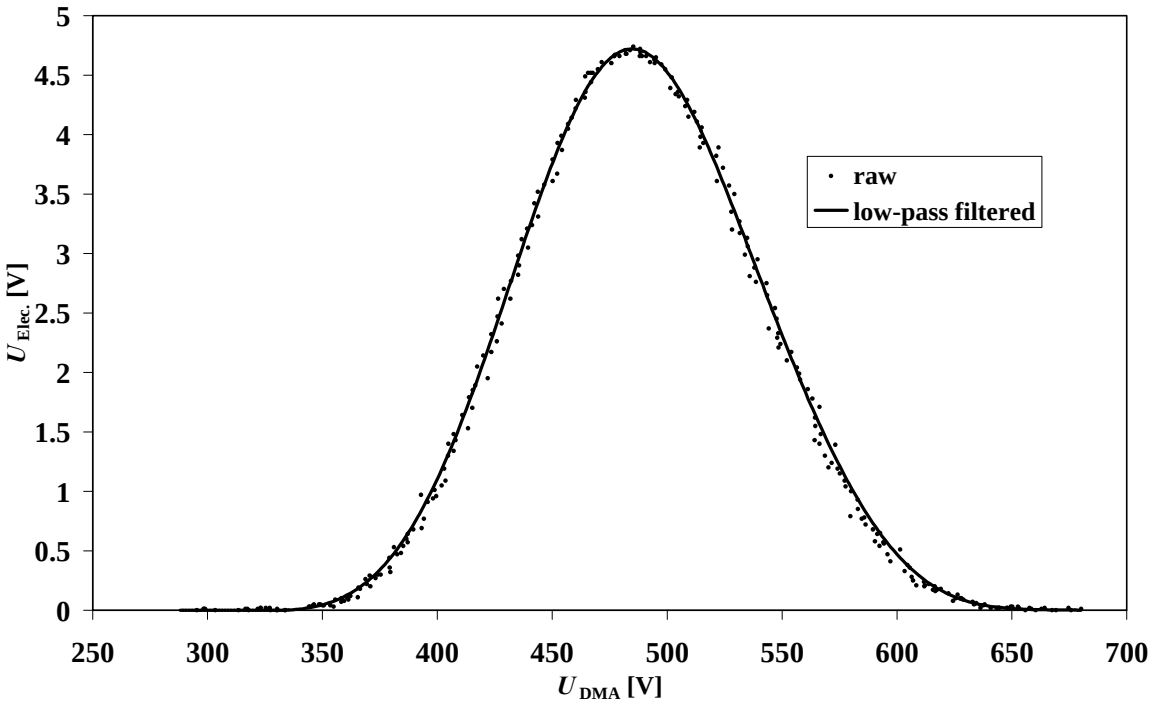

Figure 4.5.2.2: Example for raw signal (dots) and low-pass filtered signal (solid line) of the electrometer as a function of DMA voltage. The data are obtained with the setup shown in figure 4.5.2.1 with two DMA in series. The voltage of the first DMA is kept constant, the one of the second swept over the range 250V to 700V.

4.5.3 Experimental results for the DMA transfer function

The transfer function has been determined for various pressures and particle sizes. The volume flows of the LPDMA are those specified in chapter 4.3. Each measurement has been performed three times, the values for $\alpha_{Z_P}(D_P)$ and $\beta_{Z_P}(D_P)$ have been averaged. The averaged values for $\alpha_{Z_P}(D_P)$ and $\beta_{Z_P}(D_P)$ have been fitted (least squares method) by the functions

$$\alpha_{Z_P}(D_P) = C_1 + C_2 \cdot \exp\left(-\frac{D_P[\text{nm}] + C_3}{C_4}\right) \quad \text{and} \quad \beta_{Z_P}(D_P) = C_5 + C_6 \cdot \exp\left(-\frac{D_P[\text{nm}] + C_7}{C_8}\right) \qquad (4.5.3.1)$$

since a continuous function of D_P is desired. As an example figure 4.5.3.1 shows the averaged values for $\alpha_{Z_P}(D_P)$ and $\beta_{Z_P}(D_P)$ for a pressure of 200mbar. The bars indicate the deviations of the single measurement from the mean value. The dotted lines give the results for the exponential fits. The results for the pressures 400mbar, 600mbar, and 1000 mbar and the corresponding values for C_1 to C_8 are given in A9.

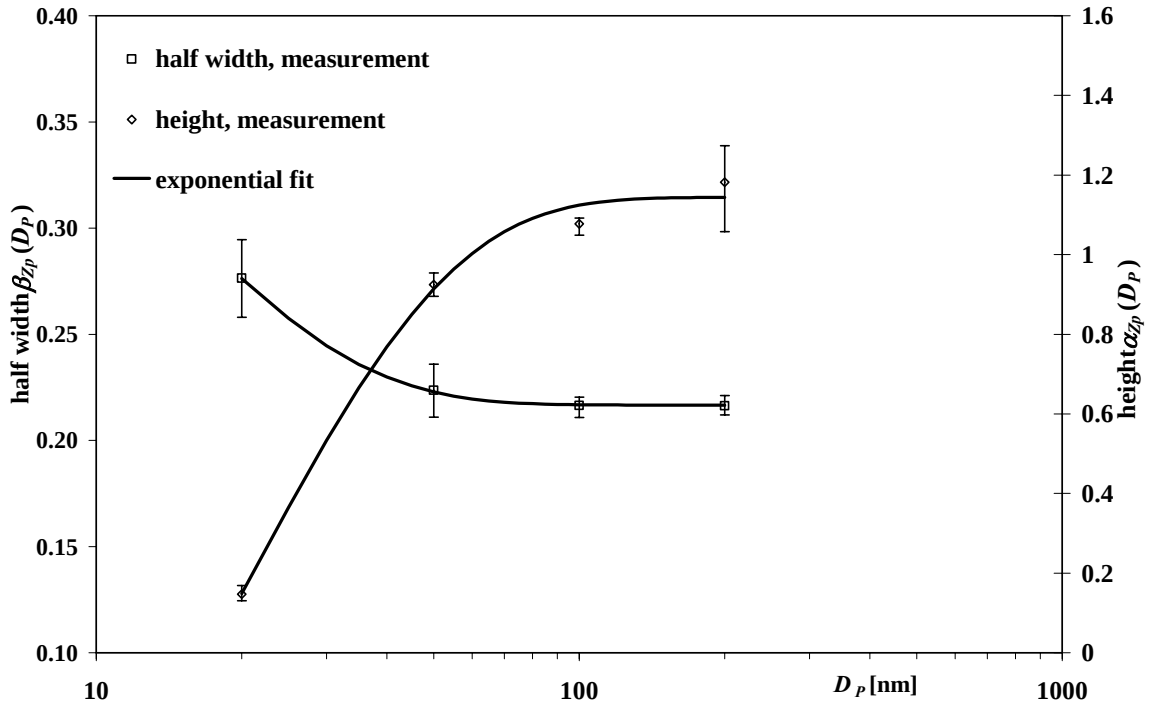

Figure 4.5.3.1: α_{Zp} and β_{Zp} as a function of D_P for p = 200mbar. The bars indicate the deviations of the single measurements from the mean value. The solid lines give the results for the exponential fits.

The averaged values for $\alpha_{Z_P}(D_P)$ and $\beta_{Z_P}(D_P)$ of the transfer functions are given by figures 4.5.3.2 and 4.5.3.3. The experimentally determined values for $\alpha_{Z_P}(D_P)$ and $\beta_{Z_P}(D_P)$ show a dependence on the particle size as expected due to particle diffusion (chapter 3.4.1.1.4). The pressure dependency as predicted by the theory shown in figures 4.5.1.1 has not been found. The reason for the deviation from the theory is probably inaccurate measurements of the volume flows under subatmospheric pressure. Since the clean air mass flow has to be adjusted for each pressure, the DMA runs with different sets of volume flows causing different $\alpha_{Z_P}(D_P)$ and $\beta_{Z_P}(D_P)$ of the transfer functions. However this does neither restrict the functionality of the measurement system nor the validity of the transfer functions as long as for every pressure always the same flow adjustment is guaranteed.

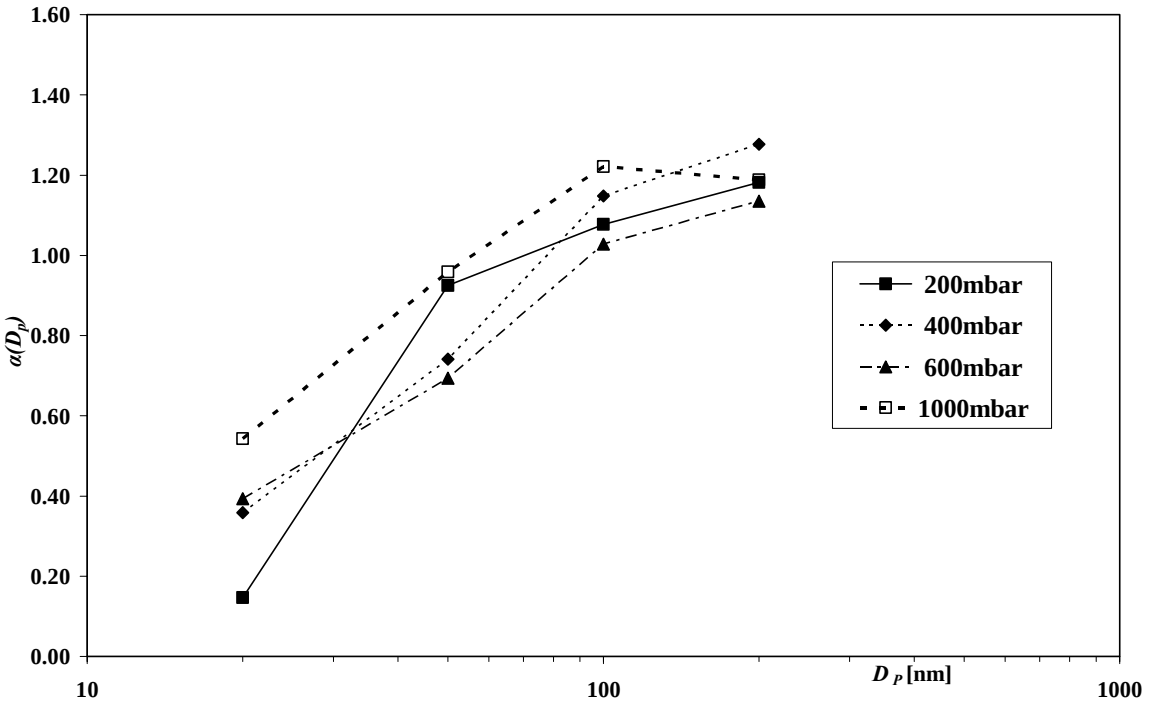

Figure 4.5.3.2: Experimentally determined heights of the transfer function α_{Zp} as a function of D_P

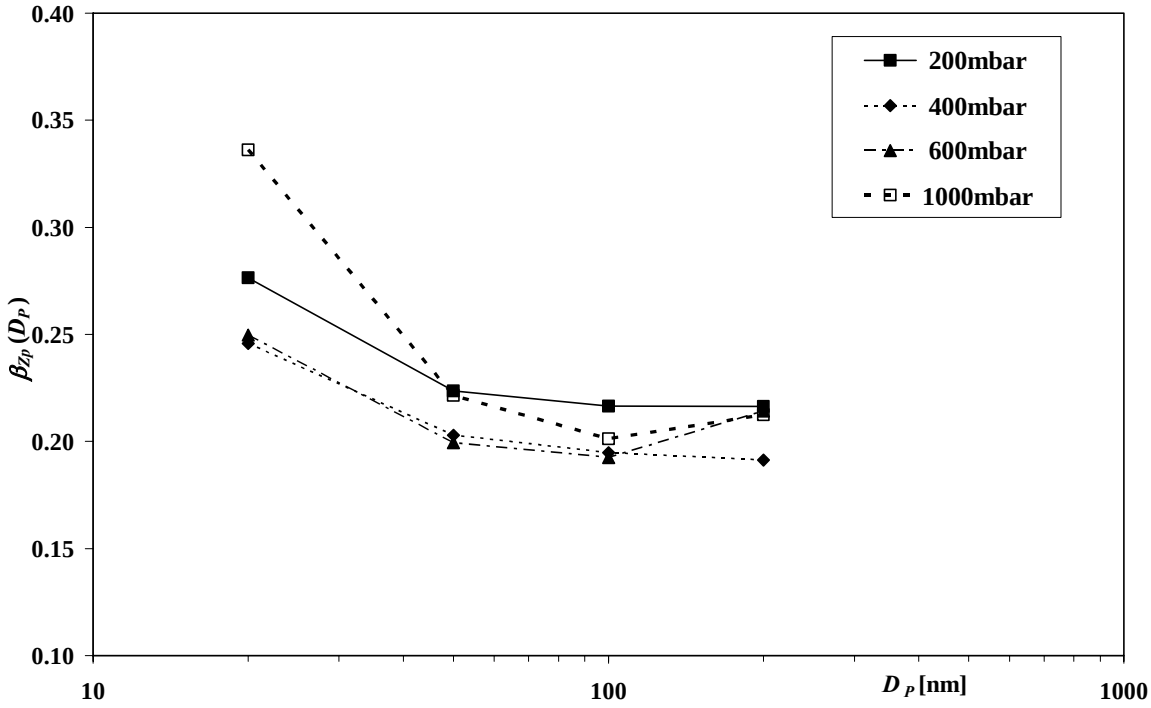

Figure 4.5.3.3: Experimentally determined widths of the transfer function β_{Zp} as a function of D_P

An effect on $\beta_{Z_P}(D_P)$ can also be caused by:

a) imperfections of the geometry causing a inhomogeneity of the gas flow e.g. no azimuthal symmetry (for example no perfect parallelism of the electrodes)

b) inhomogeneity of the electrical field

c) turbulences of the gas flow

Inhomogeneities of the gas flow and of the electrical field are difficult to determine. Turbulences of the gas flow are not assumed since the maximum Reynolds number is 670.7 (chapter 4.5.1). In case of $\dot{V}_a > \dot{V}_s$ the ideal transfer function is a trapezoid. The experimental values for $\alpha_{Z_P}(D_P)$ and $\beta_{Z_P}(D_P)$ then give a coextensive triangle which takes diffusional broadening into account. The data inversion algorithm which will be introduced in chapter 4.7 needs only information about the width of the mobility window from $Z_P^*(1-\beta_{Z_P})$ to $Z_P^*(1+\beta_{Z_P})$ and of the average probability $\overline{\Omega(Z_P)}$ for a particle with a mobility in between to pass the DMA. $\overline{\Omega(Z_P)}$ is a rectangular function given by

$$\overline{\Omega(Z_P)} = \frac{\alpha_{Z_P}}{2} \cdot \mathrm{rect}\left(\frac{Z_P - Z_P^*}{Z_P^*(1+2\beta_{Zp})} \right) \tag{4.5.3.5}$$

The rect function is defined as

$$\mathrm{rect}\left(\frac{x}{w}\right) = \begin{cases} 0\,; & x < -\frac{w}{2} \\ 1\,; & -\frac{w}{2} \le x \le \frac{w}{2} \\ 0\,; & x > \frac{w}{2} \end{cases}$$

A deviation from matched flow condition can lead to a shift in the dependency between the DMA voltage and the corresponding electrical mobility $Z_P^* = \frac{\left(2\cdot\dot{V}_a + \dot{V}_c - \dot{V}_s\right)\cdot b}{2\cdot\pi\cdot\left(R_2^{\,2} - R_1^{\,2}\right)\cdot U}$. Therefore the relationship between the LPDMA voltage and the particle size has been evaluated for various pressures and particle sizes in the laboratory. The setup for the experiment is shown in figure 4.5.3.4. A TSI SMPS has been used to compare the LPDMPS raw data (electrometer output voltage U_{elec}) to. For the SMPS the raw data is the number of photo detector pulses per size channel and time. The reason for the comparison of the raw data is that the different charge correction algorithms should not be taken into account. The test aerosol was silver particles generated by an evaporation- condensation process (Scheibel *et al*. [63]). For the calculations of the LPDMA voltages the pressure dependences of λ and C_C have been taken into account. An example for this comparisons is given in figure 4.5.3.5 for a particle size D_P = 90nm.

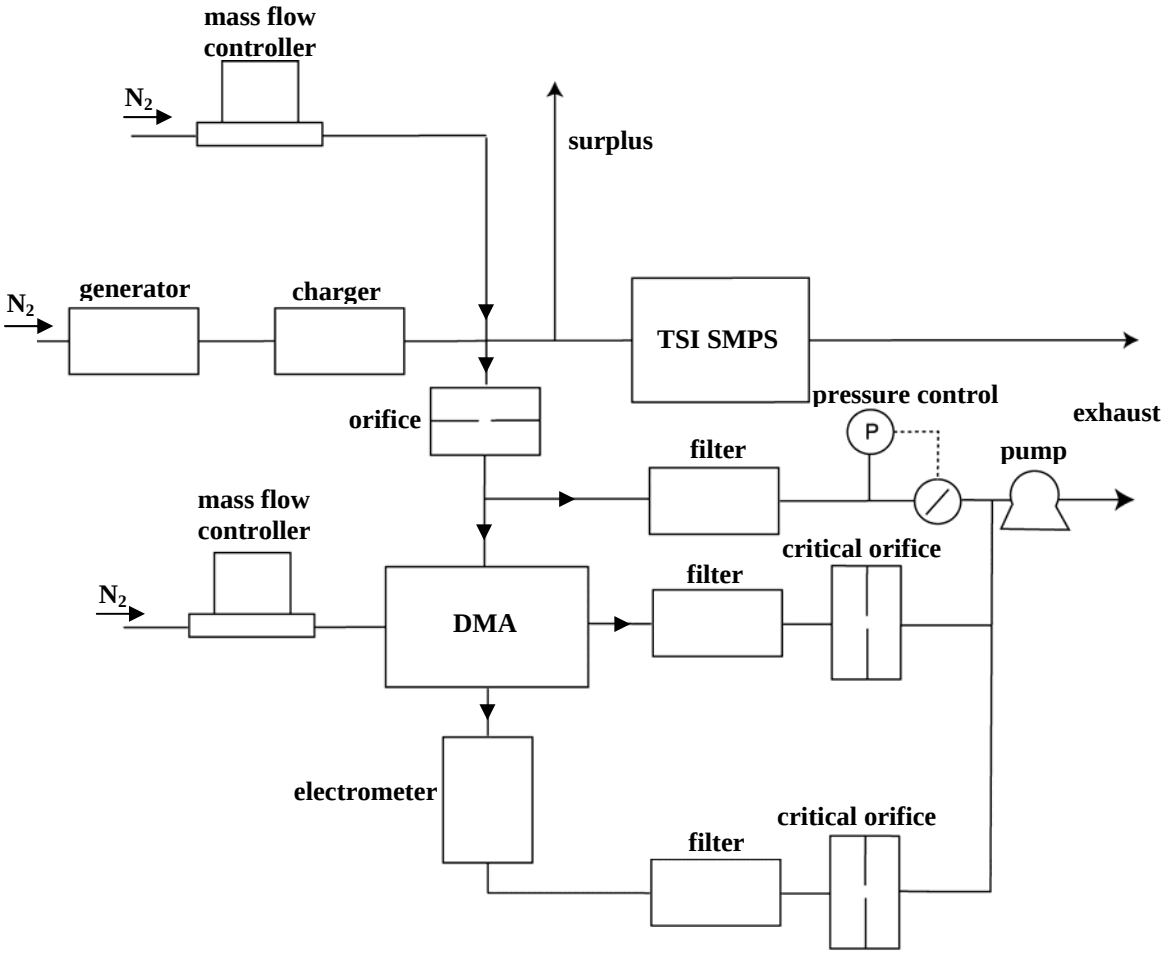

Figure 4.5.3.4: Setup for the comparison of LPDMPS to TSI SMPS

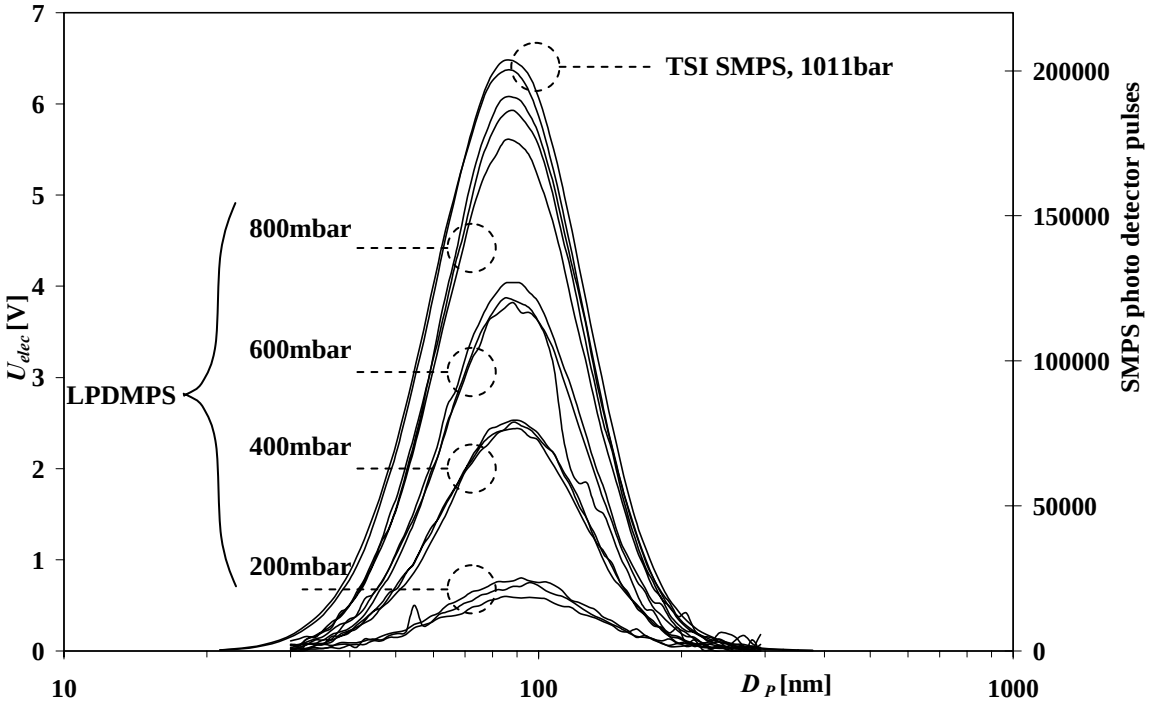

Figure 4.5.3.5: LPDMPS raw data U_{elec} compared to SMPS raw data as a function of D_P

4.6 Electrometer

For the detection of the number of particles passing the DMA, an electrometer is used since it is the only instrument able to operate under the prevailing process conditions (low pressure, presence of HCl, high concentrations). For the new LPDMPS a new electrometer has been developed which is made from standard Hastelloy C4 pipe and flange components, what kept the costs low and has made the instrument resistive against corrosion. Also an electronic circuit also has been developed newly. The detection limit of the electrometer is about $2 \cdot 10^{-15}$A which for a volume flow of 0.33lmin^{-1} corresponds to a particle number concentration of 1000cm^{-3}. The electrometer can be subdivided into two main parts:

1. The housing, which must filter the aerosol within an electrically conducting encapsulation and which allows to measure the displacement current outside the filter chamber. The displacement current is caused by the charges on the particles and can be measured between the surface of the Faraday cup and the housing. The conductivity of the housing protects against capacitive coupling.

2. The electronic circuit which has to transform the very low power signal into a manageable quantity.

4.6.1 Electrometer housing

The principle of the electrometer housing for low pressure application is illustrated by figure 4.6.1.1.

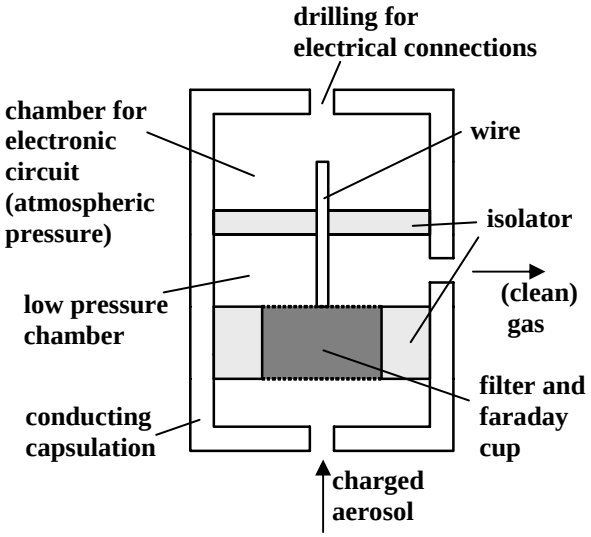

Figure 4.6.1.1: Electrometer housing (principle)

After having entered the device the aerosol should immediately reach the Faraday cup in order to minimize losses of particles due to diffusion. Therefore the first critical point is the aerosol path from the entrance to the filter. Since the aerosol completely has to pass the filter, the latter must be sealed by an isolating material. Out of reasons discussed below, the conductivity of the electrical isolation of the filter must be extremely low. The same is valid for the isolation of the wire by which a connection to the atmospheric pressure chamber is realized. For applications where no corrosive gas or vapour is present, the electronic circuit can be situated directly downstream the filter, in the chamber which is filled with the filtered process gas. For the new LPDMPS this is not possible. The isolators are a further critical point of the design of the electrometer. The third critical point is the electronic circuit, which is described in chapter 4.6.2. For a schematic of the electrometer housing see appendix A4, figure A4.1.

The instrument is rotationally symmetrical (apart from screws, bolts and outlet). The parts which isolate the filter cup are made from PVC. Its specific conductance κ is in the order of $\frac{1}{10^{16}\Omega\text{cm}}$ which leads to a total resistance of the isolating parts of about $2 \cdot 10^{15}\Omega$. In chapter 3.4 it has been discussed, why it is important, that the isolation resistance is sufficiently high. The particles are conducted through a fibre filter of the type Ultra Filter type H cartridge by MSA^{TM}, Pittsburgh, USA with a filter efficiency of 99.5% (Mine Safety Appliances [76]). The filter is removed from its original aluminium cup and situated in a cup, which is made from Hastelloy C4. The latter is perforated at top and bottom. It is pressed into a conical milling by a spring, which in connection with a rod serves as wire for the displacement current into the circuit board chamber. It

is separated from the low pressure chamber of the instrument by a sealed PVC disk. The circuit board is fastened by four screws on matching bolts.

4.6.2 Transformer circuit

The lowest currents detectable with an electrometer are in the range 10^{-16}A to 10^{-15}A for d.c. measurements. The detection limit is determined by noise. For the contemporary commercial aerosol electrometer TSI type 3068A the noise level is quantified with $2 \cdot 10^{-15}$A corresponding to 1253 singly charged particles for a volume flow of 0.3lmin^{-1} (TSI [52]).

Electrometer circuits consist of a current- voltage converter and a voltage amplifier stage. The current-voltage converter has a differential input of which the non- inverting input is connected to the reference potential (e.g. 0V), the inverting input is connected to the capsulation of the aerosol filter. For the measurement of extremely low currents the input impedance of the differential amplifier has to be extremely high. Contemporary electrometer circuits use integrated operational amplifiers. Special techniques (JFET, DIFET) offer high impedance and a comparatively low temperature drift. A basic circuit of a current- voltage inverter using an operational amplifier is shown in figure 4.6.2.1(Tietze *et al.* [72]).

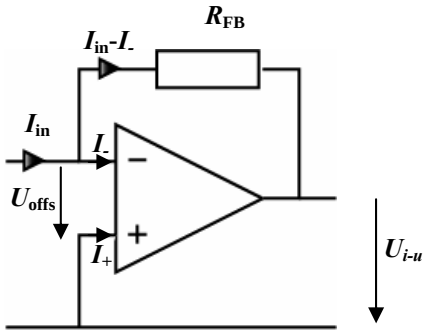

Figure 4.6.2.1: Current-voltage converter using an operational amplifier

For an ideal operational amplifier the idle running voltage gain $A_0 \to \infty$ and the voltage between the non-inverting input (+) and the inverting input (-) $U_{\text{offs}} = 0$. The input currents are zero ($I_+ = I_- = 0$), the current I_{in} to be measured flows through the feedback resistor R_{FB}, and the output voltage U_{i-u} of the current voltage converter stage equals $U_{i-u} = -R_{\text{FB}} \cdot I_{\text{in}}$. For the measurement of currents in the range of 10^{-15}A, the feedback resistance has to be in the range of about $10^{12}\Omega$ or higher. The high resistance is one of the crucial points of the circuit. Coal resistors are not suitable because of their noise and temperature sensitivity. Metal film resistors are available up to $10^{12}\Omega$. Thus with a current of 10^{-15}A, the output voltage of the converter stage ideally would be 1mV. In reality offset voltage, offset and bias currents are not zero and do affect the

dependency of $U_{i\text{-}u}$ on I_{in} because the operational amplifier has to provide its own offset voltage and current (over the feedback resistor and isolators).

In table 4.6.2.1 the important parameters are listed for two operational amplifier IC which are suitable for the application as current- voltage converter. The IC are the type ICH8500A by Intersil™ and the type OPA128LM by Burr Brown™ (Intersil [30], Burr Brown [58]).

Table 4.6.2.1: Parameters of operational amplifiers

Parameter	ICH8500A	OPA128LM
I_{bias}	typ. 10fA	max. 75fA
I_{offs}	no specification	max. 30fA
U_{offs}	max. 50mV	max. 500µV
drift(I_{bias})	no specification	no specification
drift(I_{offs})	no specification	no specification
drift(U_{offs})	no specification	max. 5µV/°C

I_{bias} is average of the input currents of the inverting and non-inverting input, I_{offs} the difference of the input currents. U_{offs} is the voltage between the inputs for the case, that the output is zero. The reason for the demand for high input impedance and a low input current is, that with such a high feedback resistance the output voltage, necessary to provide the input current, can be outside the working range of the device. It is because of the same reason, that the isolation resistance between filter cup and housing must be so high, because the current through the isolation must be additionally provided by the output of the operational amplifier.

The values for the OPA128 show that for a measured current of 1fA the average input current I_{bias} is almost hundred times the measured current. This fact alone is not crucial. For idle running there will just be an offset to the output voltage of $-10^{12}\Omega \cdot 75\text{fA} = -75\text{mV}$ assuming a feedback resistance of $10^{12}\Omega$. Decisive is the question how stable the input currents are and if they depend on the output voltage, temperature, time, and so on. If for example I_{bias} fluctuates by only 1% a measured current of 1fA would not be resolvable. Similar with respect to the offset voltage U_{offs}. The problem is not the presence of the offsets but that they drift or fluctuate. Fluctuations of the offsets result in noise of the current- voltage converter. Unfortunately drift and fluctuations of I_{offs}, I_{bias} and U_{offs} are difficult to quantify and statements for commercial operational amplifiers are in general not given. For example for the OPA128 only the temperature drift of U_{offs} is given in the datasheet. A careful investigation and selection of devices of the same type can reveal enormous differences as to their performance.

The temperature is one reason for changes of the behaviour of the circuit. One possibility for compensation is to cool or heat the circuit and to keep its temperature constant but that would mean great expense with

respect to design, circuitry, energy consumption, and experimental investigation. However it can be assumed that I_{bias} is always much higher than I_{off}, and that a change of the temperature would affect both input currents by the same magnitude. Under these assumptions the effects of temperature on the offsets can be compensated using the circuit shown in figure 4.6.2.2 (Seifart [64]).

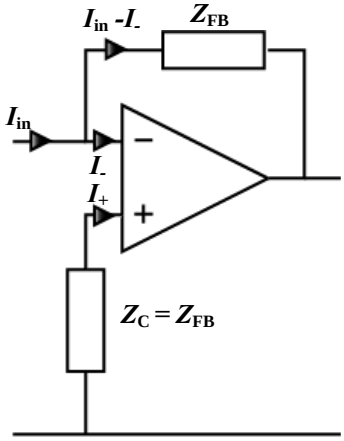

Figure 4.6.2.2: Compensation of the temperature drift of I_{bias}

Assumed that I_- as well as I_+ change by the same amount, the potentials of both inputs will vary by the same value, since the difference as to the voltage drop across the impedances is equal. So the voltage between the inputs does not change and the output voltage remains constant.

Since the electrometer is used for d.c.- measurements, it is possible to reduce the noise by giving the device a low pass behaviour at the first stage. Therefore Z_{FB} and Z_C have to be RC- elements with convenient time constants.

Apart from the temperature, further influences can cause fluctuations of the input currents, in- and output voltages. The reasons are partly to be found within the devices itself, partly in the environment. Examples are spontaneous changes of the material, aging, changes of the properties of the isolator, changes of surface- and air conductivity, electromagnetic and acoustic irradiation, which are typical electromagnetic compatibility (EMC) problems and difficult to deal with. Special care has to be taken of the mechanical set-up of the circuit. To minimize influences of the surface conductivity, all components have to be carefully cleaned with ether, and not to be touched afterwards. Using a printed circuit board (PCB), the “hot” wires, that is the connections from the inputs of the operational amplifier to the feedback- and compensation impedances, and from the filter cup to the operational amplifier have to be realized as air wires (figure 4.6.2.3). The capacitors have to have a very low (leakage-) conductivity. Therefore polystyrol- or Styroflex^{TM} types have to be used.

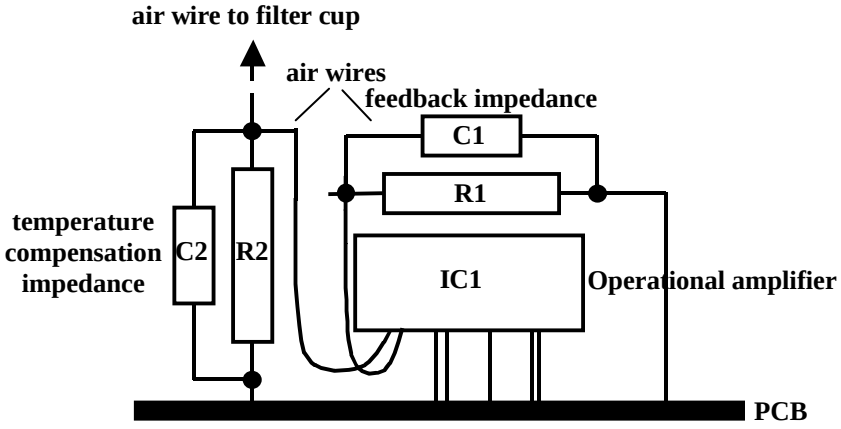

Figure 4.6.2.3: Air wires for the sensitive wires of the current-voltage converter

The schematic of the transformer circuit of the electrometer is given in figure 4.6.2.4. The parts are listed in table 4.6.2.2. The circuit has a current to voltage converter and an amplifying stage. The current to voltage converter is drift compensated by connecting the non-inverting input to the ground by an impedance identical to the feed back impedance, consisting of C_1 and R_1. The role of C_1 is the reduction of noise. The low pass filter by R_1 and C_1 has a time constant of 4.4s. The d.c. sensitivity of the converter stage theoretically equals $U_{stage1} = -I_{in} \cdot R_1$. The gain v_U of the amplification stage is determined by R_3 and R_4.

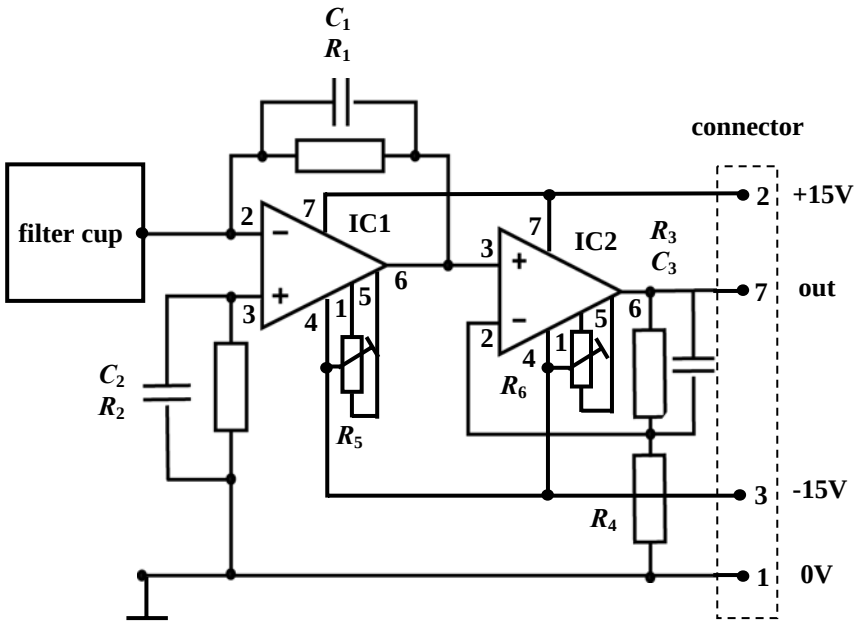

Figure 4.6.2.4: Schematic of the electrometer transformer circuit

Table 4.6.2.2: List of the parts of the transformer circuit

*IC*1	OPA128LM
*IC*2	OP07
C_1	22pF
C_2	22pF
C_3	1µF
R_1	200GΩ
R_2	200GΩ
R_3	100Ω
R_4	100KΩ
R_5	100KΩ
R_6	22KΩ

As feedback and compensation resistances $R_1 = R_2 = 200\text{G}\Omega$, 500GΩ, and 1000GΩ have been tried. For 200GΩ the circuit has shown the best behaviour as to sensitivity in relation to noise. A gain $v_U = \left(1 + \frac{R_3}{R_4}\right) = 1001$ for a d.c. amplifier stage is comparatively high. However it showed excellent stability.

The theoretic current $I_{\text{in,theor}}$ to be measured by the electrometer is $I_{\text{in,theor}} = -4.995 \cdot 10^{-15} \cdot U_{out} \cdot \frac{\text{A}}{\text{V}}$.

With regard to the high isolation resistance, the connections to the inputs of the operational amplifier IC1 have been realized by air wires. The isolating parts (PVC) as well as IC1, R_1, R_2, C_1, C_2 have been carefully cleaned with ether. Since the resistance of the isolation is difficult to determine and because to generate small currents is as difficult as to measure them, the electrometer sensitivity has been determined as electrometer output voltage per charged particle for a certain aerosol volume flow.

4.6.3 Experimental determination of the electrometer sensitivity

The experimental set up, which has been used for the determination of the sensitivity of the electrometer, is sketched in figure 4.6.3.1. In a tube furnace silver particles are generated (Scheibel *et al.* [63]), charged by a Kr^{85} radioactive source and separated by a DMA. The DMA size fractionizes the aerosol and allows adjusting the particle number concentration. A UCPC nucleus counter is used as a reference.

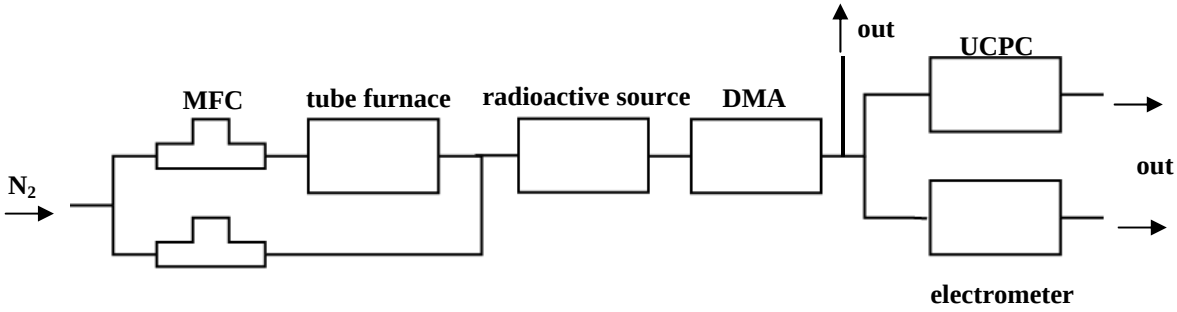

Figure 4.6.3.1: Setup for the determination of the electrometer sensitivity

The plumbing between DMA and UCPC and DMA and electrometer have the same lengths, also the volume flows were almost identical (0.3lmin^{-1} through the UCPC and 0.33lmin^{-1} through the electrometer). Consequently for diffiusional losses is made up. The UCPC is the type 3025A by TSI. The particle sizes were 17nm to 30nm, where all particles leaving the DMA are singly charged and the counting efficiency of the UCPC is 100%. The electrometer sensitivity has been calculated by relating the electrometer output signal to the concentration indicated by the UCPC.

As an example in figure 4.6.3.2 the response of the electrometer is shown for a concentration of 1000cm^{-3}. The electronic current by the moving charged particles is 10^{-15} A . For the calculation of the sensitivity the mean values of 8min have been taken. The concentration has been switched abruptly by switching the DMA voltage from 0 to a certain value. After the switching, one minute has been awaited until the first electrometer output signal has been recorded. The experiments have been made for various concentrations. The sensitivity has been determined to be 68µV per singly charged particles for a volume flow of 0.33lmin^{-1}. It is assumed to be independent from pressure. With 0.33 l/ min and an averaging time of ten seconds, the detection limit as to the concentration is about 10^3cm^{-3}. For various volume flows $\dot{V}_{\text{elec}}$ and number of elementary charges q the sensitivity S_{elec} of the electrometer can be given as

$$S_{\text{elec}} = 68\mu\text{V} \cdot \frac{q \cdot \dot{V}_{\text{elec}}}{0.33\text{l}\,\text{min}^{-1}} \cdot \frac{1}{\text{cm}^{-3}} . \qquad (4.6.3.1)$$

The particle number concentration N measured by the electrometer is $N = \frac{U_{\text{elec}}}{S_{\text{elec}}}$. The theoretical electrometer output voltage $U_{\text{elec,theor}} = -I_{\text{part}} \cdot R_{FB} \cdot \left(1 + \frac{R_3}{R_4}\right) = 209\mu\text{V}$ leading to a theoretical sensitivity

$$S_{\text{elec,theor}} = 209\mu\text{V} \cdot \frac{q \cdot \dot{V}_{\text{elec}}}{0.33\text{l}\,\text{min}^{-1}} \cdot \frac{1}{\text{cm}^{-3}} . \qquad (4.6.3.2)$$

The deviation of the experimental from the theoretical sensitivity is a consequence of the conductivity of the electrical isolation of the filter cup. As typical for operational amplifier circuits the electrometer output voltage range covers −15 to +15V. This voltage range corresponds to a maximum concentration of $2.2 \cdot 10^5$ positively singly charged particles per cm^3 (-15V) to $2.2 \cdot 10^5$ negatively singly charged particles per cm^3 (+15V). Due to the maximum input voltage of 10V of the A/D card the maximum concentration is restricted to $1.5 \cdot 10^5$ singly charged particles per cm^3.

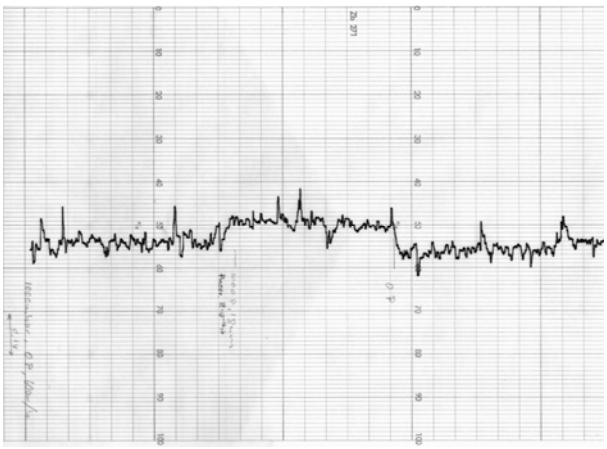

Figure 4.6.3.2: Response of the electrometer for a concentration of 10^3 cm^{-3} for a volume flow of 0.33lmin^{-1}

4.7 Data inversion

4.7.1 Simulation of DMA particle sizing

In the situation of having a charged aerosol already captured in a data file from simulation of charging dynamics (chapter 4.4) it is but consequent to simulate the DMA particle sizing and to evaluate the data inversion algorithm by comparing the inversed DMA output signal to the original size distribution. DMA particle sizing means to sweep the DMA voltage and to deduce from DMA output to the particle size distribution. Since a certain voltage corresponds to one certain mobility but to several particle sizes depending on the charge, sweeping the DMA voltage also means to sweep several windows along the size axis at the same time. The term window is used instead of transfer function because the latter is related to the electrical particle mobility.

Figure 4.7.1.1 shows the size windows for the new LPDMA for a voltage of U_{DMA}=119.1V for $-1 \geq q \geq -10$. As a comparison the figure also shows a log normal size distribution with D_g=50nm, σ_g=1.5 as typical for combustion processes.

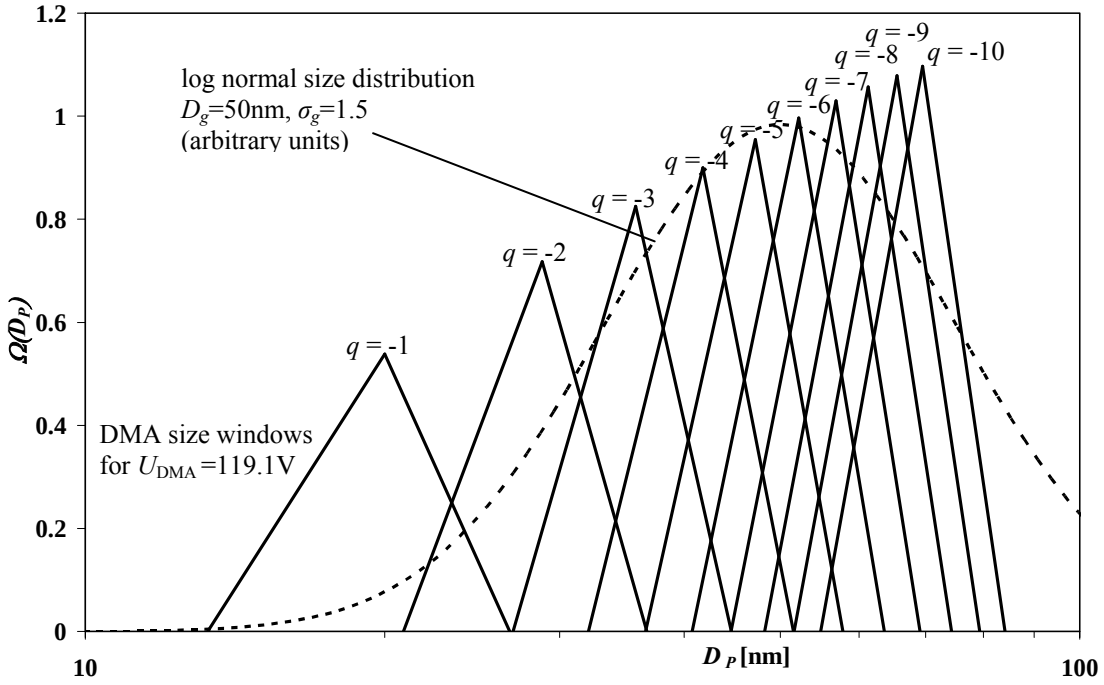

Figure 4.7.1.1: DMA windows for U_{DMA}=119.1V compared to log normal size distribution with D_g=50nm, σ_g=1.5

The windows in figure 4.7.1.1 are given by the half width β_{D_P}, and the height α_{D_P} as calculated by equation 4.5.3.1 (analytical fits of experimental values). The values for D_{Pl} and D_{Pu} of the windows are calculated by equations 3.1.3.2 and 3.1.3.3. In table 4.7.1.1 the windows are given for $-1 \geq q \geq -10$ are listed.

Table 4.7.1.1: New LPDMA, size windows for U_{DMA}=119.1V (nitrogen, 1013mbar, 293K)

q	D_P[nm]	$\alpha_{Dp}(D_P)$	$\beta_{Dp}(D_P)$	$D_{Pl}(D_P)$	$D_{Pu}(D_P)$
-1	20.00	0.5385	0.3362	13.28	26.72
-2	28.80	0.7177	0.2745	20.89	36.71
-3	35.77	0.8254	0.2474	26.92	44.62
-4	41.79	0.8996	0.2329	32.06	51.52
-5	47.20	0.9543	0.2243	36.61	57.79
-6	52.19	0.9964	0.2190	40.76	63.62
-7	56.85	1.0296	0.2155	44.60	69.10
-8	61.26	1.0565	0.2131	48.21	74.31
-9	65.47	1.0785	0.2114	51.63	79.31
-10	69.49	1.0968	0.2103	54.88	84.10

Since within a window the size cannot be resolved, for the inversion of DMA data the triangular window has to be represented by a rectangle of equal area. The result is a constant probability $\Omega = \frac{\alpha_{D_P}(D_P)}{2}$ within $D_{Pl}(D_P)$ and $D_{Pu}(D_P)$ for a particle to pass the DMA (Figure 4.7.1.2).

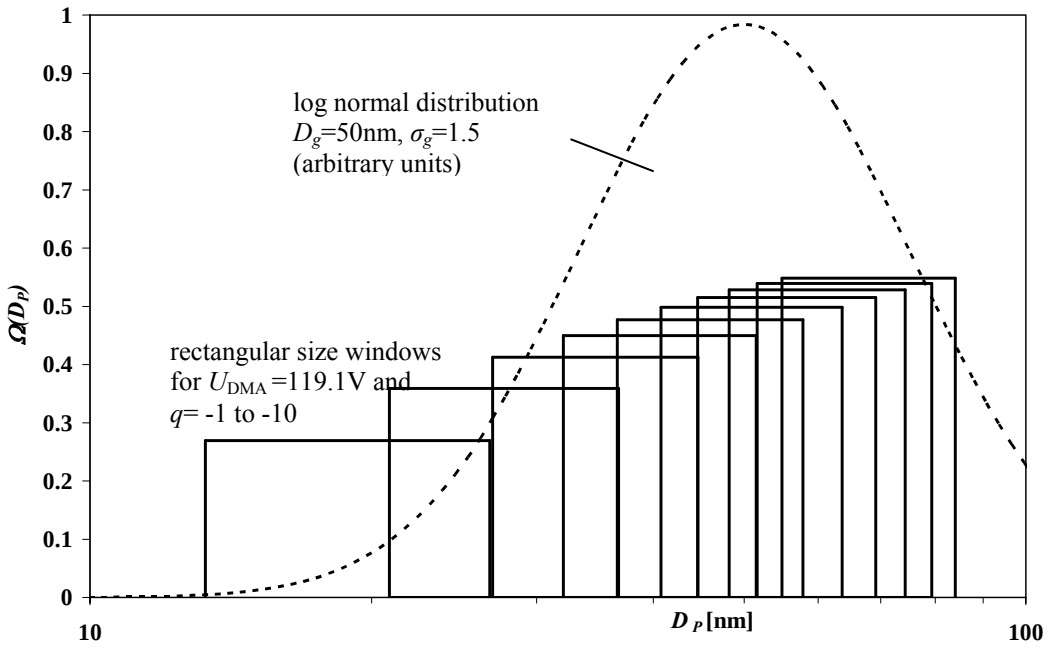

Figure 4.7.1.2: Rectangular windows for the LPDMA as given in table 4.7.1.1 for U_{DMA}=119.1V compared to log normal distribution D_g=50nm, σ_g=1.5

With the windows shown in figure 4.7.1.2 a size classification would be difficult if not the charge fractions decreased with increasing number of elementary charges. When $\Omega(D_P)$ is multiplied by the absolute number of elementary charges $|q|$ and the size fractions $f(q)$ for 119.1V only for doubly charged particles with a mean

size of 28.8nm there is only one window additionally to the one for singly charged particles (figure 4.7.1.3). For 2466.5V (100nm, singly charged) the contribution by windows for multiply charged particles is graver (figure 4.7.1.4). The values for $f(q)$ have been determined by simulations of thermo- and photo charging as described in chapter 4.4 for a log normal distribution with N_{proc}=1.2·10^{8}cm^{-3}, N_{SP}=10^{6}cm^{-3}, σ_g = 1.5.

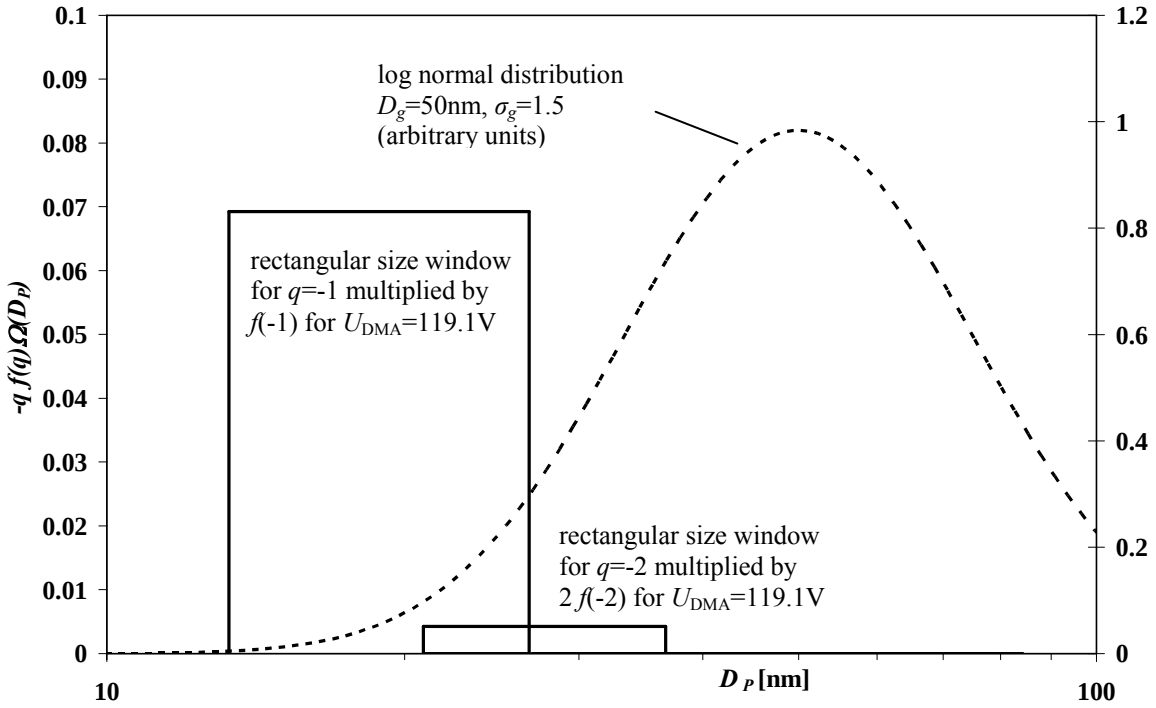

Figure 4.7.1.3: Rectangular windows for the LPDMA as given in table 4.7.1.1 weighted by $-qf(q)$ for q=-1 to -10 and U_{DMA}=119.1V compared to log normal distribution D_g=50nm, σ_g=1.5, the values for $-qf(q)$ have been determined by simulations of thermo- and photocharging as described in chapter 4.4 for a log normal distribution with N_{proc}= 1.2·10^{8}cm^{-3}, N_{SP}= 10^{6}cm^{-3}, D_g=50nm, σ_g=1.5

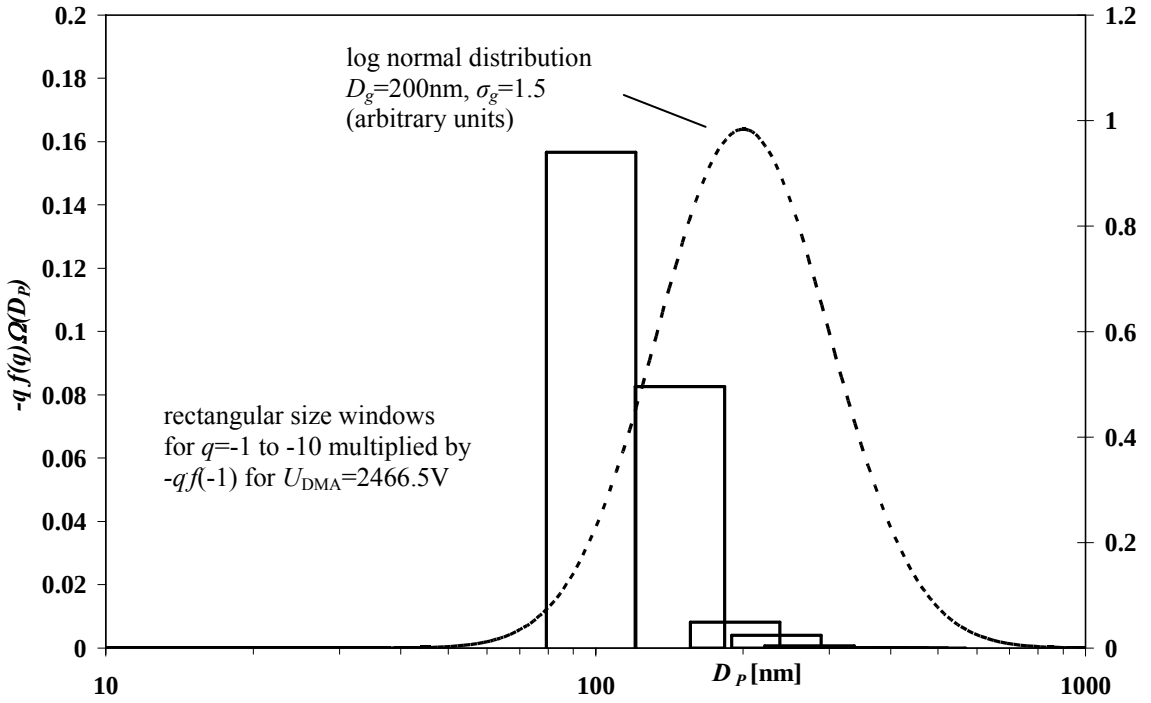

Figure 4.7.1.4: Rectangular windows for the LPDMA (nitrogen, 1013mbar, 293K) weighted by $-qf(q)$ for q=-1 to -10 and U_{DMA}=2466.5V compared to log normal distribution D_g=200nm, σ_g=1.5, the values for $-qf(q)$ have been determined by simulations of thermo- and photocharging as described in chapter 4.4 for a log normal distribution with $N_{proc}=1.2\cdot10^8 cm^{-3}$, $N_{SP}=10^6 cm^{-3}$, D_g=200nm, σ_g=1.5

4.7.2 Data inversion algorithm

Aerosol sizing methods have in general do not classify particles due to their size but due to a size-depending quantity. Since no instrument has a step function response with respect to particle size, much attention has been paid to the problem of the transformation of instrument "raw" data into size spectra (Twomey [75], Kandlikar *et al.* [32]). In the literature this transformation is commonly called "data inversion" or "deconvolution".

For the LPDMPS the raw data is the electrometer output voltage as a function of particle size. Unfortunately there is no one to one correspondence between the raw data and the particle size channels since a particular channel will collect particles from multiple size ranges.

The relationship between the number concentration $N(D_P)$ and the instrument response for the kth channel R_k can be expressed by the Fredholm integral equation (Wolfenbarger [83], Kandlikar *et al.* [32], Talukdar *et al.* [70]):

$$R_k = \int_{D_P=0}^{\infty} K_k(D_P) N(D_P) dD_P + \varepsilon_k \qquad (4.7.2.1)$$

The kernel function $K_k(D_P)$ of the system is given by:

$$K_k(D_P) = \sum_{q=1}^{\infty} f(D_P, q) \cdot \Omega_k(D_P, q) \cdot \Psi(D_P, q) \tag{4.7.2.2}$$

with q the number of elementary charges, ε_k the error in the mobility channel k, $f(D_P, q)$ represents the charge distribution on the particles, $\Omega_k(D_P, q)$ the transfer function of the DMA, and $\Psi(D_P, q)$ the response of the detector. In matrix notation equation (4.7.2.1) becomes

$$\vec{R} = \vec{\vec{A}} \cdot \vec{N} \tag{4.7.2.3}$$

where $\vec{\vec{A}}$ is a $m \times m$ matrix with m being the number of discrete mobility channels. A straight forward inversion of equation 4.7.2.3 $\vec{N} = \vec{\vec{A}}^{-1} \cdot \vec{R}$ in general is not possible because the elements of $\vec{\vec{A}}$ depend on another and because $\vec{\vec{A}}$ is nearly singular. A simple inversion thus would be very sensitive against errors and noise and would lead to oscillating solutions and $N(k) < 0$ (Cooper *et al*. [10]).

Discrete distributions $\vec{N}$ to satisfy equation (4.7.2.3) can found by solving minimizing problems or using smoothing techniques, constraints or initial assumptions like for example $\vec{N}$ be a sum of monotonic functions or a log normal function. A lot of work has been done about mathematical techniques to find appropriate solutions for equation 4.7.2.3 (Lesniec *et al*. [41], Wolfenbarger *et al*. [83], Talukdar *et al*. [70], Tikhonov *et al*. [73]).

For the inversion of LPDMPS raw data a method is used which goes back to Hoppel [25] who presented an iterative data inversion scheme especially for the transformation of DMA electrical mobility data into size distributions. The algorithm converges after a few iterative approximations. The reason why this method is used is its simplicity.

The initial guess $\vec{N}^0 = \begin{pmatrix} N_{01} \\ N_{02} \\ . \\ N_{0m} \end{pmatrix}$ for the discrete size distribution $\vec{N} = \begin{pmatrix} N_1 \\ N_2 \\ . \\ N_m \end{pmatrix}$ is obtained by dividing the recorded electrometer voltages for each channel $U_{\mathrm{elec}}(k)$ by the electrometer sensivity $\vec{N}^0 = \frac{\vec{U}_{elec}}{S_{elec}}$.

Since all detected particles are charged and most of the charged ones are singly charged, a close approximation $\vec{N}^I$ of the number size distribution $\vec{N}$ is given by $\vec{N}^I = \frac{\vec{N}_0}{f(D_P, q=1)}$. $\vec{N}^I$ overestimates the real numbers because in every channel *Z(k)* also multiple charged particle appear. The next approximation $\vec{N}^{II} = \vec{N}^I - \overrightarrow{\Delta N}_{(2)}$ accounts for doubly charge particles. The number of doubly charged particles $\Delta N_{(2)}(k)$ in $N^I(k)$ can be approximated by $\Delta N_{(2)}(k) = \frac{f(D_P, q=2)}{f(D_P, q=1)} \cdot N^0\left(\frac{Z_P(k)}{2}\right)$. The problem is that the electrical mobilities $\frac{Z_P(k)}{2}$ respectively $\frac{Z_P(k)}{q}$ do not necessarily coincide with the preset channels $Z_P(k)$. In order to overcome this problem Hoppel recommended to increase the electrical mobility exponentially $Z_P(k+1) = g \cdot Z_P(k)$ and to let the volume flow ratio be $\frac{\dot{V}_a}{\dot{V}_c} = \frac{g-1}{g+2}$ with constant *g*. Then the channels $Z_P(k)$ are adjoining and non- overlapping. If $g = \sqrt{2}$ the electrical mobilities of multiply charged particles coincide with the preset channels at least for $\frac{Z_P(k)}{2} = Z_P(k-2)$, $\frac{Z_P(k)}{4} = Z_P(k-4)$, and so on. The method requires that the contribution of particles beyond the size scope is negligible and that all particles in the channels of smallest electrical mobility are singly charged because $Z_P(k-j)$ does not exist for $k \le j$. For the data inversion of the LPDMPS it is not assumed that the channels $Z_P(k)$ are adjoining and non-overlapping. Instead the scheme presented by Hoppel [25] has been modified for a more correct consideration of multiply charged particles. This is necessary because the electrometer weights the number of multiply charged particles by the number of charges. It is assumed that $\frac{Z_P(k)}{q}$ in general does not coincide with preset channels. The numbers of multiply charged particles are always estimated by averaging the nearest neighbouring channels. Instead of the electrical mobility the particle size is increased exponentially since the desired quantity is d*N*/dlog(D_P).

As a first approximation all detected particles are taken for singly charged, and the numbers $N^0(k)$ are divided by the fraction $f(D_P, q=1)$ for each size channel. This approximation overestimates the real numbers by the multiple particles. In the next step the contribution of doubly charged particles is estimated. Since the aerosol does not contain particles with a lower mobility than measured in the lowest mobility channel, the particles detected in the lowest mobility channels are all singly charged and the number of particles in the upper size channels of the approximated distribution is free from errors due to multiple charges. Coming from low mobility channels (big sizes) there is one channel, at which multiply charged particles occur for the first time (figure 4.7.2.1).

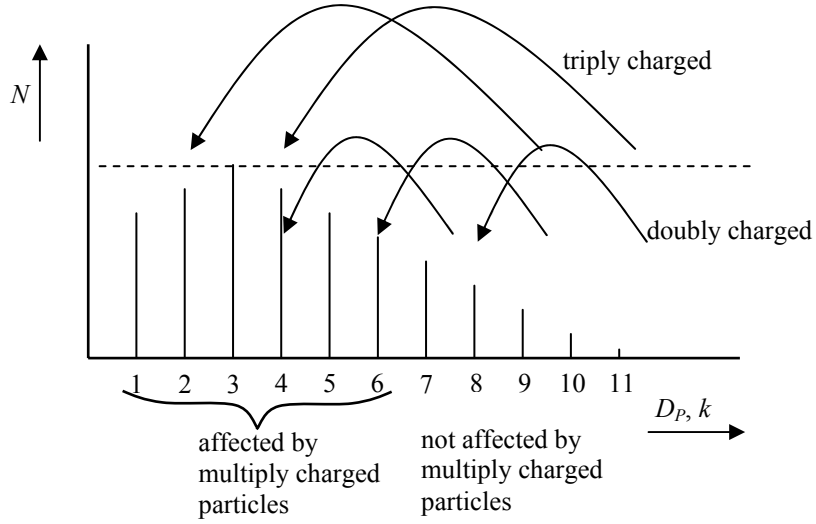

Figure 4.7.2.1: Numbers of particles in the size channels are affected by multiply charged particles

In the example in figure 4.7.2.1 with 11 mobility channels, in channels 7 to 11 only singly charged particles are detected. The number *N(k)* of particles in these size channels in the aerosol can be determined by dividing the initial guess $N^0(k)$ by the fraction $f\left(D_{P\,k=7\ldots11}, q=1\right)$. In Channel 6, the multiply charged particles all carry two charges. The number of particles in this size channel is calculated at first by dividing $N^0(k{=}6)$ by $f\left(D_{P\,k=6}, q=1\right)$, which overestimates the real number, then by subtracting the number of doubly charged particles with a size between those detected in the channels 9 and 10. Since the numbers of particles corresponding to channel 9 and 10 are already known, a good estimate for the number of doubly charged particles can be found by calculating a mean value of the numbers in 9 and 10 which is weighted by the distance between the size of doubly charged particles in channel 6 to the sizes of channels 9 and 10 (Figure 4.7.2.2). Since D_P is increased exponentially, the mean value of real numbers in the channels 9 and 10 is weighted logarithmically with

$$N_x = N_{10}\cdot\log\left(\frac{9\cdot\left(D_{Px}-D_{P,k=9}\right)}{D_{P,k=10}-D_{P,k=9}}+1\right)+N_9\cdot\left(1-\log\left(\frac{9\cdot\left(D_{Px}-D_{P,k=9}\right)}{D_{P,k=10}-D_{P,k=9}}+1\right)\right). \qquad (4.7.2.4)$$

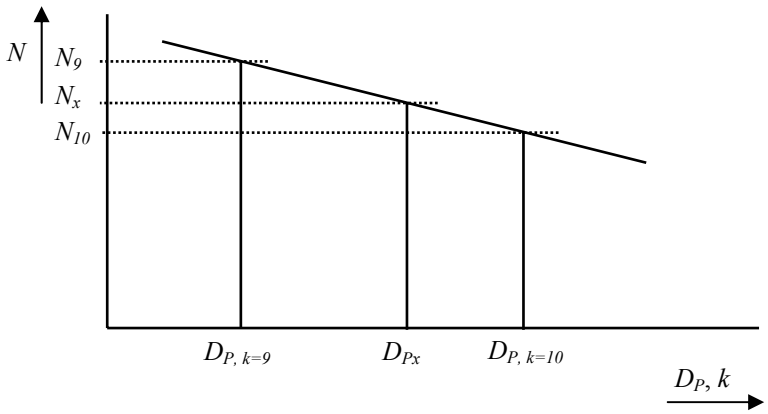

Figure 4.7.2.2: Estimation of the number of particles of the size D_{PX} by equation 4.7.4

Now, with the value for N_x and charge fraction $f(D_{Px}, q=2)$ the approximation $N^I(k=6)$ can be corrected. When the number in channel 6 is known, it can be used to estimate the number of doubly charged particles appearing in channels of smaller sizes. After all channels have been corrected for doubly charged particles, the same procedure has to be performed for triply, fourthly, and so on charged ones until either the fraction $f(D_{Px}, q)$ is zero or the corresponding sizes are above the upper size channel. Multiply charged particles are weighted by the inverse of their number of charges. Figure 4.7.2.3 shows the charge correction procedure in a flow chart. It is important to notice, that the transfer function of the DMA, which is *size* dependent, must be considered *after* the correction as to multiple charges.

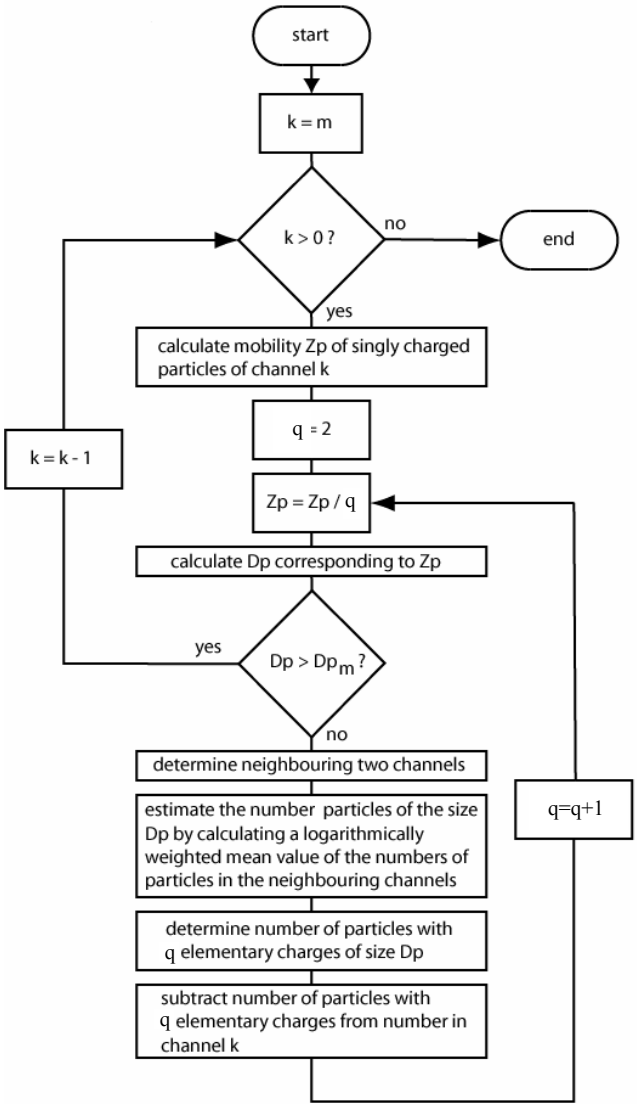

Figure 4.7.2.3: Flow diagram for the correction as to multiple charges

After $\vec{N}(k)$ has been determined, the dilution D_{SP} of the sampling probe, half width $\beta_{Z_p}(D_P)$ and the efficiency $\eta_{DMA}(k)$ of the DMA, and the penetration P (chapter 3.5) have to be taking into account by

$$\frac{\mathrm{d}N(k)_{\mathrm{proc}}}{\mathrm{d}\log(D_P)} = \frac{dN(k)_{\mathrm{proc}}}{\mathrm{d}\log\left(\frac{D_{P,u}}{D_{P,l}}\right)} = \frac{N(k)\cdot D_{\mathrm{SP}}\cdot P(k)\cdot\eta_{\mathrm{DMA}}(k)}{\log\left(\frac{D_P\left(Z_{P,k}\left(1+\beta_{Z_P}(D_P)\right)\right)}{D_P\left(Z_{P,k}\left(1-\beta_{Z_P}(D_P)\right)\right)}\right)}. \tag{4.7.2.5}$$

Equation 4.7.2.5 gives the final result of the calculation of the discrete number size distribution $N(k)_{\mathrm{proc}}$ in the process.

4.7.3 Evaluation of data inversion algorithm for known size distributions

The task of the data inversion for the LPDMPS is to convert the electrometer output signal into a number size distribution. The algorithm introduced in chapter 4.7.2 has been evaluated by performing the simulation of particle charging, simulation of DMA size fractionation, and electrometer counting on different input distributions and by comparing the results of the data inversion to the input distributions. In the simulation of DMA fractionation the transfer function has been assumed to be triangular. In the data inversion the transfer function is represented by a rectangle out of reasons mentioned above. Figures 4.7.3.1 and 4.7.3.2 show the results of the data inversion for various lognormal input distributions.

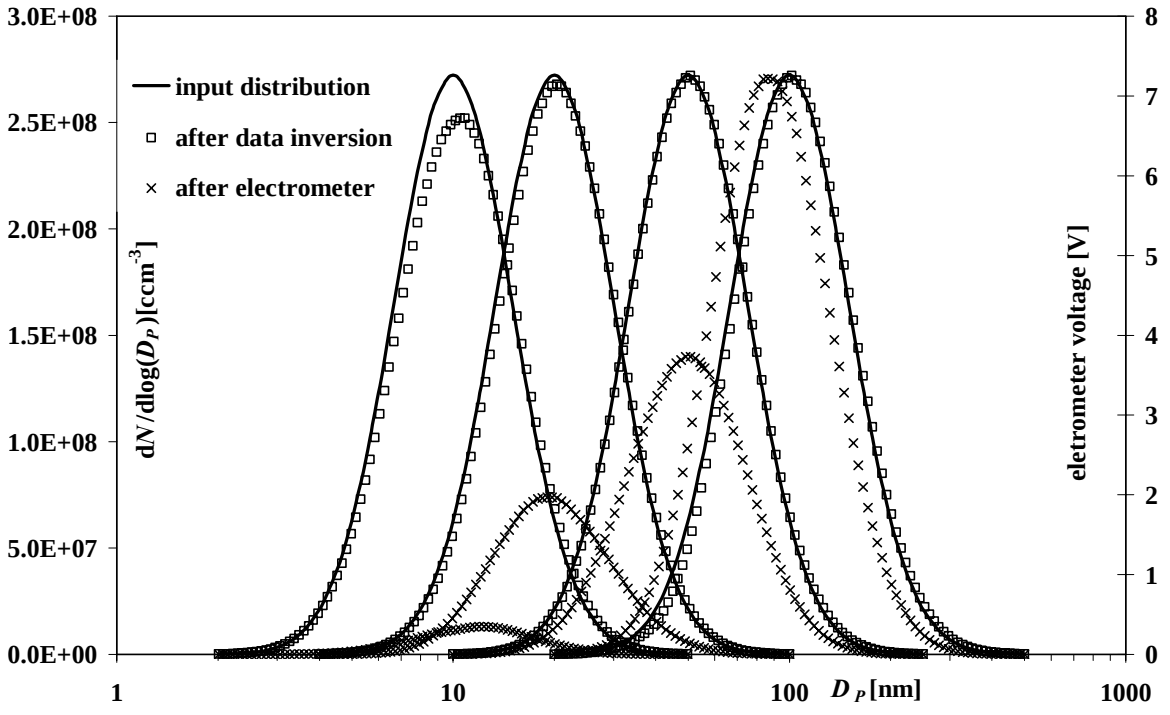

Figure 4.7.3.1: Result of simulation of thermionic charging, photonic charging and size fractionating. Electrometer signal (crosses) and result of data inversion (rectangular dots) compared to lognormal input distribution (solid line) for D_g=10nm, D_g=20nm D_g=50nm, and D_g=100nm (σ_g=1.50, N_{proc}=1.2·10^{8}cm^{-3}, N_{SP}=10^{6}cm^{-3}, p=1013.0mbar, T_{proc}=1673.0K, 100 size channels). The electrometer signal from left to right is for D_g=10nm, D_g=20nm D_g=50nm, and D_g=100nm.

For size distributions with D_g=20nm to D_g=100nm the data inversion algorithm well restores the input distribution. For D_g=10nm a deviation can be seen which is caused by the fact that for small particle sizes $\beta_{Z_P}(D_P)$ increases and subsequently the error due to averaging the charge fractions and particles numbers inside the size window. The number of DMA size channels in figure 4.7.3.1 and 4.7.3.2 is 100. For size distributions with particles D_g > 200nm the impact of multiple charges becomes grave, which can be seen by the large difference between electrometer signal and input distribution (figure 4.7.3.2). Errors due to averaging the charge fractions and particles numbers increase because the number of corrections of the lower channels (left side of the curves) grows strongly since $f(-1)$ decreases strongly in relation to $f(q)$ for $q < -1$ (figure 4.7.3.3). The charge fractions for D_g=20nm are given in figure 4.7.3.4.

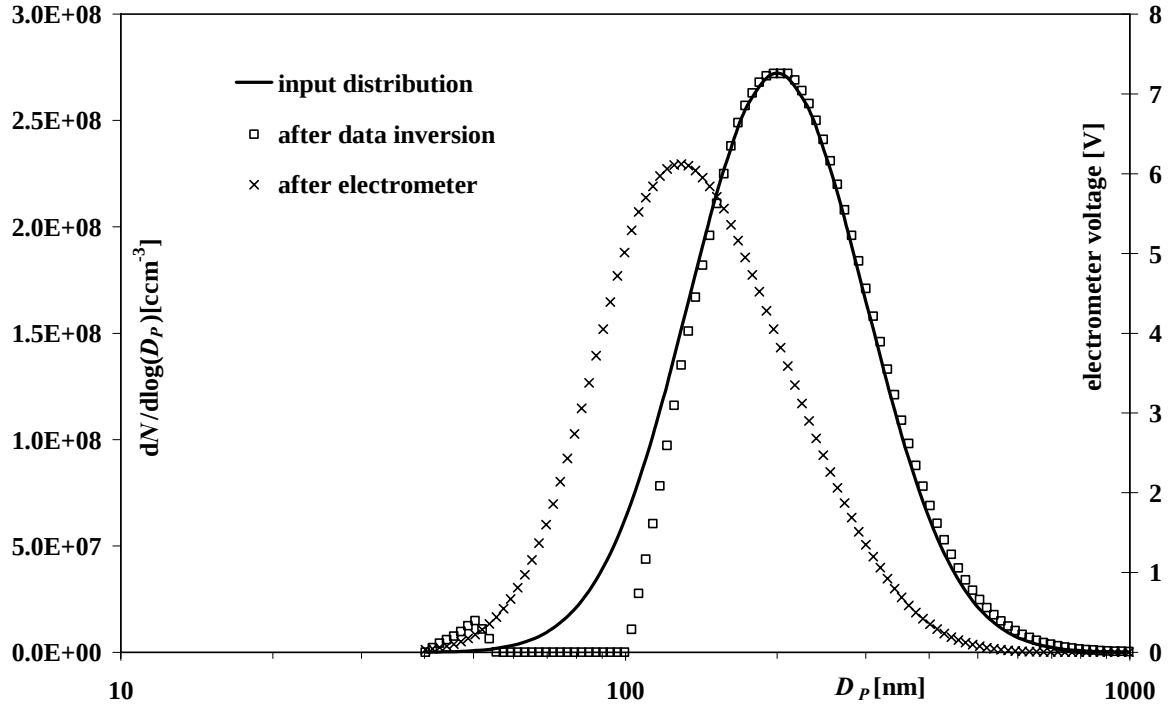

Figure 4.7.3.2: Result of simulation of thermionic charging, photonic charging and size fractionating. Electrometer signal (crosses) and result of data inversion (rectangular dots) compared to lognormal input distribution (solid line) for D_g=200nm (σ_g=1.50, N_{proc}=1.2·10^{8}cm^{-3}, N_{SP}=10^{6}cm^{-3}, p=1013.0mbar, T_{proc}=1673.0K, 100 size channels)

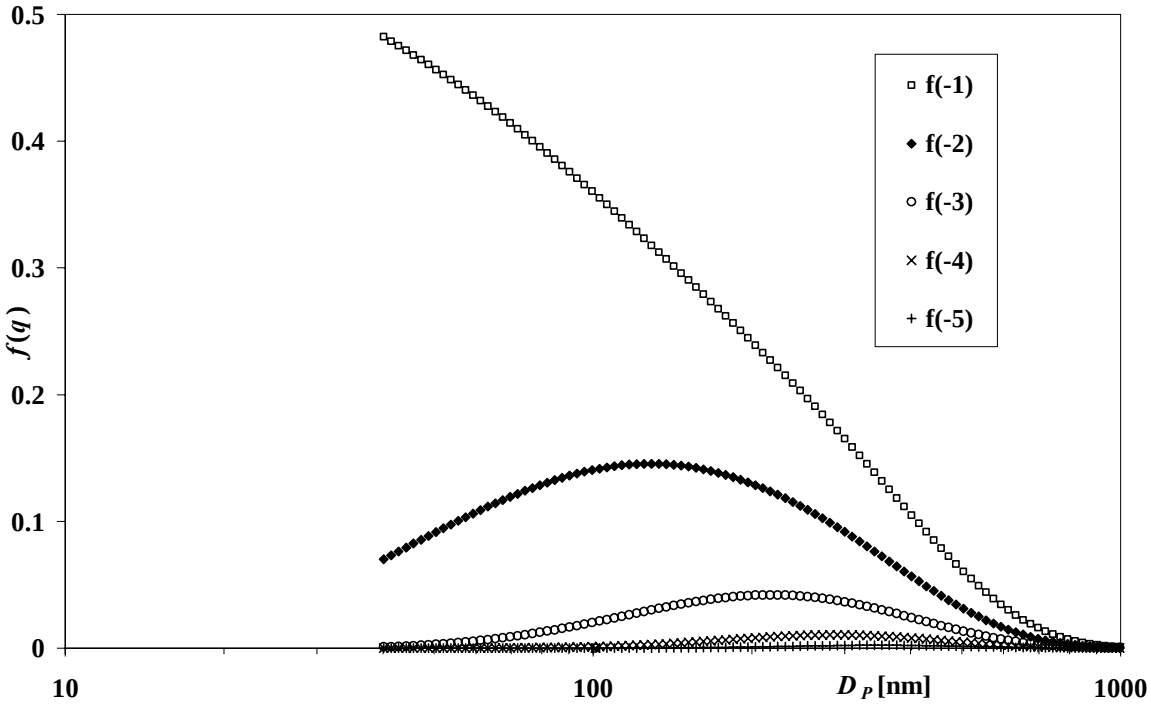

Figure 4.7.3.3: Charge fractions $f(q)$ as a result of simulation of thermionic and photonic charging for lognormal input distribution with D_g=200nm (σ_g=1.50, N_{proc}=1.2·10^{8}cm^{-3}, N_{SP}=10^{6}cm^{-3}, p=1013.0mbar, T_{proc}=1673.0K)

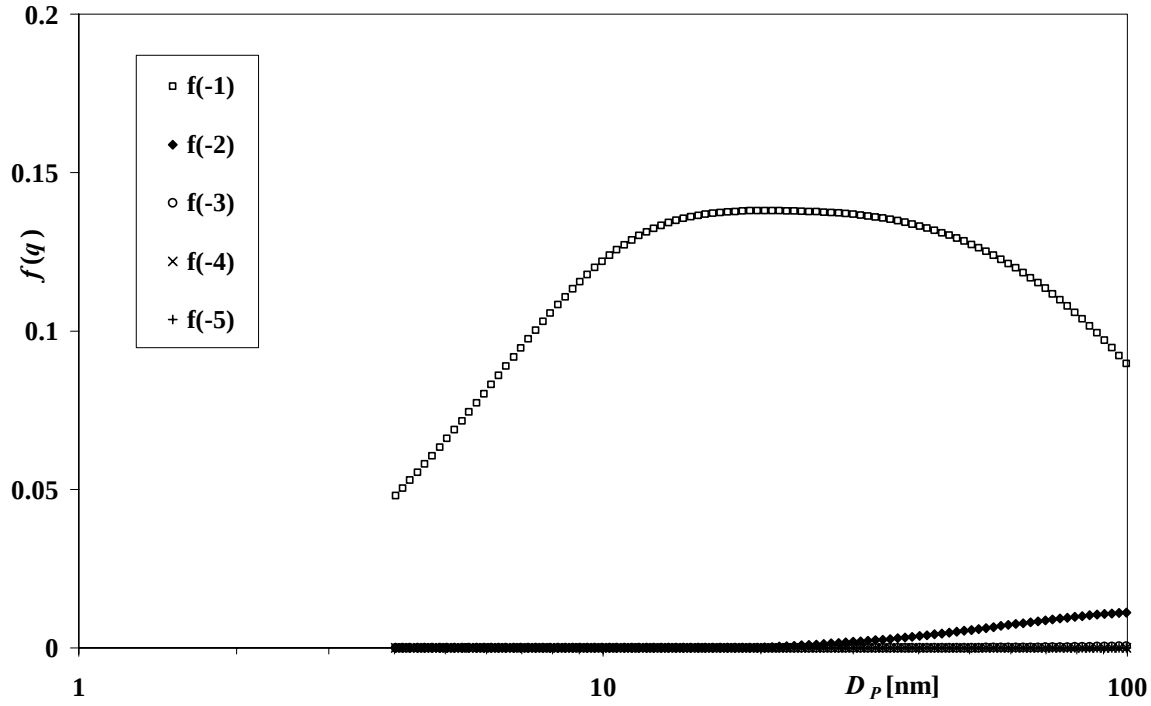

Figure 4.7.3.4: Charge fractions $f(q)$ as a result of simulation of thermionic and photonic charging for lognormal input distribution with D_g=20nm (σ_g=1.50, N_{proc}=1.2·10^{8}cm^{-3}, N_{SP}=10^{6}cm^{-3}, p=1013.0mbar, T_{proc}=1673.0K)

In order to reveal the limits of the data inversion it is interesting to look how it responds to a step function. Therefore a rectangular distribution has been taken as input for the simulation. The results of DMA size fractionating and data inversion are shown in figure 4.7.3.5.

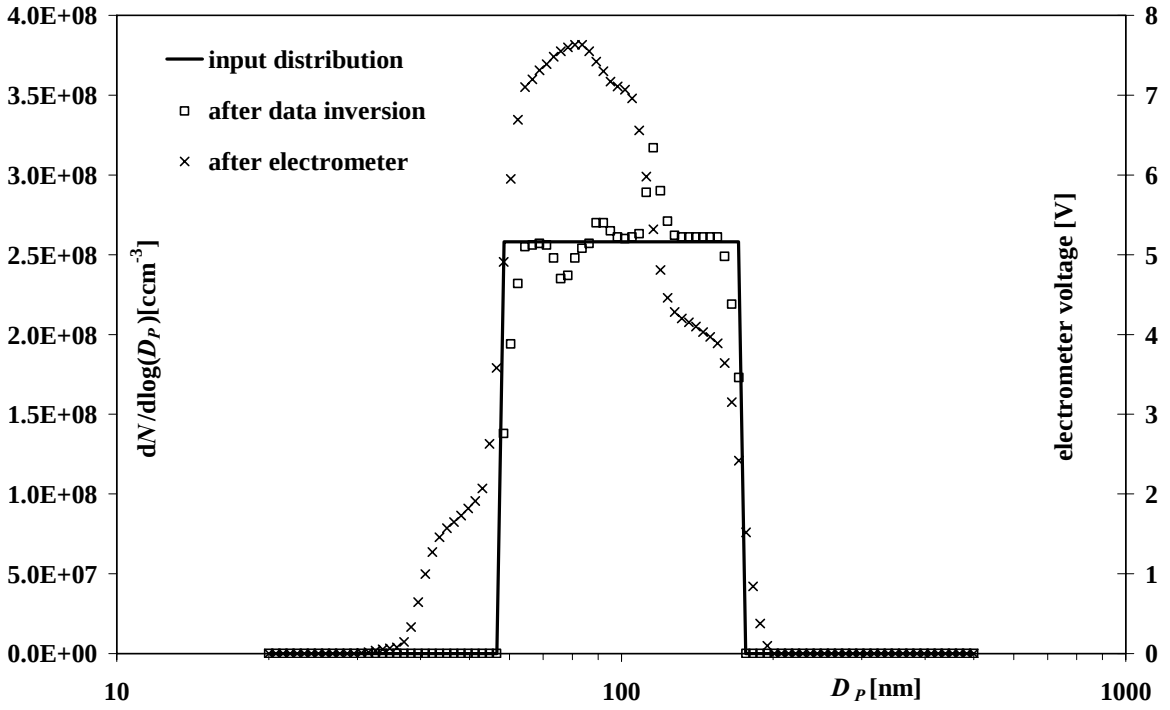

Figure 4.7.3.5: Result of simulation of thermionic charging, photonic charging and size fractionating. Electrometer signal (crosses) and result of data inversion (rectangular dots) compared to rectangular input distribution (solid line) for D_g=100nm (N_{proc}=1.2·10^{8}cm^{-3}, N_{SP}=10^{6}cm^{-3}, p=1013.0mbar, T_{proc}=1673.0K, 100 size channels)

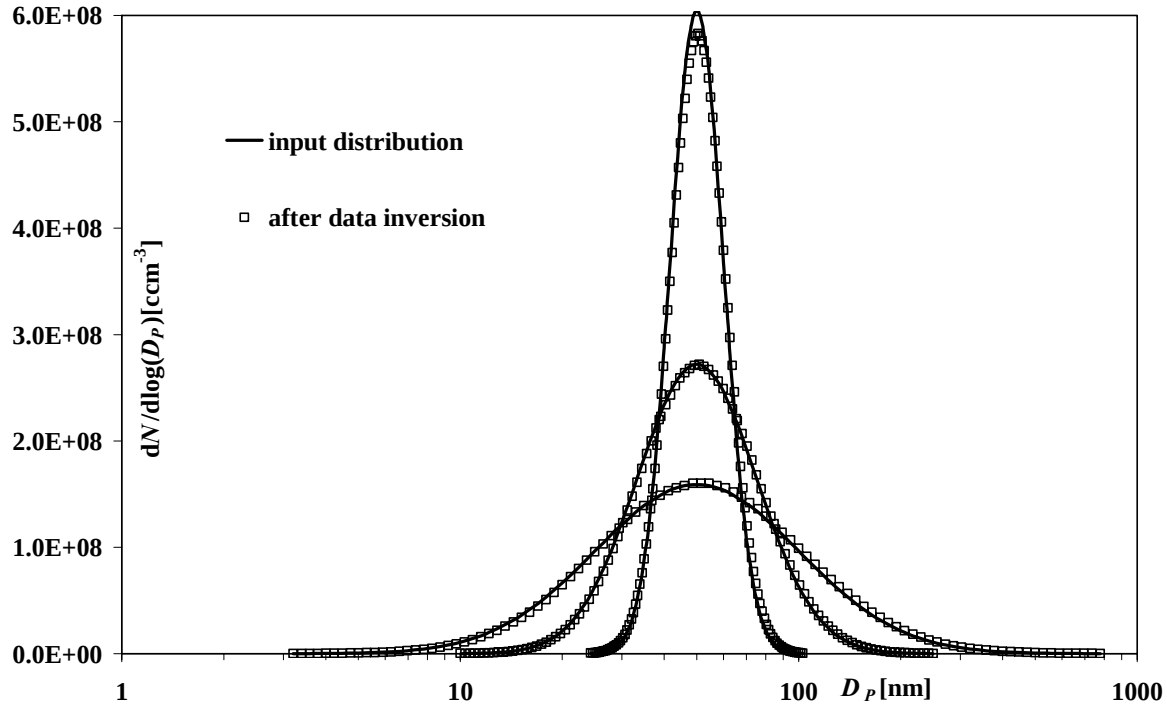

Figure 4.7.3.6: Result of simulation of thermionic charging, photonic charging and size fractionating and data inversion (rectangular dots) compared to lognormal input distribution (solid line) for σ_g=1.20, σ_g=1.50, and σ_g=2.0 (D_g=50nm, N_{proc}=1.2·10^{8}cm^{-3}, N_{SP}=10^{6}cm^{-3}, p=1013.0mbar, T_{proc}=1673.0K, 100 size channels)

As a consequence of the evaluation by the preceding simulations it can be stated that the suggested data inversion works well for lognormal size distributions with mean sizes D_g between 10nm and 200nm and geometric standard deviations σ_g from 1.2 to 2.0 when the input distribution is known.

Even for D_g>200nm the input distribution can be well restored when the result of the simulation is fitted by a lognormal distribution by a least squares method. In figure 4.7.3.7 the result of a lognormal fit by a least squares method is given for the result of data inversion for D_g=200nm, σ_g=1.50 (as in figure 4.7.3.2) and D_g=400nm, σ_g=1.50. The fit delivers D_{gf}=208.10nm and σ_{gf}=1.45 respectively D_{gf}=424.36nm and σ_{gf}=1.43, which is quiet good considering the electrometer signals (crosses in figure 4.7.3.7).

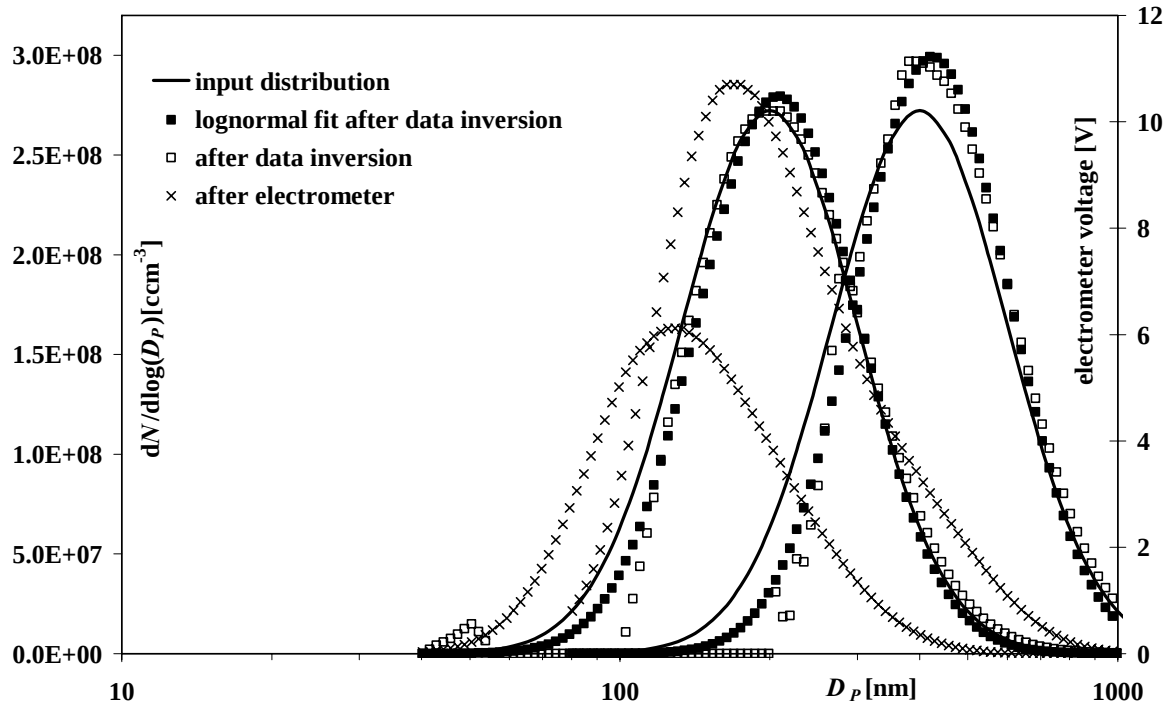

Figure 4.7.3.7: Result of simulation of thermionic charging, photonic charging and size fractionating and data inversion with a lognormal fit by a least squares method (rectangular dots) compared to lognormal input distribution (solid line) for D_g=200nm and D_g=400nm (σ_g=1.50, N_{proc}=1.2·10^{8}cm^{-3}, N_{SP}=10^{6}cm^{-3}, p=1013.0mbar, T_{proc}=1673.0K, 100 size channels). The electrometer signal with the lower magnitude is for D_g=200nm.

4.7.4 Evaluation of data inversion algorithm for unknown size distributions

The data inversion so far requires known charge fractions which are calculated for known size distributions. Since the size distribution is the very measurement quantity and therefore unknown, a different strategy has to be found to determine the size distribution out of the electrometer signal. In chapter 4.4 the influence of particle concentration on photo-charging has already been mentioned. In contrast to particle sizing methods which use β-irradiation for charging and can operate with constant size fractions $f(q)$, for photo-charging the charge of a particle depends on the whole particle ensemble. As a consequence there is no convergence when the inversion scheme is executed several times in a row since the size fraction depend on the size distribution.

Figure 4.7.4.1 and 4.7.4.2 show the simulated electrometer signal for lognormal size distributions with D_g =10nm respectively D_g =100nm and σ_g =1.5 for various concentrations N_{SP}. The DMA transfer function has been calculated with equation 4.5.3.1 for 1000mbar

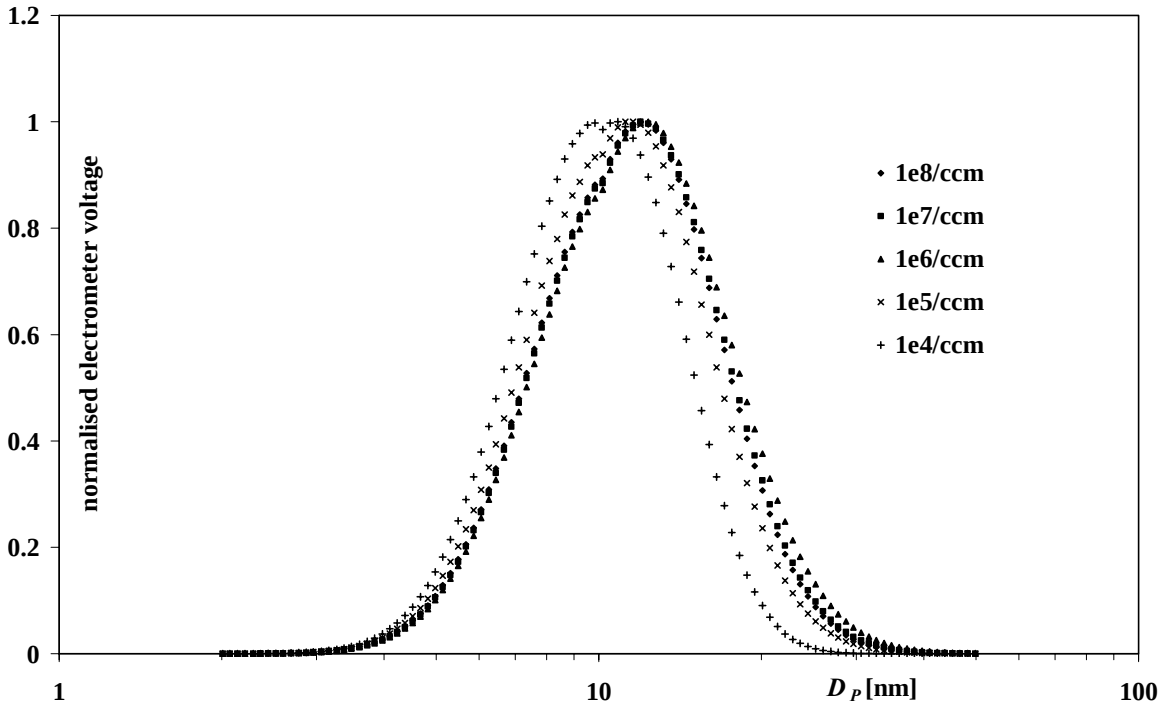

Figure 4.7.4.1: Simulated electrometer signals for lognormal size distributions with D_g=10nm and σ_g=1.5 for various concentrations N_{SP}. The signals are divided by the maxima.

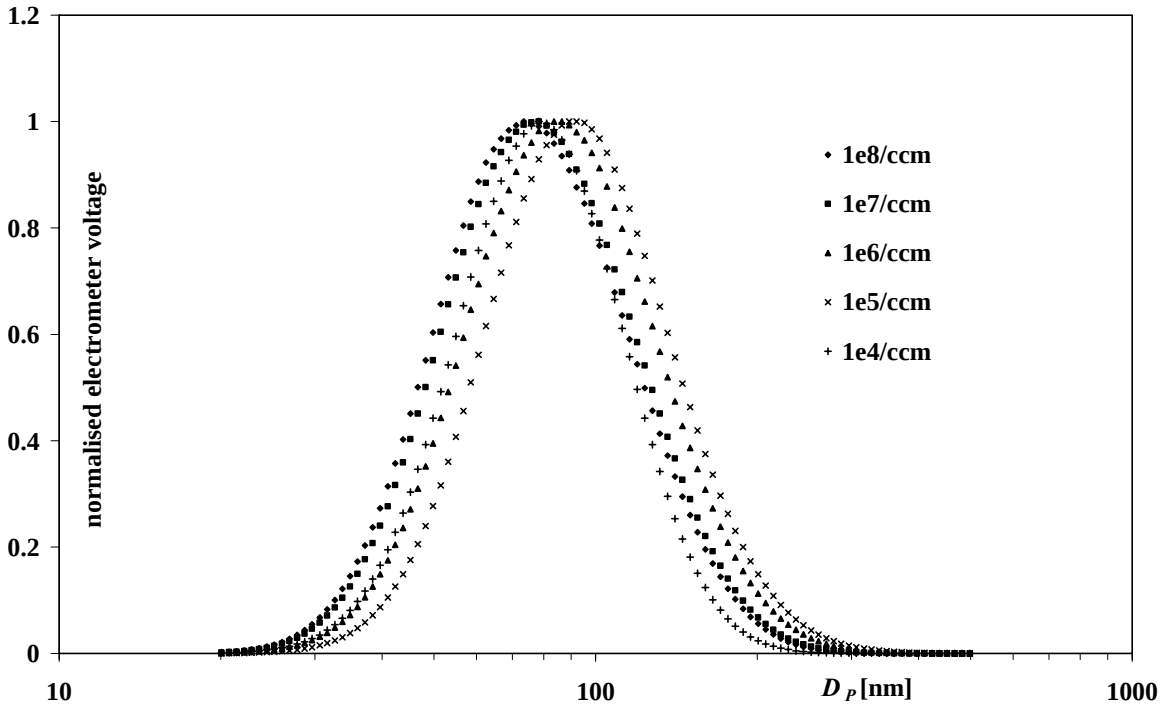

Figure 4.7.4.2: Simulated electrometer signals for lognormal size distributions with D_g=100nm and σ_g=1.5 for various concentrations N_{SP}. The signals are divided by the maxima.

The curves in figure 4.7.4.1 and 4.7.4.2 can be fitted by lognormal functions leading to geometric mean sizes D_{gfe} and standard deviations σ_{gfe} as given in table 4.7.4.1. The idea is to take the electrometer signal as an estimated size distribution for the calculation of the charge fractions.

Table 4.7.4.1: D_{gfe} and σ_{gfe} of the lognormal fit of the electrometer signals for various concentrations N_{SP} as shown in figure 4.7.4.1 and 4.7.4.2.

N_{SP}	D_g=10nm, σ_g=1.50	D_g=100nm, σ_g=1.50
10^8cm^{-3}	D_{gfe}=11.39nm, σ_{gfe}=1.463	D_{gfe}=75.67nm, σ_{gfe}=1.50
10^7cm^{-3}	D_{gfe}=11.48nm, σ_{gfe}=1.467	D_{gfe}=78.08nm, σ_{gfe}=1.50
10^6cm^{-3}	D_{gfe}=11.73nm, σ_{gfe}=1.480	D_{gfe}=85.83nm, σ_{gfe}=1.493
10^5cm^{-3}	D_{gfe}=10.87nm, σ_{gfe}=1.451	D_{gfe}=92.27nm, σ_{gfe}=1.477
10^4cm^{-3}	D_{gfe}=9.97nm, σ_{gfe}=1.412	D_{gfe}=78.51nm, σ_{gfe}=1.427

The output voltage range of the electrometer is limited to 10V. An optimum concentration would produce a peak of just 10V in order to minimize the effect of noise. In practise the dilution ratio must be adjusted that way that the electrometer voltage peak is inside a range of about 3V to 10V. For D_g=10nm, σ_g=1.50 for N_{SP}=10^7cm^{-3} the voltage peaks at 5.56V , for N_{SP}=10^8cm^{-3} it is 60.9V and far outside the electrometer voltage range. For N_{SP}=10^6cm^{-3} U_{peak}=0.43V which in practise is too low since the signals in the marginal channels are covered by noise. For D_g=10nm and σ_g=1.50 a convenient concentration is N_{SP}^0=$1.86 \cdot 10^7$cm^{-3} causing a U_{peak} of 8.94V. For D_g=20nm and σ_g=1.50 a convenient concentration is N_{SP}^0=$3.30 \cdot 10^6$cm^{-3} causing a U_{peak}=3.44V.

An estimate D_{gest} for the unknown D_g can be obtained by

$$D_{gest}[\text{nm}] = 7.53 \cdot 10^{-7} (D_{gfe}[\text{nm}])^4 - 1.69 \cdot 10^{-4} \cdot (D_{gfe}[\text{nm}])^3 + 1.63 \cdot 10^{-2} \cdot (D_{gfe}[\text{nm}])^2 + \\ + 4.91 \cdot 10^{-2} \cdot D_{gfe}[\text{nm}] + 2.88 \qquad (4.7.4.1)$$

as given in table 4.7.4.2.

Table 4.7.4.2: Lognormal fit of the electrometer signal in terms of D_{gfe} and σ_{gfe} for various input distributions for a convenient concentration N_{SP}^0.

D_g [nm]	σ_g	N_{SP}^0 [cm^{-3}]	D_{gfe} [nm]	σ_{gfe}	D_{gest} [nm]
10	1.3	$1.86 \cdot 10^7$	10.87	1.313	9.94
10	1.5	$1.86 \cdot 10^7$	11.84	1.467	10.71
10	1.8	$1.86 \cdot 10^7$	12.42	1.653	11.19
20	1.3	$3.30 \cdot 10^6$	20.75	1.298	18.73
20	1.5	$3.30 \cdot 10^6$	19.47	1.492	17.49
20	1.8	$3.30 \cdot 10^6$	22.68	1.701	20.64
50	1.3	$1.74 \cdot 10^6$	48.75	1.320	50.31
50	1.5	$1.74 \cdot 10^6$	48.88	1.484	50.47
50	1.8	$1.74 \cdot 10^6$	49.69	1.705	51.47
100	1.3	$1.71 \cdot 10^6$	87.62	1.372	102.07
100	1.5	$1.71 \cdot 10^6$	85.83	1.493	99.43
100	1.8	$1.71 \cdot 10^6$	84.38	1.663	97.31
200	1.3	$1.06 \cdot 10^6$	139.97	1.489	217.59
200	1.5	$1.06 \cdot 10^6$	135.67	1.535	203.56
200	1.8	$1.06 \cdot 10^6$	128.04	1.647	181.44
400	1.3	$1.06 \cdot 10^6$	170.70	1.776	362.07
400	1.5	$1.06 \cdot 10^6$	187.80	1.602	489.38
400	1.8	$1.06 \cdot 10^6$	170.70	1.629	362.07

N_{SP}^0 can be obtained by

$$N_{SP}^0[\text{cm}^{-3}] = \begin{cases} -1.53 \cdot 10^6 \cdot D_{gest}[\text{nm}] + 3.39 \cdot 10^7; & D_{gest} < 20\text{nm} \\ -5.20 \cdot 10^4 \cdot D_{gest}[\text{nm}] + 4.34 \cdot 10^6; & 20\text{nm} \le D_{gest} < 50\text{nm} \\ -4.53 \cdot 10^3 \cdot D_{gest}[\text{nm}] + 1.97 \cdot 10^6; & 50\text{nm} \le D_{gest} < 200\text{nm} \\ 1.06 \cdot 10^6; & 200\text{nm} \le D_{gest} \end{cases} \quad (4.7.4.2)$$

If now the charge fractions are calculated for a size distribution with D_{gest}, σ_{gfe}, and N_{SP}^0 and the data inversion is performed on the actual electrometer signal (for D_g, σ_g, and N_{SP}) it is interesting to see how a variation of D_g and σ_g of the input concentration affects the result. For 3V<U_{peak}<10V the concentration should be between $0.333 \cdot N_{SP}^0$ and $1.667 \cdot N_{SP}^0$, therefore N_{SP} has been varied between $0.333 \cdot N_{SP}^0$ and $1.667 \cdot N_{SP}^0$. Table 4.7.4.3 gives the results.

Table 4.7.4.3: Effect of a variation of the concentration N_{SP}^0 of the input distribution on the final values of D_{gdi} and σ_{gdi} after data inversion

input distribution		N_{SP}^0 [cm^{-3}]	$N_{SP}=0.333 \cdot N_{SP}^0$		$N_{SP}=N_{SP}^0$		$N_{SP}=1.667 \cdot N_{SP}^0$	
D_g[nm]	σ_g		D_{gdi} [nm]	σ_{gdi}	D_{gdi} [nm]	σ_{gdi}	D_{gdi} [nm]	σ_{gdi}
10.00	1.30	$1.86 \cdot 10^7$	10.33	1.33	10.29	1.33	10.28	1.32
10.00	1.50	$1.86 \cdot 10^7$	10.62	1.51	10.53	1.51	10.50	1.51
10.00	1.80	$1.86 \cdot 10^7$	11.18	1.77	10.97	1.75	10.92	1.75
20.00	1.30	$3.30 \cdot 10^6$	20.64	1.31	20.31	1.31	20.20	1.31
20.00	1.50	$3.30 \cdot 10^6$	20.95	1.52	20.18	1.50	19.94	1.50
20.00	1.80	$3.30 \cdot 10^6$	22.26	1.83	20.68	1.77	20.24	1.75
50.00	1.30	$1.74 \cdot 10^6$	51.83	1.30	50.57	1.31	49.98	1.31
50.00	1.50	$1.74 \cdot 10^6$	53.39	1.50	50.49	1.50	49.31	1.49
50.00	1.80	$1.74 \cdot 10^6$	56.32	1.81	50.67	1.78	48.69	1.76
100.00	1.30	$1.71 \cdot 10^6$	105.28	1.29	102.86	1.30	101.47	1.31
100.00	1.50	$1.71 \cdot 10^6$	108.03	1.48	101.90	1.49	98.90	1.50
100.00	1.80	$1.71 \cdot 10^6$	110.85	1.74	99.37	1.75	94.71	1.74
200.00	1.30	$1.06 \cdot 10^6$	218.02	1.32	215.08	1.31	213.31	1.31
200.00	1.50	$1.06 \cdot 10^6$	217.68	1.45	212.36	1.45	208.61	1.45
200.00	1.80	$1.06 \cdot 10^6$	218.96	1.60	201.65	1.61	191.73	1.63

Up to 200nm the maximum errors are ±12.6% for D_g and ±11.1% for σ_g as long as the concentration N_{SP} is between $0.333 \cdot N_{SP}^0$ and $1.667 \cdot N_{SP}^0$ as calculated by equation 4.7.4.2. For D_g>200nm the method is not suitable since variations of D_g lead only to small changes of D_{gfe}. This in principle extends the size range if the instrument because actual size distributions are projected onto electrometer signals with smaller mean sizes. The uncertainties however gravely increase for D_g>200nm. Additionally the simulation of the charging becomes very expensive since the process becomes more dynamic and the number of differential equations increases. For D_g=400nm the calculation of the charge fractions on a modern personal computer can take several hours, for D_g=1000nm several days.

As a summary it can be stated that a determination of size distributions is possible when photo charging is used and when the total number concentration is not exactly known. Assuming a lognormal distribution the following steps are necessary:

1. Lognormal fit of electrometer signal delivering D_{gfe} and σ_{gfe}.
2. Calculation of D_{gest} by equation 4.7.4.1
3. Calculation of N_{SP}^0 by equation 4.7.4.2
4. Calculation of charge fractions by simulation of the charging process for N_{SP}^0, D_{gest}, and σ_{gfe}
5. Data inversion of the electrometer signal leading to the final result in terms of D_{gdi} and σ_{gdi}.

5 Application of the system to industrial powder synthesis processes

5.1 Application to a large scale powder synthesis plant

The process for the SiO_2 powder synthesis is illustrated by figure 5.1.1.

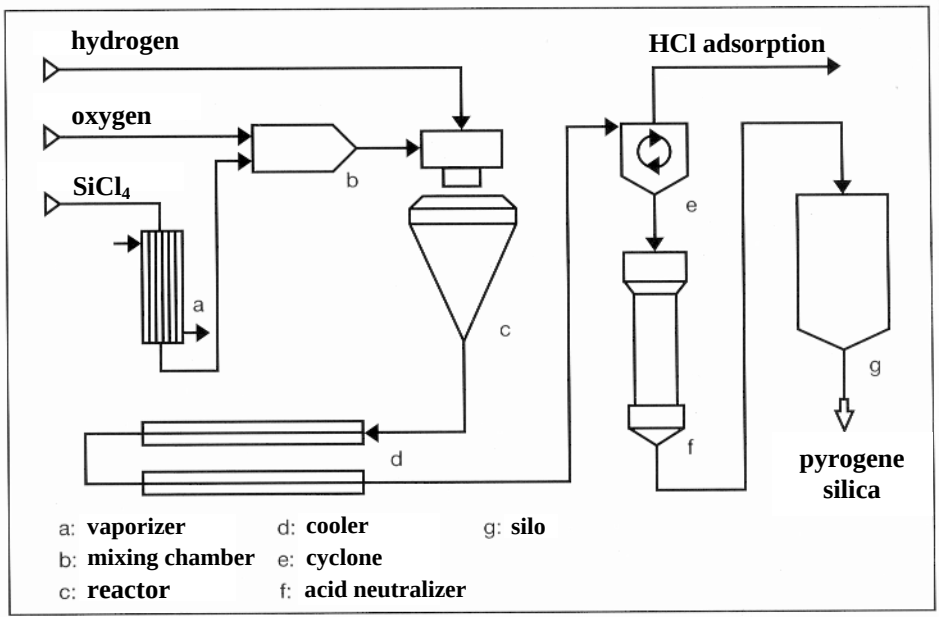

Figure 5.1.1: Silica synthesis (by courtesy of Degussa AG)

The silicon tetrachloride precursor is liquid and vaporized before mixed with oxygen and hydrogen and given into the reactor. In a first reaction water is generated by the exothermal reaction between hydrogen and oxygen. Silica and hydrochloride are generated by the endothermic reaction between water and silicon tetrachloride. The resulting temperature is about 1000°C. In order to keep the silica (and the hydrochloride) gas borne, a secondary air flow is introduced into the reactor, coaxially around the reactants. After the reaction is completed the airborne product is cooled, the hydrochloride is removed, and the particles (SiO_2 powder) are separated from the air by cyclones and filters.

Measurements of the number size distribution have been done at different locations of the process. One location was directly at the exit of the reactor, the others were further downstream the plant. Directly at the reactor the measurements could not be reproduced because the concentrations of the sampled aerosol fluctuated too much. Further downstream the process the results were reproducible. Two different SiO_2 synthesis processes have been investigated. The one generates a specific surface of $200m^2/g$, the other a specific surface of $300m^2/g$. The number of DMA size channels has been 39. The pressure was 600mbar. The results of the measurements and the data inversion are given in table 5.1.1. Table 5.1.2 gives the averaged values.

Table 5.1.1: Results of the LPDMPS measurements at the large scale powder synthesis plant

location	spec. surface [m^2/g]	D_{gfe}	σ_{gfe}	D_{gdi}	σ_{gdi}
1	200	240.76	1.40	243.39	1.20
1	200	231.26	1.45	241.23	1.20
1	200	218.18	1.49	242.09	1.21
1	200	199.60	1.44	233.63	1.19
1	300	194.69	1.57	236.54	1.20
1	300	197.63	1.45	232.03	1.19
1	300	210.23	1.48	237.74	1.20
1	300	193.24	1.50	234.45	1.19
2	200	78.40	1.60	83.46	1.49
2	200	64.06	1.95	85.43	1.62
2	200	74.69	1.69	95.37	1.53
2	200	70.97	1.72	92.54	1.53
2	300	74.35	1.53	84.27	1.52
2	300	62.33	1.57	87.05	1.49
2	300	60.49	1.93	82.24	1.61
2	300	61.00	1.95	86.10	1.58

Table 5.1.2: Results of the LPDMPS measurements at the large scale powder synthesis plant, averaged values

location	spec. surface [m^2/g]	$\overline{D_{P0fe}}$ [nm]	$\overline{\sigma_{gfe}}$	$\overline{D_{gdi}}$ [nm]	$\overline{\sigma_{gdi}}$
1	200	229.79	1.34	240.09	1.20
1	300	216.93	1.46	235.19	1.19
2	200	68.27	1.49	89.20	1.54
2	300	65.68	1.48	84.92	1.55

5.2 Comparison to offline size measurement of aerosol sampled onto filter grids for SEM

For a comparison of LPDMPS data to SEM image analysis the particles downstream the sampling probe additionally have been sampled onto micropore filters for SEM. The particles have been synthesized in a research scale furnace reactor. The SEM images are shown in figure 5.2.1. The deposition surface ratio is about 2%. The fact that particles (bright) mainly deposit around the pores (dark) of the filter suggests that particles agglomerate to a certain degree on the filter. The analysis has yielded the size distribution in figure 5.2.2. The number of sized particles has been 2627. The geometric mean size of the lognormal fit of LPDMPS data after inversion is 101.08nm (σ_g=1.302). The difference between LPDMPS and SEM is assumed to be caused by agglomeration of particles on the filter, which is the very drawback of offline size analysis. The online measurement developed in this thesis overcomes this problem.

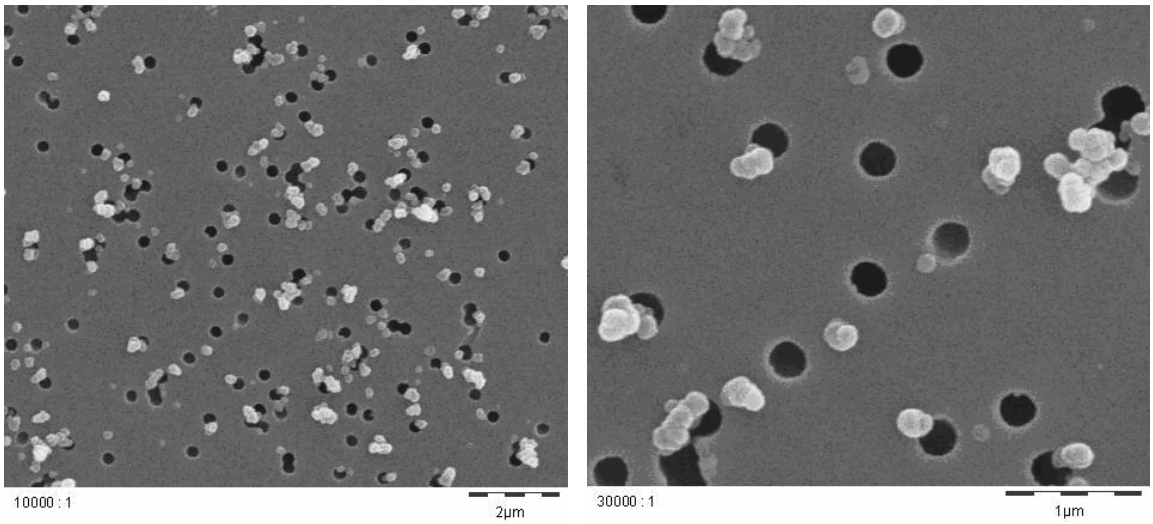

Figure 5.2.1: SEM images of SiO_2 particles (bright) deposited on a micropore filter (by courtesy of Degussa AG)

The averaged electrometer signal of seven measurements and the result of the data inversion in comparison to the result of SEM image analysis of the images in figure 5.2.1 are shown in figure 5.2.2.

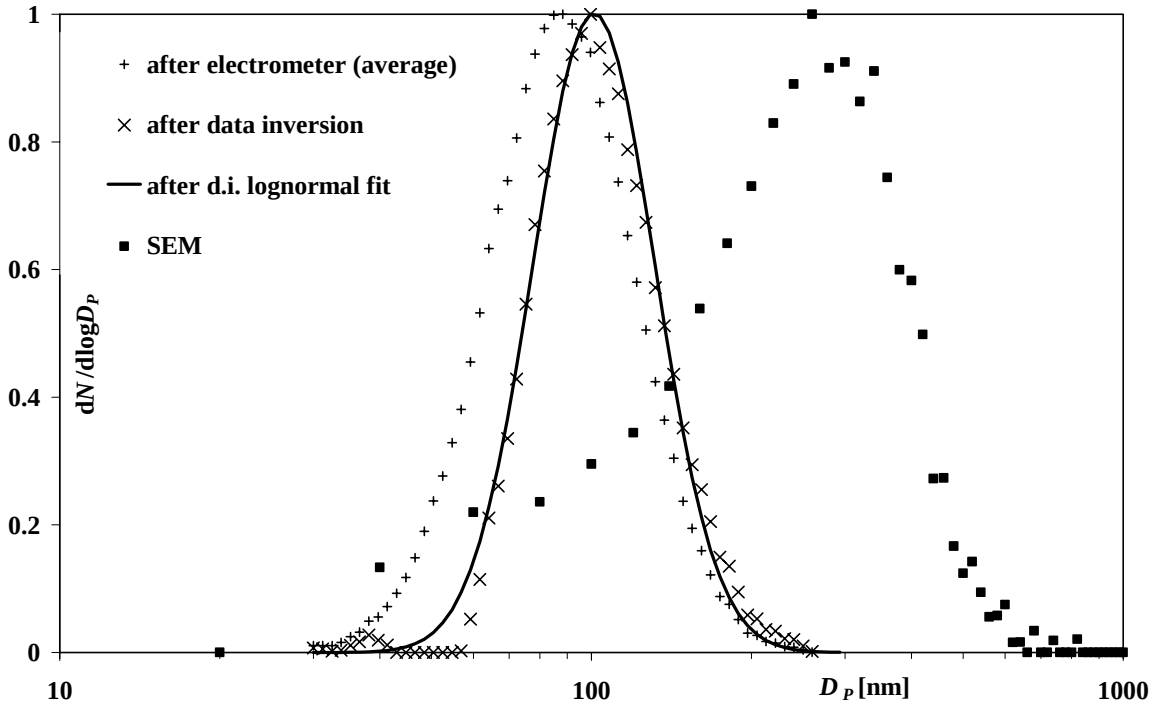

Figure 5.2.2: LPDMPS measurement result (averaged electrometer signal from seven measurements, inverted signal and lognormal fit) compared to result of SEM image analysis (all normalized to maximum)

5.3 Discussion of the measurement results

The measurements have shown that the new LPDMPS is able to provide particle number size distributions for synthesis processes for powders. It is beyond the scope of this thesis to discuss the influences of synthesis conditions on the particle size. However the influence of certain reactor parameters on the particle size could be shown. For the research plants fluctuations of the mean particle size occurred even when the plants operated with constant adjustments. These fluctuations could be traced back to a successive change of the reactors during the operation, by the deposition of particles onto the reactor walls, and a non constant dosing of the chemical components. Depending on the load, the duration of operation after disassembling – cleaning – assembling of the reactors was one to two hours. At the end of the phases of operation, the measured size distributions gravely deviated from the lognormal distribution and were not reproducible any more. The quality of measurements depended on the period the reactors had operated after cleaning and was a subjective decision. For the large scale plant measurements inside the reactor were not possible. Measurements more downstream the plant did work well. The tendency of the results agrees with theoretical expectations.

6 Conclusion and outlook

Within this thesis a measurement system has been developed and realized which allows the measurement of particle number size distributions in industrial processes for the production of nanoscaled powders. The basic principle is the differential mobility analysis. The single components, namely sampling probe, DMA, and electrometer have been newly designed in so far, as the system has to cope with subatmosheric pressures, high concentrations and HCl. The measurement system delivers the sizes of aggregates. In contrast to SEM which is widely used for nanoparticle size characterization, the method does not suffer from artefacts due to particle sampling onto filters or grids.

To the system belong a couple of sensors and actuators which are necessary to control the measurement execution and treatment of data. An interface to a personal computer has been realized. A computer program has been developed to control the measurement, enter parameters like size range, measurement time, and to display, store and process the data. A data inversion algorithm has been implemented, which converts the electrometer raw data into number size distributions. The suitability of the system to monitor the influence of reactor parameters on the size distribution has been shown by application to a research scale and large scale plants for powder synthesis.

The requirements as to pressure, particle number concentrations and the presence of HCl have been fulfilled. However unexpected difficulties impeded the application of the system. The first one was a blocking up of the sampling probe by powder. A good remedy was a permanent backward flushing in between sampling and cleaning by backward pressure pulses after a measurement. Depending on the process this cannot avoid crusts of annealed particles, which occurred at sampling from inside the reaction zone of combustion processes. Another difficulty was a fluctuation of the pressure which caused a fluctuation of the volume flow in the measurement system. This affects the DMA transfer function. Although a capillary tube was helpful, all processes showed unexpected pressure changes. Some reasons could be identified as for example a non-constant precursor dosing or the blowing-free of filters. Other reasons could only speculated about as for example the loosening of crusts of powder from the reactor walls. For future work a stronger separation of the pressure inside the measurement system and the process should be considered. The processes however do not show steady state behaviour and the particle size distribution turned out to vary gravely at certain sampling locations. The magnitude and frequency of these variations have to be investigated and a useful representation has to be discussed.

The suitability of a commercially available ultra violet irradiation unit as particle charger has been shown. This avoids the risk of radioactive contamination coming with α- or β- sources. Particle charging has been determined by numerically solving ion population balances. It has been shown that thermionic charging from the reaction plays no role, as the former charge history is completely erased. The disadvantage of photocharging is the dependency of the charging on the size distribution, the very quantity to measure. This has been revealed by numerical modelling of the charging. Efforts to find a convergent iterative scheme to

gradually approximate the actual size distribution failed. Instead the data inversion is performed with the charge fractions of an estimated distribution for which the charging is calculated. A simulation of DMA size fractionation and data inversion showed that for size distributions up to D_g=200nm the deviation of the geometric mean size is below 12.6% for the geometric standard deviation below 11.1%. If possible a radioactive source should be favoured.

Results of experimental investigations on the DMA transfer function were not according to theory e.g. no clear pressure dependency has been observed. The reason is a uncertainty of volume flows under reduced pressure. As a consequence for different pressures the DMA was operated with different sets of flows and the transfer functions were no longer comparable. The transfer function has been fitted by triangular fits of experimental data. The results showed that the volume flows were not perfectly matched since the heights of the fitting triangles exceeded 1.0. A broadening due to particle diffusion however could be observed for all pressures. Electrical breakthroughs occurred at about 17kV and restricted the maximum particle size to about 417nm which is below the postulated value of 500nm. The transfer function has been measured down to 20nm for pressures down to 200mbar. For the required size minimum of 10nm extrapolated transfer functions can be used. Simulations have demonstrated the functionality of the DMA in the range between 10nm and 400nm. The usage of only two critical orifices restricts the number of possible values for the volume flows. In order to extend the size range, several sets of critical orifices could be used which can be alternatively switched by electrical valves. The machining however is difficult since the diameters are in the micrometer range.

In order to widen the measurement range and to save time, two DMA and two electrometers could be used simultaneously. Since the plumbing of the instrument has been made of standard vacuum components, a lot of space and weight could be saved by using custom-made components. The personal computer could be replaced by a small microprocessor circuit, the monitor by a small liquid crystal display. Finally a measurement unit could be created which fulfills the standards of modern computer integrated process control.

Literature

[1] Als-Niesen, J., McMorrow, D., Elements of Modern X-ray Physics, John Wiley & Sons, Ltd. (2001)

[2] Argarwal, J. K., Sem, G. J., Continuous flow single-particle-counting condensation nucleus counter, J. Aerosol Sci., 11, p. 343 (1980)

[3] Batel, W., Einführung in die Korngrößenmesstechnik, Springer- Verlag, Berlin-Heidelberg (1960)

[4] Biswas, P., Measurement of high- concentration and high- temperature aerosols, in: Aerosol measurement: principles, techniques and applications, 2nd ed., Baron, P. and Willeke, K., (eds.), p. 705, Wiley & sons, New York (2001)

[5] Bockhorn, H., Geitlinge, H., Jungfleisch, B., Lehre, T., Schon, A., Streibel, T., Suntz, R., Progress in characterization of soot formation by optical methods, Physical Chemistry Chemical Physics, 4 (15) p. 3780 (2002)

[6] Brumberger, H., Editor, Modern Aspects of Small-Angle Scattering, Kluwer Academic Publishers (1993)

[7] Brunauer, S., Emmett, P. H., Teller, E., Adsorption of gases in multimolecular layers, J. Am. Chem. Soc., 60, p. 309 (1938)

[8] Burtscher, H., Scherrer, L., Siegmann, H.C., Schmitt-Ott, A., Federer, B. Probing aerosols by photoelectric charging. J. Aerosol Sci., 17, p. 41 (1982)

[9] Chen, D. R., Pui, D. Y. H., Mulholland, G. W., Fernandez, M., Design and testing of an aerosol/ sheath inlet for high resolution measurements with DMA, J. Aerosol Sci., 30, (8), p. 983 (1999)

[10] Cooper, D., W., Wu, J., J., The inversion matrix and error estimation in data inversion: application to diffusion battery measurements, J. Aerosol Sci., 21, (2), p. 217 (1990)

[11] Dormand, J.R., Prince, P.J., A family of embedded Runge- Kutta formulae, J. Comput. Appl. Math., 6, 19- 26 (1980)

[12] Fierz, M., Scherrer, L., Burtscher, H., Real-time measurement of aerosol size distributions with an electrical diffusion battery, J. Aerosol Sci., 33, p. 1049 (2002)

[13] Filipov, A. V., Markus, M. W., Roth, P., In situ characterization of ultrafine particles by laser-induced incandescence: sizing and particle structure determination, J. Aerosol Sci., 30, (1), p. 71 (1999)

[14] Fissan, F., Pöcher, A., Neumann, S., Boulaud, D., Pourprix, M., Analytical and empirical functions of a simplified spectromètre de mobilité electrique circulaire (SMEC) for nano particles, J. Aerosol Sci., 29, (3), p. 289 (1998)

[15] Fissan, H., Helsper, C., Thielen, H.J., Determination of particle size distributions by means of an electrostatic classifier, J. Aerosol Sci., 14, (3), p. 345 (1983)

[16] Flagan, R. C., Seinfeld, J.H., Fundamentals of air pollution engineering, Prentice Hall, New Jersey (1988)

[17] Flagan, R. C., On differential mobility analyzer resolution, Aerosol Science and Technology, 30, p. 556 (1999)

[18] Fomenko, V. S., Handbook of thermionic properties, Plenum Press Data Devision, New York (1966)

[19] Friedlander, S. K., Smoke, dust, and haze. Oxford University Press, New York (2000)

[20] Fuchs, N. A., On the stationary charge distribution on aerosol particles in a bipolar ionic atmosphere, Geofis. Pura Appl., 56, p. 185 (1963)

[21] GNU Scientific Library, Reference Manual, Edition 1.6 (2004)

[22] Gunn, R., The ratio of the positive and negative light ion conductivities within a neutral aerosol space, Journal of Colloid Science, 11, p. 661 (1956)

[23] Hasenpusch, O., Hochspannngstechnik, Franzis Verlag München (1981)

[24] Hinds, W. C., Aerosol Technology. John Wiley and Sons, New York (1982)

[25] Hoppel, W.A, Determination of the aerosol size distribution from the mobility distribution of the charged fraction of aerosols. J. Aerosol Sci., 9, p. 41 (1978)

[26] Hummes, D., Neumann, S., Fissan, H., Chen, D. R., Pui, D. Y. H., Quant, F. R., Sem, G. J., Nanometer differential mobility analyzer (Nano-DMA): experimental evaluation and performance verification, J. Aerosol Sci., 27, Suppl. 1, p. 135 (1996)

[27] Hummes, D., Stratmann, F., Neumann, S., Fissan, H., Experimental determination of the transferfunction of a differential mobility analyzer (DMA) in the nanometer size range, Part. Part. Syst. Charact., 13, p. 327 (1996)

[28] Hyeon-Lee, J., Beaucage, G., Pratsinis, S. E., Vemury, S., Fractal analysis of flamesynthesized nanostructured silica and titania powders using small-angle X-ray scattering, Langmuir 14 (20) 5751-5756 (1998)

[29] Ibach, H., Lüth, H., Solid state physics, 2. edition, Springer, Berlin (1996)

[30] ICH8500 datasheet, Intersil Corporation

[31] ISO 13321 Particle size analysis - Photon correlation spectroscopy (1996)

[32] Kandlikar, M., Ramachandran, G., Inverse methods for analysing aerosol spectrometer measurements: a critical review, J. Aerosol Sci., 30, p. 413 (1999)

[33] Karlsson, M. N. A., Martinsson, B., Methods to measure and predict the transfer function size dependence of individual DMAs, J. Aerosol Sci., 34, p. 603 (2003)

[34] Keady, P. B., Quant, F. R., Sem, G. J., Automated differential mobility particle sizer, Proceedings for the 1st International Aerosol Conference, p. 71 (1984)

[35] Keskinen, J., Pietarinen, K., Lehtimäki, M., Electrical low pressure impactor, J. Aerosol Sci., 23 S353-369 (1992)

[36] Knutson, E. O., Whitby, K. T., Aerosol classification by electric mobility: Apparatus, theory, and applications, J. Aerosol Sci., 6, p. 443 (1975)

[37] Kodas, T.T., Hampden-Smith, M.J., Aerosol processing of materials, Wiley-VCH, New York (1999)

[38] Kousaka, Y., Okuyma, K., Adachi, M., Determination of particle size distribution of ultra-fine aerosols using a differential mobility analyzer, Aerosol Science and Technology, 4, p. 209 (1985)

[39] Köylü, Ü. Ö., McEnally, C. S., Rosner, D. E., Pfefferle, L. D., Simultaneous measurements of soot volume fraction and particle size / microstructure in flames using a thermophoretic sampling technique, Combustion and Flame, 110, p. 494 (1997)

[40] Kulkarni, P., Namiki, N., Otani, Y., Biswas, P., Charging of particles in unipolar coronas irradiated by in-situ soft x-rays: enhancement of capture efficiency of ultrafine particles, J. Aerosol Sci., 33, p. 1279 (2002)

[41] Lesniec, D., Elliott, L., Ingham, D. B., A numerical analysis of the data inversion of particle sizing instruments, J. Aerosol Sci., 27, (7), p. 1063 (1996)

[42] Lesniewski, T. K., Koch, W., Production of rounded Ti- and Al- hydroxide particles in a turbulent jet by coagulation-controlled growth followed by rapid coalescence, J. Aerosol Sci., 29, (1), p. 81 (1998)

[43] Lindsay, S. M., Hemski, J. W., Look, D. C., Electron beam modification of GaAs surface potential: Measurement of Richardson constant, J. Appl. Phys., 74 (3) p. 1890 (1993)

[44] Liu, B. Y. H. Pui, D. Y. H., On the performance of the electrical aerosol analyzer, J. Aerosol Sci., 6, p. 249 (1975)

[45] Liu, B. Y. H., Pui, D. Y. H., Equilibrium charge distribution, Journal of Colloid Interface Science, 49, p. 305 (1974)

[46] Maisels, A., Jordan, F., Fissan, F. , Dynamics of the aerosol particle photocharging process. J. Appl. Phys., 91, p. 3377 (2002)

[47] Maisels, A., Jordan, Fissan, F., On the effect of charge recombination on the aerosol charge distribution in photocharging systems, J. Aerosol Sci., 34, p. 117 (2003)

[48] Matter excimer radiator type 990810, manual, Matter Engineering AG, Switzerland

[49] McClelland, J. A., On the conductivity of the hot gases from flames, Phil. Mag., 46, p. 29 (1898)

[50] Michael, G., Ferch, H., Grundlagen von Aerosil, Schriftenreihe Pigmente, Nummer 11, Degussa AG (1998)

[51] Millikan, R. A., The isolation of an ion, a precision measurement of its charge, and the correction of Stoke's law, Phys. Rev. Lett., 32, p. 349 (1911)

[52] Model 3068 aerosol electrometer, manual, TSI inc., St. Paul, MN, USA (2003)

[53] Mölter, L., Keßler, P.: Grundlagen der Partikelgrößen- und Partikelanzahlbestimmung in der Außenluft mit zählenden Messverfahren, Gefahrstoffe-Reinhaltung der Luft, Heft 7/8, S. 319-323 (2004)

[54] Mölter, L., Keßler, P.: Partikelgrößen- und Partikelanzahlbestimmung in der Außenluft mit einem neuen optischen Aerosolspektrometer, Gefahrstoffe-Reinhaltung der Luft, Heft 10, S. 439-447 (2004)

[55] Müller, E., Oestreich, C. (ed.), Handling of highly dispersed powders, Schwerpunktprogramm der deutschen Forschungsgemeinschaft (DFG) (1998- 2004), Shaker Verlag, Aachen (2004)

[56] Müschenborn, P., Otten, F., Neumann, S., Trampe, A. Fissan, H., Horn, H. G., Development of a differential mobility particle sizer for atmospheric aerosols, Environmental Science and Pollution Research , special issue, 4, p. 100 (2002)

[57] Nolan, P. J., The equilibrium of ionization in the atmosphere and nuclear combination coefficients, J. Atmos. Terr. Phys., 9, p. 295 (1956)

[58] OPA128 datasheet, Burr Brown Corporation

[59] Pecora, R., editor, Dynamic Light Scattering: Applications of Photon Correlation Spectroscopy, Plenum Press, New York (1985)

[60] Prince, P.J.,Dormand, J.R., High -order embedded Runge- Kutta- Nystrom formulae, J. Comput. Appl. Math, 7, 67, 423- 430 (1980)

[61] Rosell-Llompart, J., Loscertales, I. G., Bingham, D., de la Mora, F., sizing nanoparticles and ions with a short differential mobility analyzer, J. Aerosol Sci., 27, (5), p. 695 (1996)

[62] Roth, P., Hospital, A., Design and Test of a Particle Mass Spectrometer (PMS), J.Aerosol Sci., 25 (1), 61-73 (1994)

[63] Scheibel, H. G., Porstendörfer, J., Generation of monodisperse Ag- and NaCl- aerosols with particle diameters between 2 and 300nm, J. Aerosol Sci., 27, p. 136 (1983)

[64] Seifart, M., Analoge Schaltungen, Verlag Technik GmbH, Berlin (1994)

[65] Seto, T., Nakamoto, T., Okuyama, K., Adachi, M., Kuga, Y., Takeuchi, K., size distribution measurement of nanometer-sized aerosol particles using DMA under low-pressure conditions, J. Aerosol Sci., 28, (2), p. 193 (1997)

[66] Stöcker, H., Taschenbuch der Physik, Verlag Harri Deutsch, Thun und Frankfurt am Main (1998)

[67] Stolzenburg, M. R., An ultrafine aerosol size measurement system, PhD thesis, University of Minnesota (1988)

[68] Stratmann, F., Kauffeld, T., Hummes, D., Fissan, H., Differential mobility analysis: A theoretical study, Aerosol Science and Technology, 26, p. 368 (1997)

[69] Sze, S. M., Physics of semiconductor devices, 2. edition, John Wiley and sons, New York (1981)

[70] Talukdar, S. S., Swihart, M. T., An improved data inversion program for obtaining areosol size distributions from scanning mobility analyzer data. Aerosol Science and Technology, 37, p. 145 (2003)

[71] Tammet, H., Mirme, A., Tamm, E., Electrical aerosol spectrometer of Tartu University, J. Aerosol Sci., 29 Suppl.1, S427-S428 (1998)

[72] Tietze, U., Schenk, C., Halbleiterschaltungstechnik, Springer Verlag Berlin (1999)

[73] Tikhonov, A. N., Arsenin, V. Y., Solutions of ill-posed problems, W. H. Winston, Washington, DC (1977)

[74] Tishkovets, V.P., Petrova, E.V., Jockers, K., Optical properties of aggregate particles comparable in size to the wavelength, Journal of Quantitative Spectroscopy & Radiative Transfer, 86, (3), p. 241 (2004)

[75] Twomey, S., Comparison of constrained linear inversion and an iterative nonlinear algorithm applied to the indirect estimation of particle size distributions, J. of Comput. Phys., 18, p. 188 (1975)

[76] Ultra Filter type H, specifications, Mine Safety Appliances, Pittsburg, USA (1970)

[77] VDI-Norm 53206, Blatt 1, Teilchengrößenanalyse, Grundbegriffe (1972)

[78] von Ardenne, M., Tabellen zur angewandten Physik, VEB Deutscher Verlag der Wissenschaften, Berlin (1962)

[79] Wang, S. C., Flagan, R. C., Scanning electrical mobility spectrometer, Aerosol science and technology, 13, p. 230 (1990)

[80] Wiedensohler, A., Die bipolare Diffusionsaufladung in chemisch trägen Reinstgasen. PhD thesis, University Duisburg (1989)

[81] Wiedensohler, A., Lütkemeier, E., Feldpausch, M., Helsper, C, Investigation of the bipolar charge distribution at various gas conditions, J. Aerosol Sci., 17, p. 41 (1986)

[82] Winklmayr, W., Reischl, G. P., Lindner, A.O., Berner, A, A new electromobility spectrometer for the measurement of aerosol size distributions in the range from 1 to 1000nm, J. Aerosol Sci., 22, p. 289 (1991)

[83] Wolfenbarger, J. K., Seinfeld, J. H., Inversion of aerosol size distribution data. J. Aerosol Sci., 21, p. 227 (1990)

[84] Wood, M. D., Classical size dependence of the work function of small metallic spheres, Phys. Rev. Lett., 46, p. 749 (1981)

[85] Wutz, M., Adam, H., Walcher, W., Theorie und Praxis der Vakuumtechnik, Vieweg Braunschweig, Wiesbaden (1986)

[86] Zhang, S. H., Akutsu, Y., Russell, L. M., Flagan, R. C., Seinfeld, J. H., Radial differential mobility analyzer, Aerosol Science and Technology, 23, p. 357 (1995)

List of symbols

A	surface area
A_0	idle running amplification of an operational amplifier
A_{CO}	cross section of a critical orifice
A_{SS}	specific surface area
B	mechanical particle mobility
C	electrical capacity
C_C	Cunningham slip correction
C_m	chemical compound
D	diffusion coefficient
$\vec{D}$	electrical displacement vector
D_h	hydraulic diameter
D_P	particle size (diameter)
D_g	geometric mean particle size of a number size distribution
$D_{g\mathrm{est}}$	estimated geometric mean particle size
$D_{g\mathrm{di}}$	geometric mean particle size determined by data inversion
$D_{g\mathrm{f}}$	geometric mean particle size of lognormal fit
$D_{g\mathrm{fe}}$	geometric mean of lognormal fit of the electrometer signal
$\overline{D_{g\mathrm{fe}}}$	arithmetic mean of $D_{g\mathrm{fe}}$
D_i	ion diffusion coefficient
$D_{P,k}$	mean particle size of a size channel k
D_{Pl}	lower limit of the particle size range
$D_{P\,u}$	upper limit of the particle size range
D_P*	midpoint particle size corresponding to Z_P*
D_{SP}	dilution ratio of the sampling probe
E	electrical field strength
F_C	Coulomb force
F_D	drag force
I	electronic current, light intensity
J	particle flux
K_A	coagulation coefficient
K_c	material constant for the calculation of the combination coefficient
$K_k(Dp)$	kernel function for the kth channel
Kn	Knudsen number
Kn_i	Knudsen number for ions
$K(l)$	dielectric correction factor
M_{mol}	mole mass

M_j	jth moment of number size distribution
N	particle number concentration
N_k	particle number concentration in the size channel k
N_{proc}	particle number concentration inside the reactor
N_{SP}	total particle number concentration downstream of the sampling probe
$N_{\mathrm{SP}}{}^{0}$	convenient total particle number concentration for the electrometer with respect to the electrometer deflection
P	fraction of particles which pass a device e.g. pipe
Pe	Peclet number
Q	electrical charge
R	electrical resistance
R^*	effective Richardson constant
R_1	DMA radius of outlet slit
R_2	DMA radius of inlet slit
R_{gas}	general gas constant
R_k	instrument response for the kth channel
R_P	particle radius
R_{theor}	Richardson constant for free electrons
S	Sutherland constant
S_{elec}	electrometer sensitivity
T	temperature
T_R	temperature inside the reactor
T_S	temperature after sampling
U	voltage
U_{elec}	electrometer output voltage
U_{peak}	maximum of the electrometer output voltage
V	volume
$\dot{V}_a$	DMA aerosol volume flow
$\dot{V}_c$	DMA clean gas volume flow
$\dot{V}_e$	DMA excess gas volume flow
$\dot{V}_s$	DMA sample volume flow
Z	electrical impedance
Z_P	electrical mobility
Z_{Pl}	lower limit of the mobility range
Z_{Pu}	upper limit of the mobility range
Z_P*	electrical midpoint mobility
b	distance between DMA electrodes
c_0	vacuum light velocity

d_{co}	diameter of a critical orifice
e	elementary charge
$f(D_P,q,t)$	charge fraction
h	Planck constant
j	electronic current area density
k	index of size channels
k_B	Boltzmann constant
m	number of size channels
$\dot{m}_c$	critical mass flow
m_e^*	effective electron mass
m_{e0}	electron mass
n_i	number concentrations of ions
n_k	number of particles in the channel k
p	pressure
p_c	critical pressure
q	number of elementary charges
q_0	mean number of elementary charges
rH	relative humidity
s_{co}	geometric correction factor of a critical orifice
t	time
v	velocity
v_g	gas velocity
$\overline{v}_i$	mean thermal ion velocity
v_u	voltage gain
v_s	sonic speed
Δ_i	diffusional ion losses
Δ_{rH}	relative shift of particle size due to relative humidity
ϕ	electrical potential
Φ_{photon}	photon energy
$\Phi^{q\to q+1}$	work function for a spherical particle
Φ_∞	work function for a plane surface
Ω	probability of a particle to pass the DMA
$\Psi(Dp,q)$	particle detector response
α_{D_P}	height of DMA transfer function with respect to particle size
α_{Z_P}	height of DMA transfer function with respect to electrical mobility
α_{coll}	collision probability

$\alpha_{q,R_P,C_m}^{q\to q+1}$	ionisation coefficient for the photo charging
β_{D_P}	half width of DMA transfer function with respect to particle size
β_{Z_P}	half width of DMA transfer function with respect to electrical mobility
$\beta_{q,R_P,C_m}^{q\to q-1}$	recombination coefficient for diffusion charging
δ	radius of the absorbing sphere
ε_0	vacuum permittivity
ε_k	error in the mobility channel k
ϕ	electrical potential
η	dynamic viscosity
η_{DMA}	DMA transmission efficiency
φ_1	flow of dilution 1 of the sampling probe
φ_2	flow of dilution 2 of the sampling probe
φ_{co}	volume flow of a critical orifice
φ_s	flow into the sampling probe
φ_{th}	threshold for φ_1 under which no particles are sampled
κ	adiabatic coefficient
λ	mean free path of gas molecules
λ_c	critical wavelength for photo ionisation
λ_i	mean free path of gas ions
λ_P	light wavelength
ν	frequency of the light
ρ	space charge density
ρ_{gas}	gas density
σ_g	geometric standard deviation
$\sigma_{g\mathrm{di}}$	geometric standard deviation determined by data inversion
$\sigma_{g\mathrm{f}}$	geometric standard deviation of a lognormal fit
$\sigma_{g\mathrm{fe}}$	geometric standard deviation of a lognormal fit of the electrometer signal
$\overline{\sigma_{\mathrm{gfe}}}$	arithmetic mean of $\sigma_{g\mathrm{fe}}$
σ_q	geometric standard deviation of the charge q
$\upsilon_{q,R_P,C_m}^{q\to q+1}$	combination coefficient for thermal charging

Index of figures

Index of tables

A1 Functional scheme of the LPDMPS

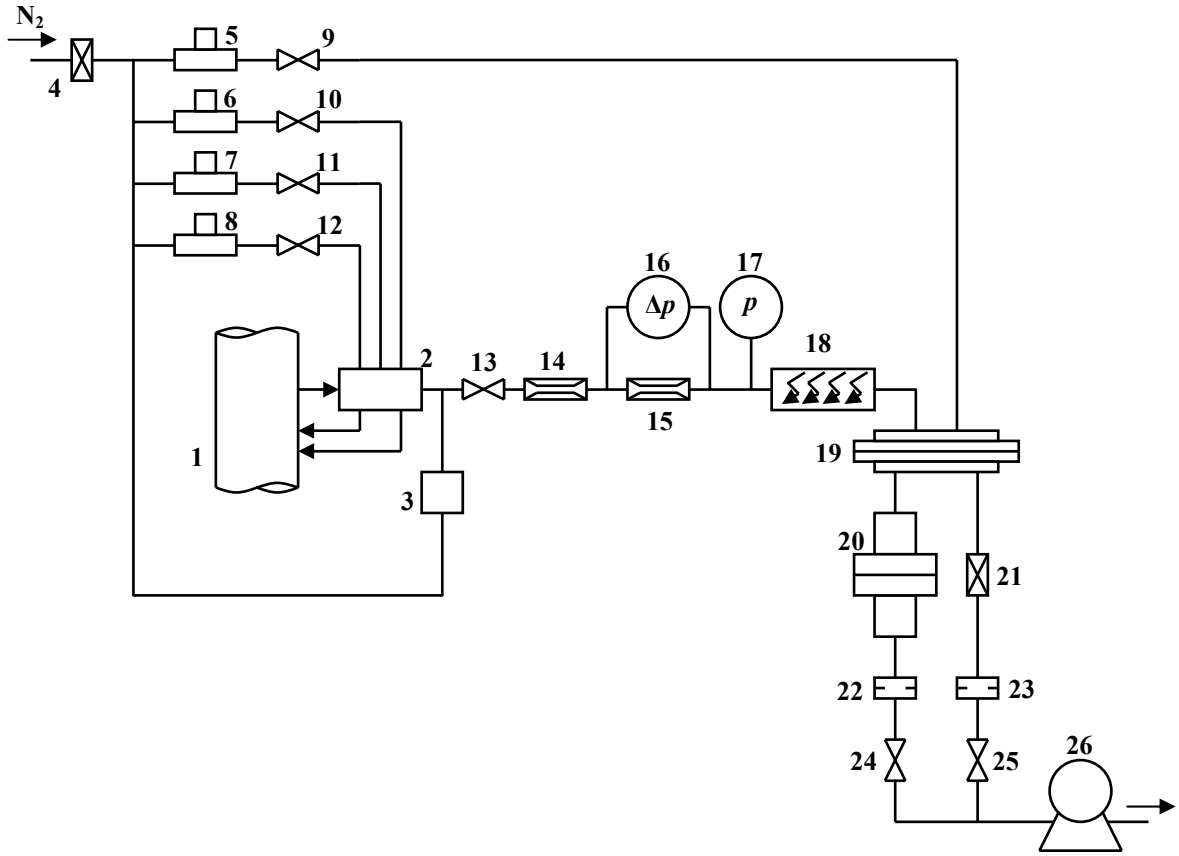

Figure A1.1: Functional scheme of the LPDMPS

Explanation:

1	process
2	probe
3	magnetic valve for the flushing of the probe with nitrogen
4	filter and pressure control
5	mass flow controller for the DMA clean gas
6	mass flow controller for dilution 1
7	mass flow controller for dilution 2
8	mass flow controller for dilution 3
9- 12	valves to protect the mass flow controllers from HCl
13	valve to cut the LPDMPS from the process
14	capillary tube for the equalization of the pressure
15	flow resistance for volume flow measurement in connection with 16

16 differential pressure gauge
17 absolute pressure gauge
18 ultra violet irradiation unit
19 DMA
20 electrometer
21 filter
22 critical orifice for the DMA sample volume flow
23 critical orifice for the DMA excess volume flow
24, 25 valves
26 vacuum pump

A2 Schematics of the sampling probe

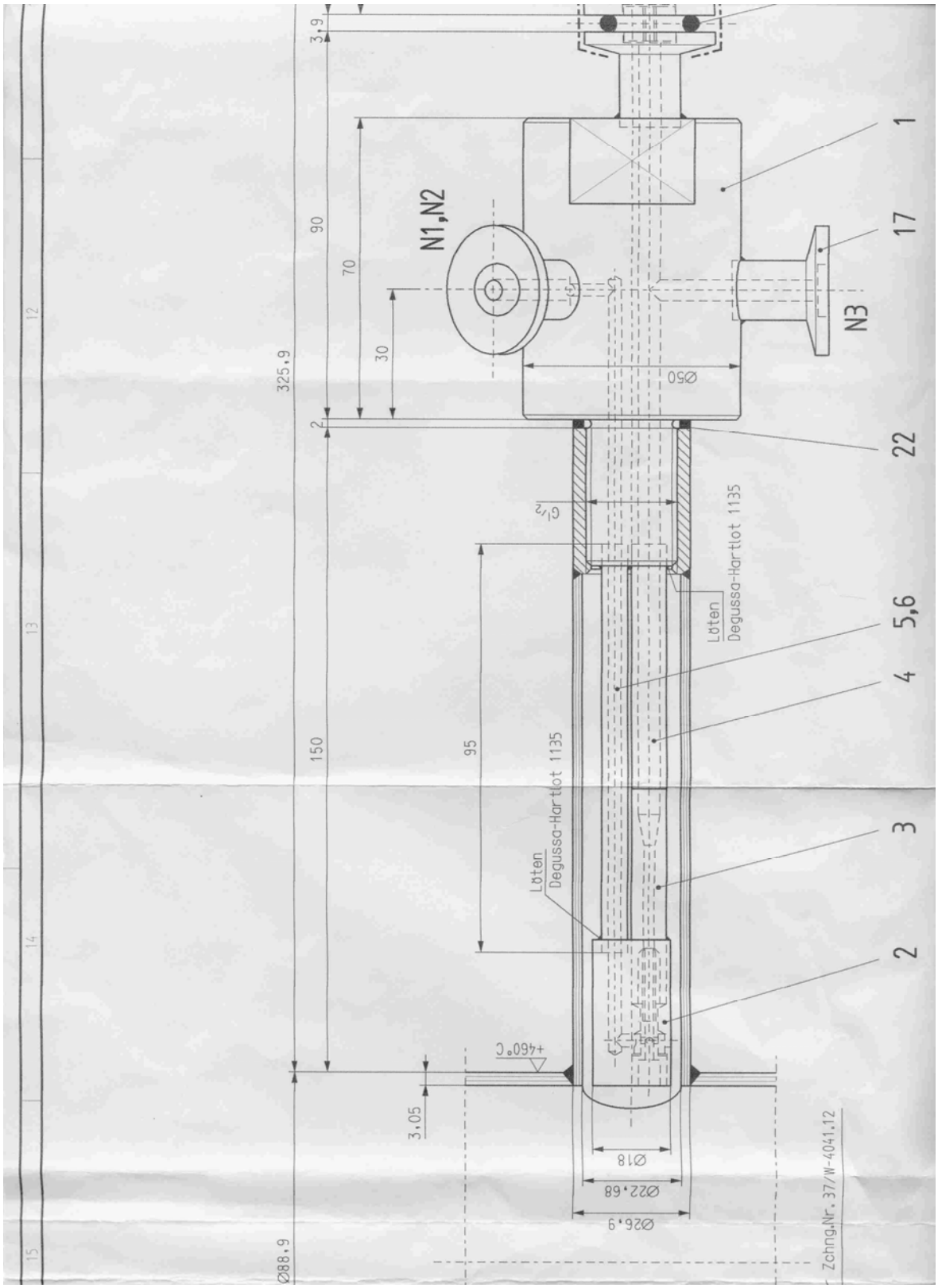

Figure A2.1: Sampling probe screwed into a flange at the reactor

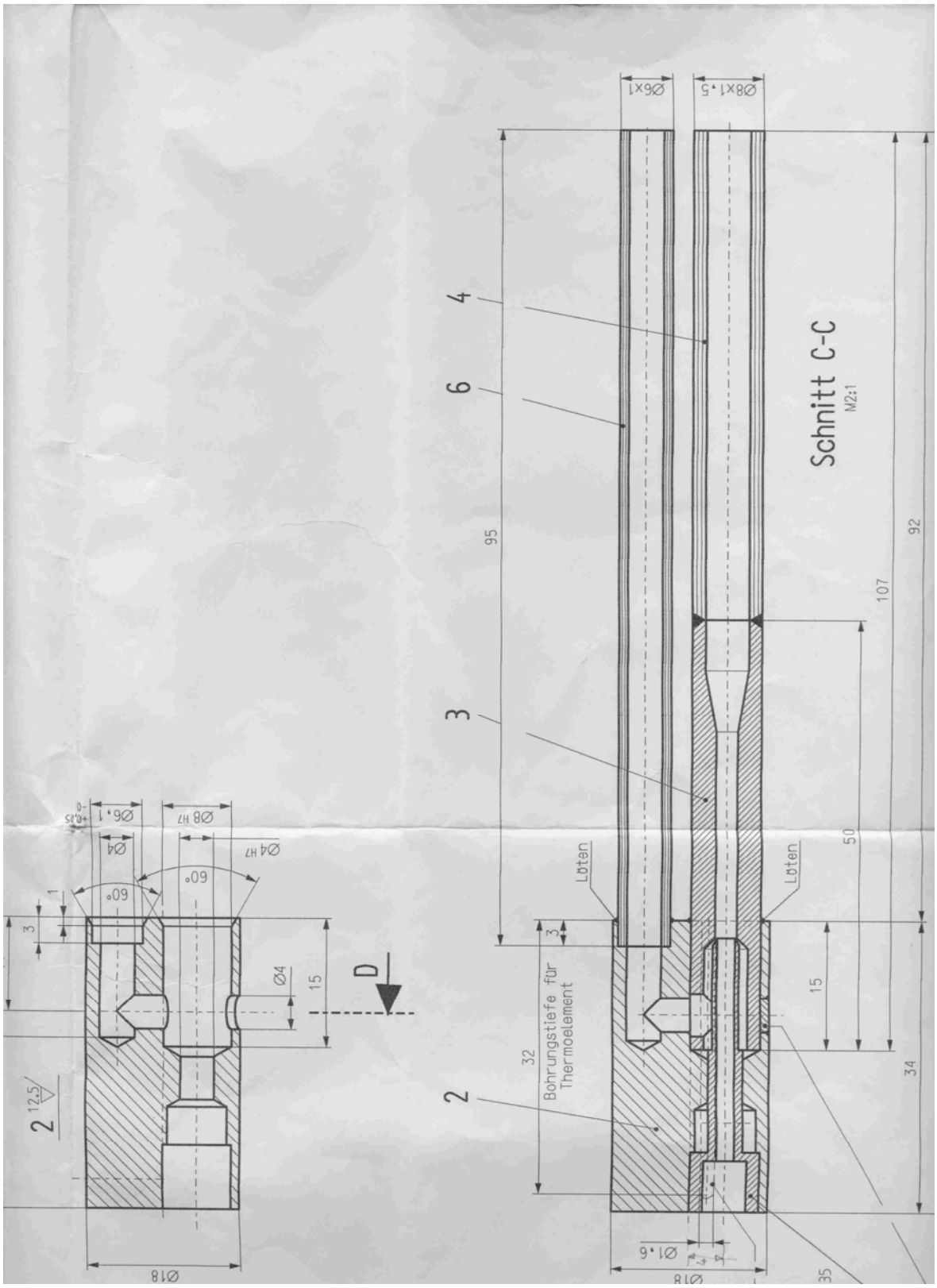

Figure A2.2: Sampling probe, detail 1

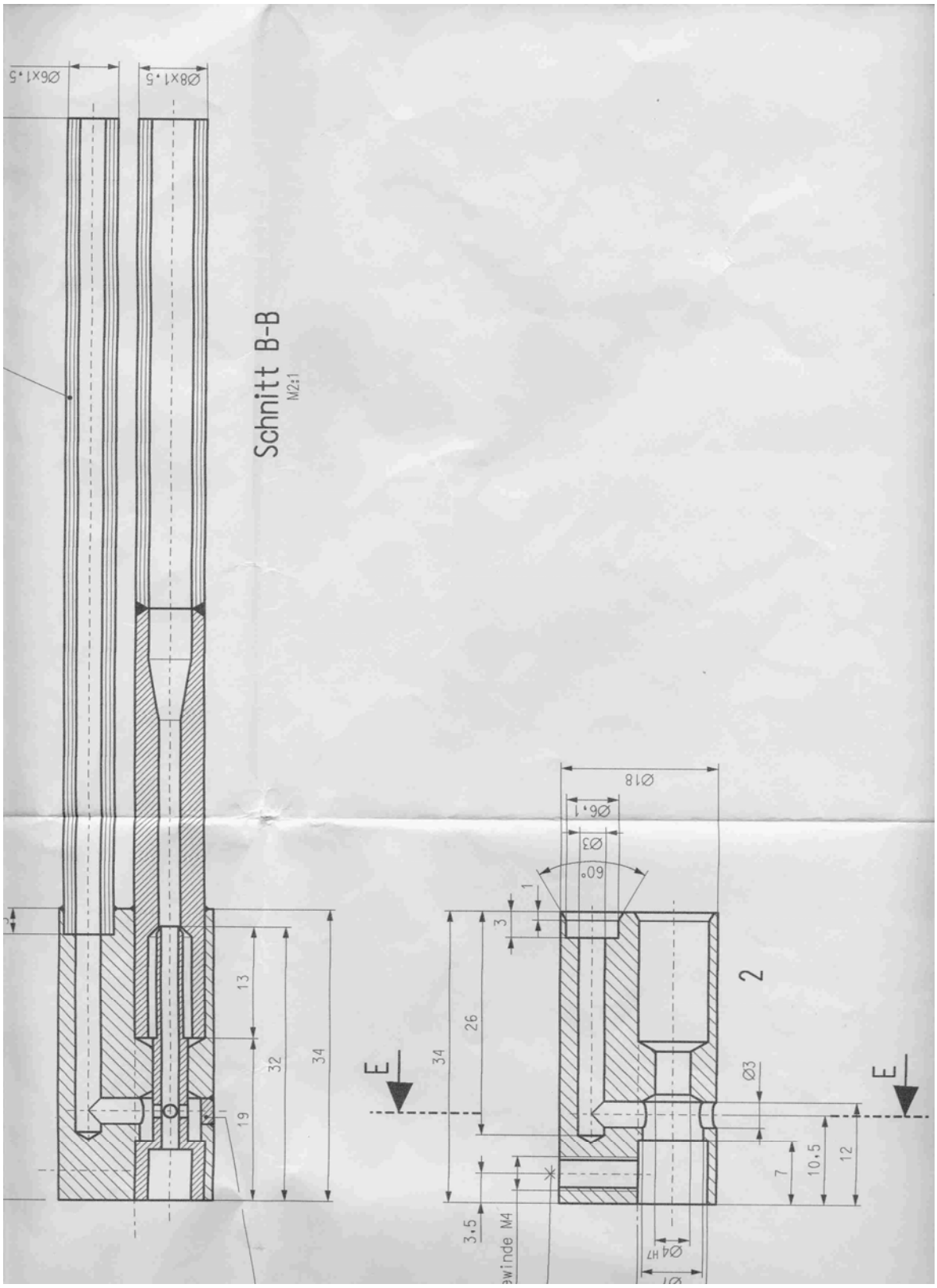

Figure A2.3: Sampling probe, detail 2

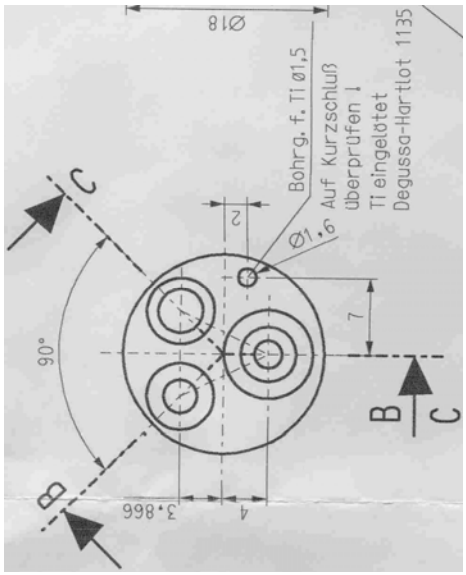

Figure A2.4: Sampling probe, detail 3

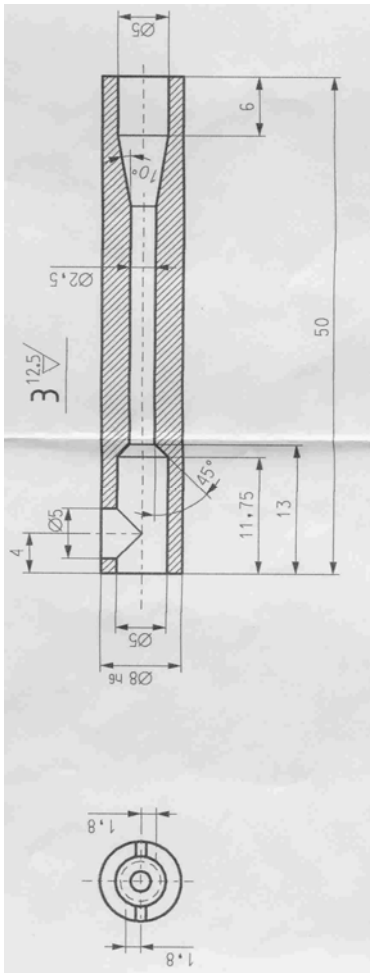

Figure A2.5: Sampling probe, detail 4

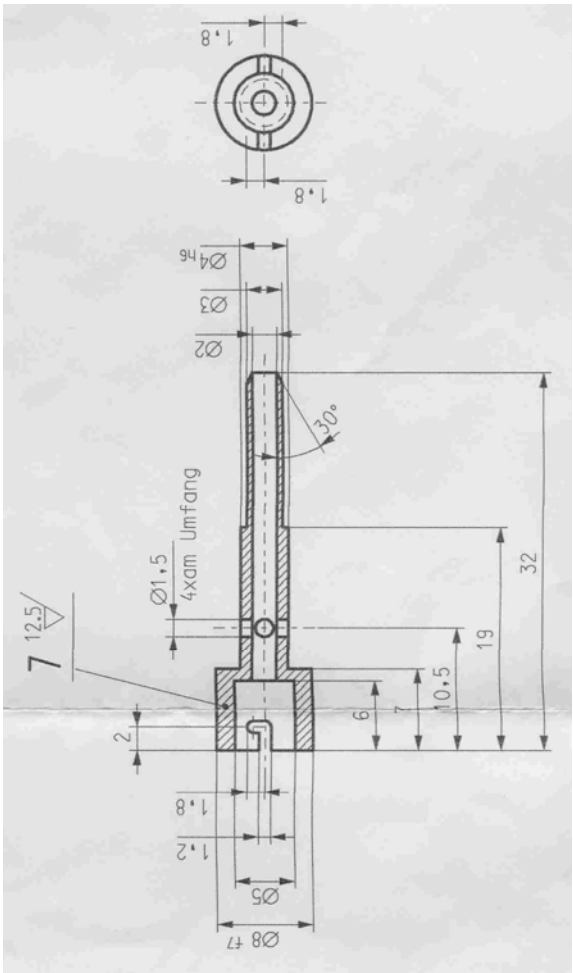

Figure A2.6: Sampling probe, detail 5

A3 Schematics of the LPDMA

Figures A3.1 to A3.3 show the new low pressure DMA, its single parts and major dimensions.

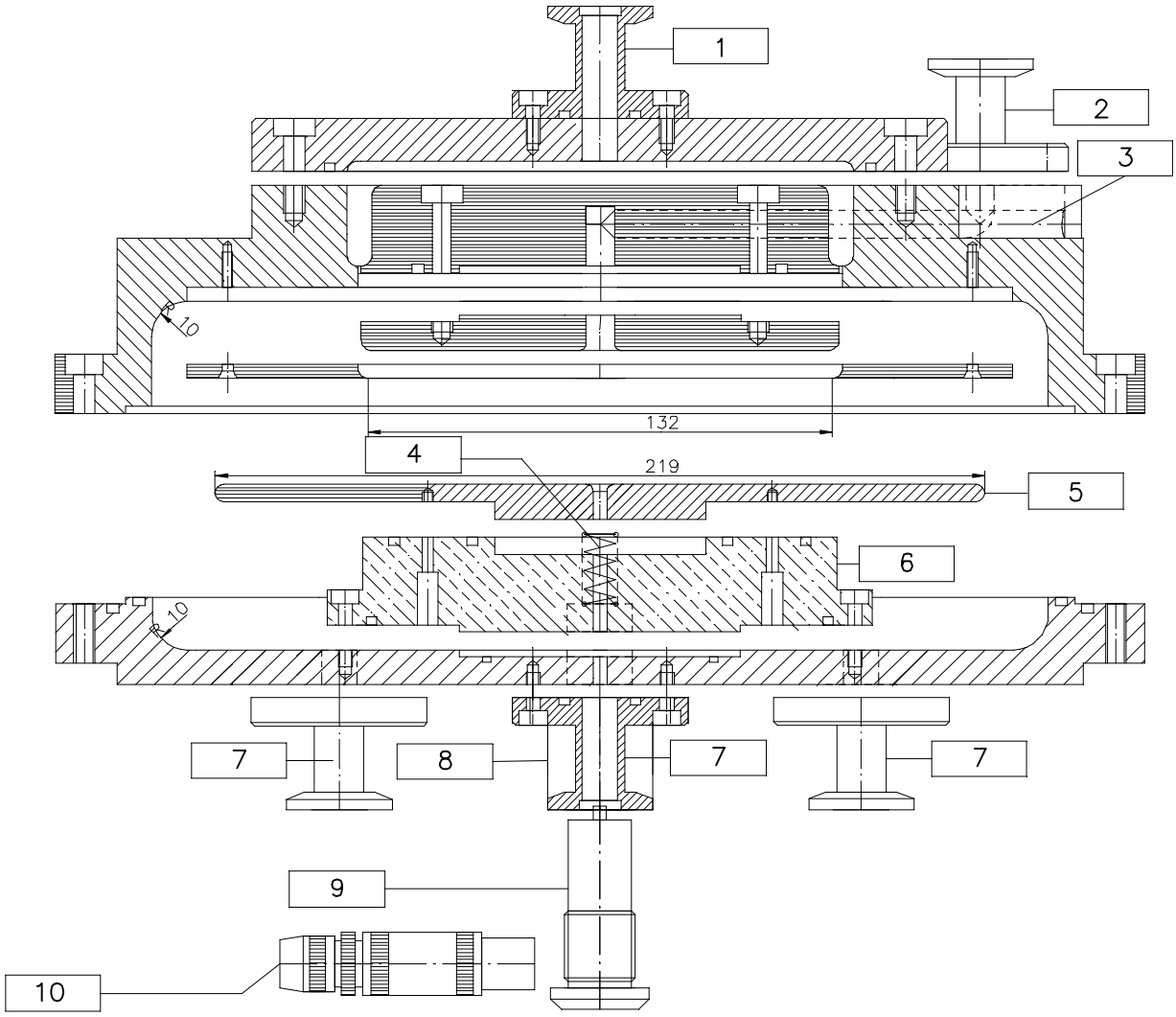

1: flange for aerosol in, 2: flange for excess gas out, 3: drilling to the centre for excess gas, 4: spring for electrical connection to the electrode: 5: electrode, 6: Teflon isolator, 7: flanges for clean gas (4x), 8: flange for electrical connector, 9: vacuum tight electrical connector, 10: plug

Figure A3.1: Disassembled parts of the new low pressure DMA

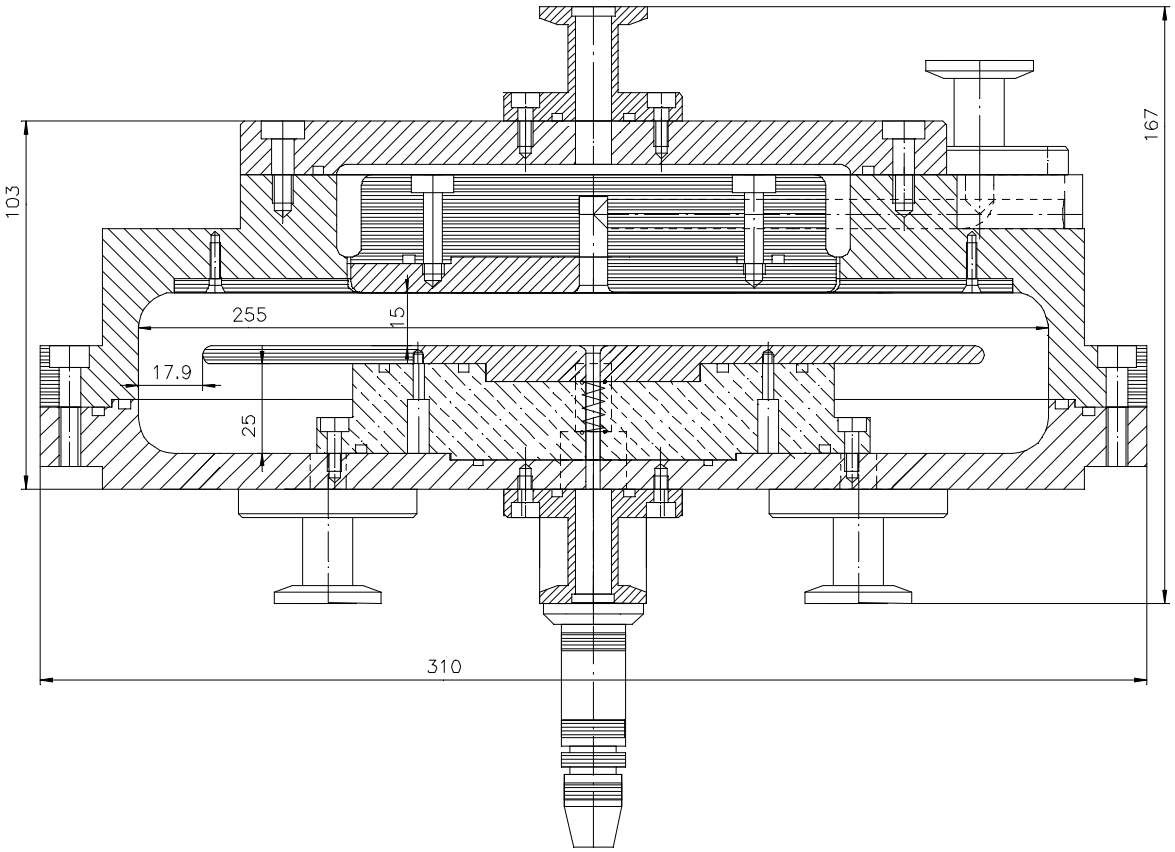

Figure A3.2: Assembled parts of the new low pressure DMA

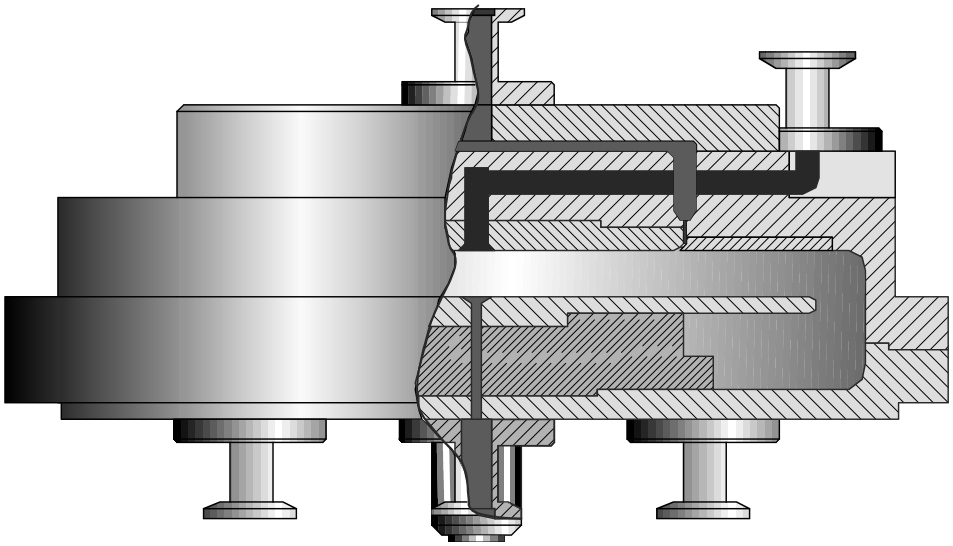

Figure A3.3: Intersectional view of the new low pressure DMA

A4 Schematic of the electrometer housing

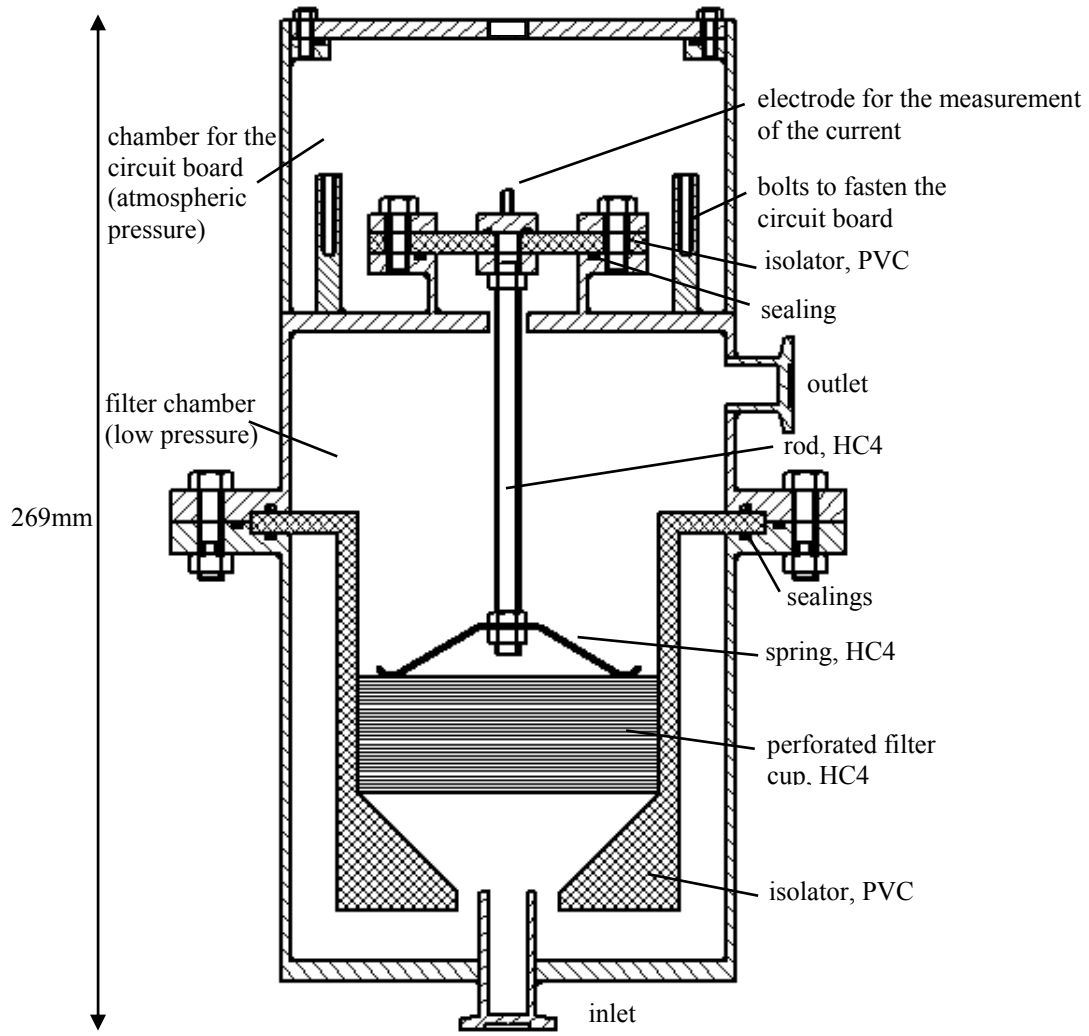

Figure A4.1: The housing of the new electrometer (crossectional view)

A5 Block diagram of the electrical hardware

The electrical components of the new LPDMPS and the signal lines to the personal computer are shown in a block diagram in figure A5.1.

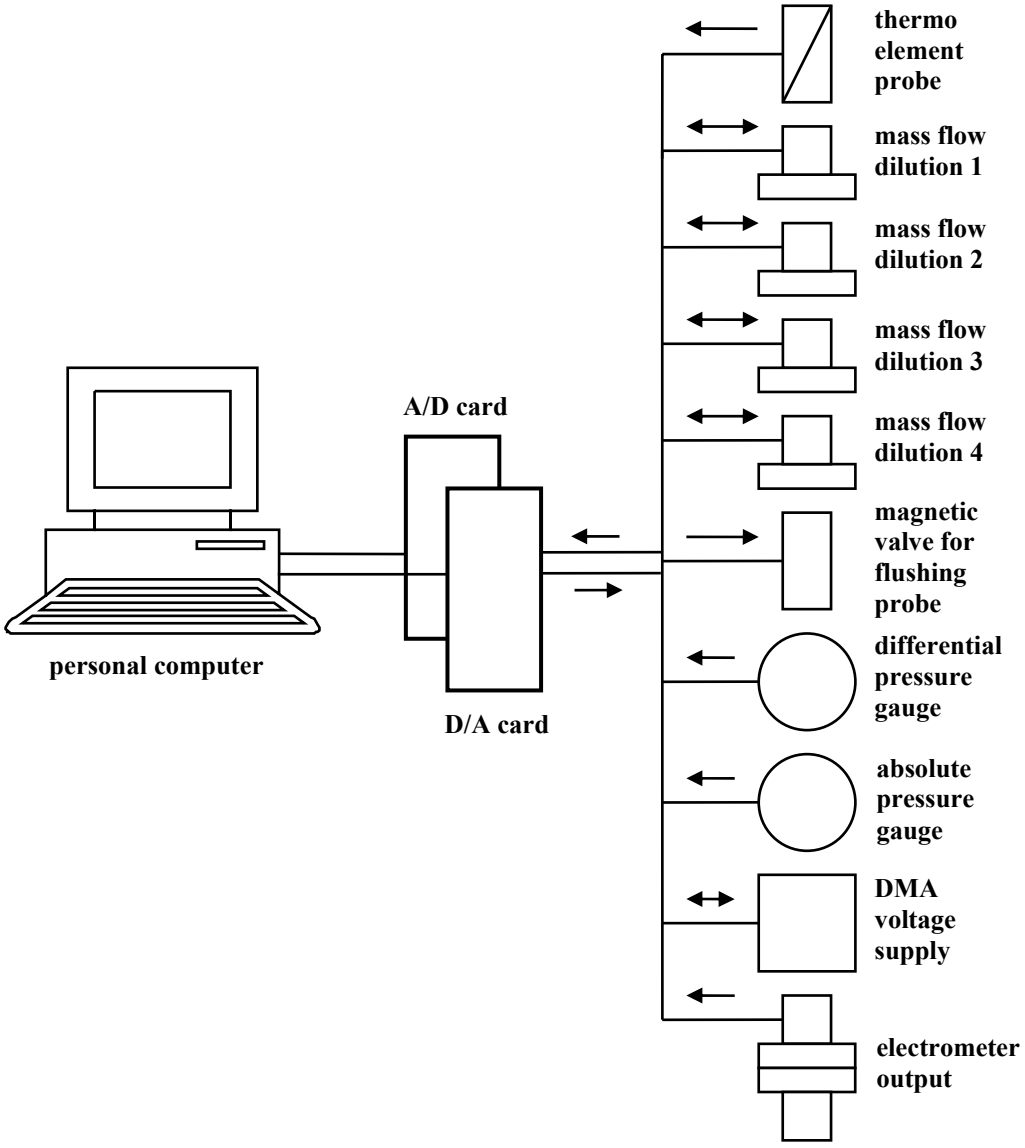

Figure A5.1: Block diagram of the electrical hardware of the LPDMPS

The IBM compatible personal computer has been equipped with an analogue output (D/A) and an analogue input (A/D) card. Each one has 16 channels and reads or writes voltages between -10V and +10V with a resolution of 16bit.

The A/D and D/A cards come with drivers for Microsoft Windows and C routines for the reading and writing of the several input- and output channels. These routines have been included to a C++ source code for the compilation to a computer program, which allows different adjustment like measurement range, resolution, etc., and which controls the measurement and calculates the number size distribution out of the electrometer raw data.

The temperature at the tip of the probe is measured by a thermo element at the entrance of the sampling probe. Although the probe temperature is not considered in the measurements and calculations, it has always been monitored to have an additional hint in case of malfunctioning of the system. In spite of the high temperature of the gas (up to 1400°), the temperature of the probe was always below 300°C due to the heat transfer of the metal and the nitrogen. The thermo element needs a special electrical transducer.

Four mass flow meters provide the dilution 1 to 3 and the clean gas flow of the DMA. For the mass flow controllers the set points are set and the actual values are monitored by the computer. A magnetic valve is used to flush the probe with nitrogen. The number and frequency of pulses can be changed in the program.

The differential and absolute pressure gages have 4mA - 20mA outputs. The currents are converted into 2-10V signals by precise 500Ω resistances.

The DMA needs a (high) voltage, which is provided by a commercially available high voltage supply. Its maximum voltage is 20KV. It is controlled by an input voltage from 0V to 10V. A built in voltage monitor output allows to monitor and record the actual DMA voltage. The voltage supply also has a current monitor output. The current is recorded because it indicates electrical breakthroughs due to a too high voltage.

Four d.c. voltage supplies provide -15V, 5V, 12V and 15V

A6 Circuit diagram of the LPDMPS

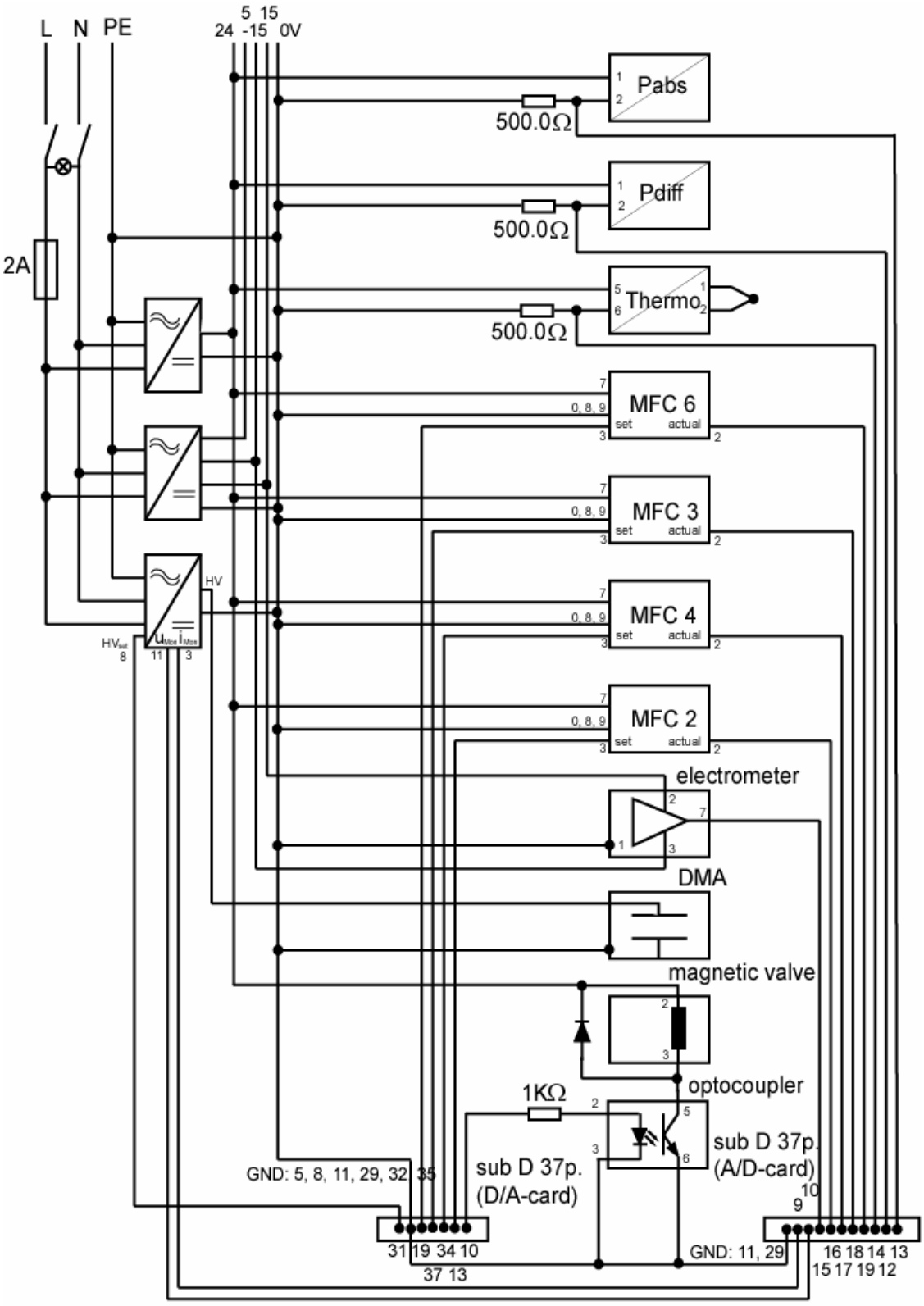

Figure A6.1: Circuit diagram of the LPDMPS

A7 List of components

power supply 1	Vero Monovolt PK120
power supply 2	Vero Trivolt PK60
power supply 3	Fug HCN 7E-20000
absolute pressure gauge	E+H PMC731-R32K1M22MD
differential pressure gauge	E+H PMD235-KBFA9EM3I
transmitter for thermoelement	Pepperl+Fuchs H-UT-Ex1
massflow controller MFC 6, 5l/min	Bronkhorst F-201D-FAB-00-P
massflow controller MFC 3, 20l/min	Bronkhorst F-201AC-FAB-00-P
massflow controller MFC 4, 100l/min	Bronkhorst F-202AC-FAB-00-P
massflow controller MFC 2, 5l/min	Bronkhorst F-201D-FAB-00-P
electrometer	University Duisburg
DMA	University Duisburg
magnetic valve	Bürkert W 33 LL
optocoupler	Weidmüller EGO4
D/A-card	Meilhaus PCI-6216V
A/D-card	Meilhaus PCI-9114HG
UV- irradiation unit	Matter type 990810

A8 Software

The control of the measurement sequence and the electrical components of the LPDMPS, for the recording of the several sensor signals and for the data inversion, a computer program has been developed. The program has been compiled using Microsoft Visual C++. It runs under Microsoft Windows. The main window of the program is shown in figure A8.1.

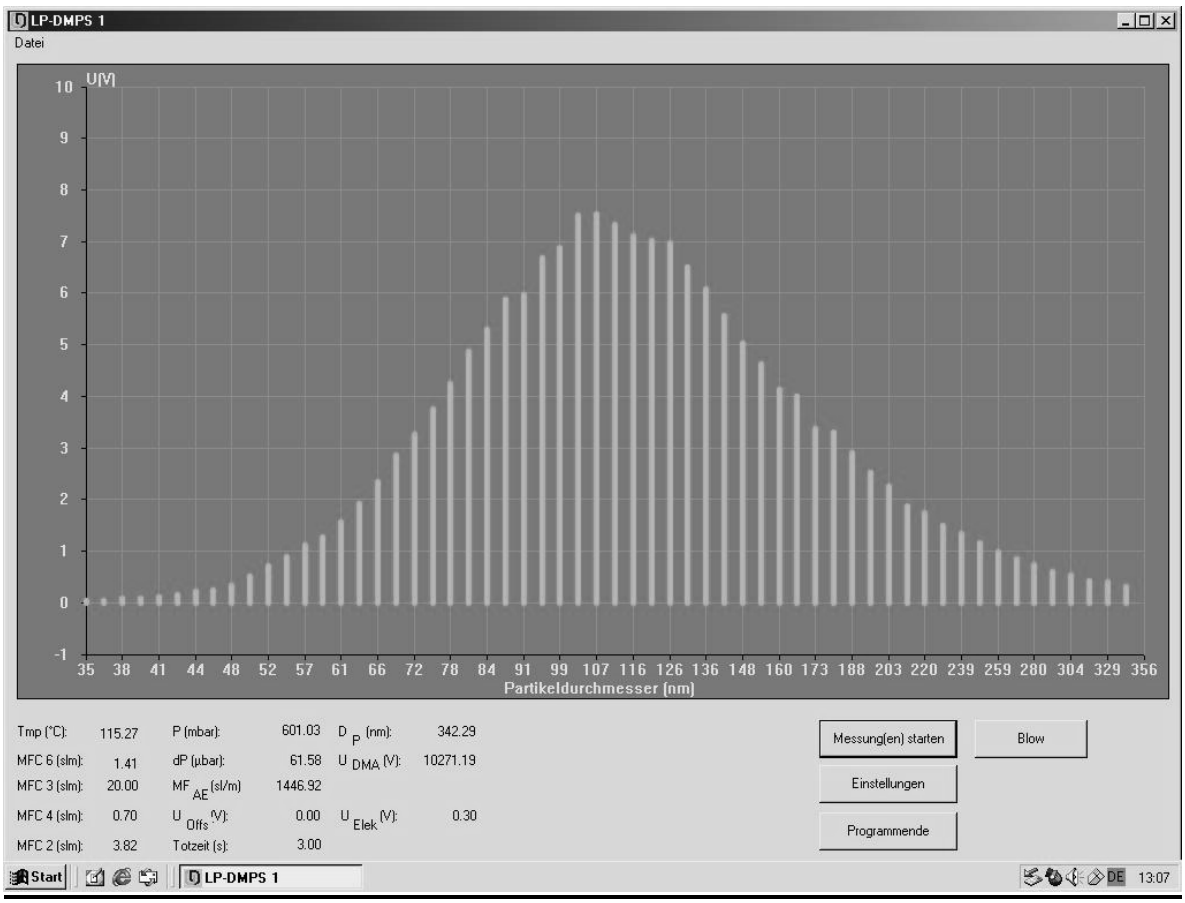

Figure A8.1: Main window of the program

The main window appears after the program has been started. It displays the current values for all measurement parameters. The electrometer output signal is graphically shown as a function of the particle size when a measurement has been started. All parameters and signals are stored in an Excel file. Figure A8.1 shows the main window after measurement in the size range 35nm to 350nm has just finished.

The adjustments button pops up a window where the operator can vary the particle size range of the measurement, the number of size channels, the volume flows, dead time, and number of values to be averaged.

The button “blow” causes the magnetic valve to flush the probe with nitrogen. The number and duration of pulses can be varied.

The buttons are locked as soon as a measurement has been started. Only the start button turns to a stop button and remains active.

At the beginning of each measurement the electrometer zero point is read. The number and particle sizes of the channels are calculated out of the values for the measurement size range and the size step width, which can be entered by the operator. The abscissa of the diagram is scaled to the chosen size range. After started the measurement, for each size channel the DMA voltage is calculated and applied, the dead time is awaited, and all parameters and signals are recorded. The electrometer signal is displayed on the screen.

For each particle size channel the DMA voltage is calculated according to the following procedure (see chapter 3.4):

1. The pressure p is read.
2. The mean free path λ between the gas molecules is calculated.
3. The actual clean gas mass flow is read.
4. The clean gas volume flow $\dot{V}_c$ is calculated.
5. The Cunningham slip correction C_C is calculated.
6. The DMA voltage is calculated and applied.

After the measurement has finished, the number size distribution is calculated taking into account the individual properties of charger, DMA, and electrometer.

A9 Results for DMA Transfer functions and exponential fits

The figures A9.1 to A9.4 give the range of measured values for experimentally determined widths β_{Zp} and heights α of the transfer function as a function of D_P. Each value has been measured 3 times. The bars indicate the range of the measured values. The dotted lines are the results of the exponential fit $\alpha_{Z_P}(D_P) = C_1 + C_2 \cdot \exp\left(-\frac{D_P[\text{nm}] + C_3}{C_4}\right)$ respectively $\beta_{Z_P}(D_P) = C_5 + C_6 \cdot \exp\left(-\frac{D_P[\text{nm}] + C_7}{C_8}\right)$. The constants for the exponential fits are listed in table A9.1 and A9.2.

Table A9.1: Constants of the exponential fits for $\alpha_{Zp}(D_P)$

p[mbar]	C_1	C_2	C_3	C_4
200	1.1440	-4.2715	9.8262	20.4794
400	1.3233	-1.7287	10.0041	52.4189
600	1.1760	-1.3852	10.0163	53.7815
1000	1.2187	-1.9278	9.9893	28.7868

Table A9.2: Constants of the exponential fits for $\beta_{ZP}(D_P)$

p[mbar]	C_5	C_6	C_7	C_8
200	0.2166	0.2695	0.0021	13.2495
400	0.1926	0.1560	0.0035	18.5729
600	0.2021	6.6053	-0.0200	4.0501
1000	0.2069	0.5634	-0.0052	13.5818

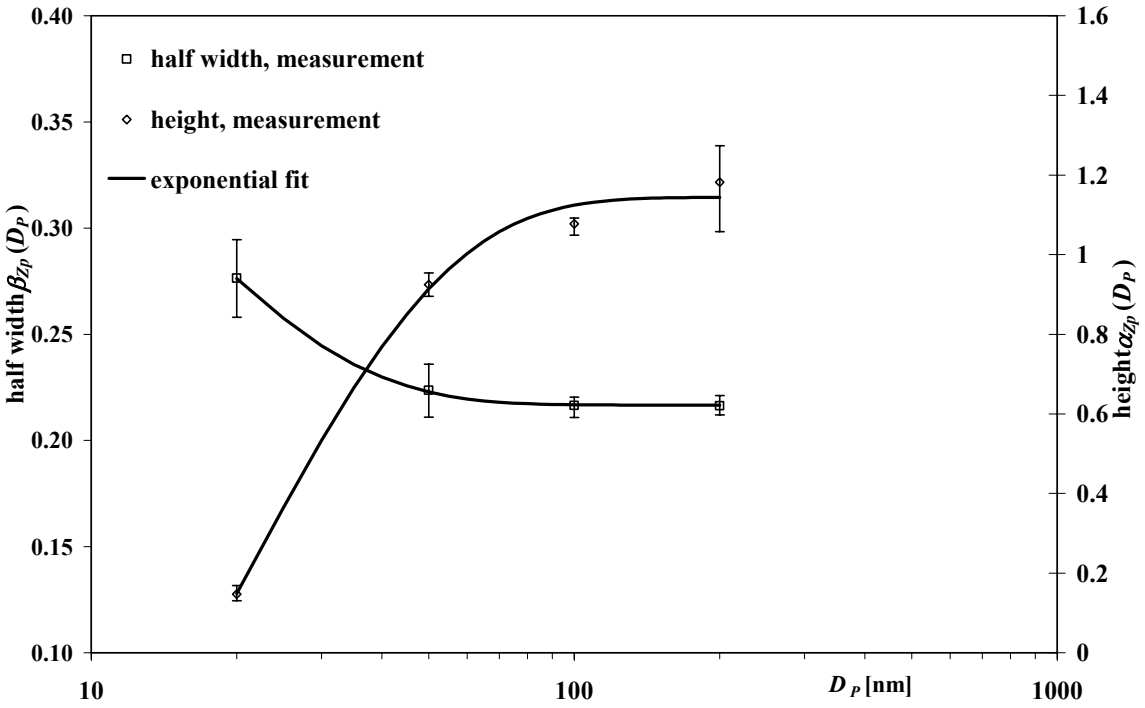

Figure A9.1: α_{Zp} and β_{Zp} as a function of D_P for p = 200mbar. The bars indicate the deviations of the single measurements from the mean value. The solid lines give the results for the exponential fits.

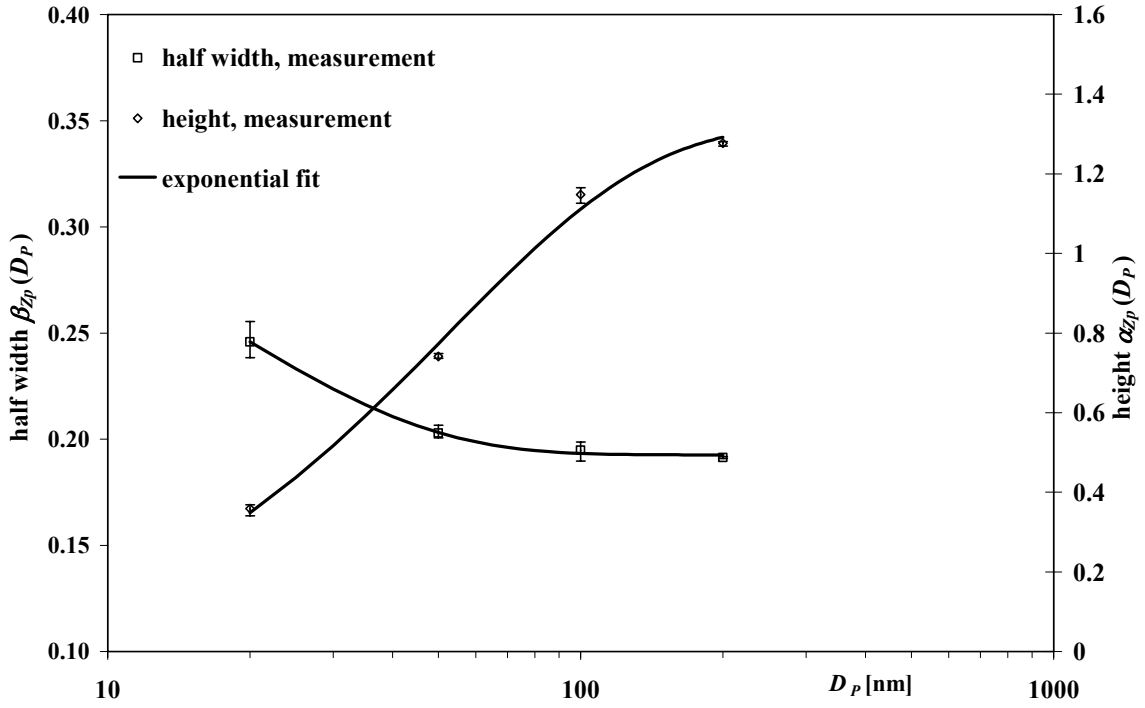

Figure A9.2: α_{Zp} and β_{Zp} as a function of D_P for p = 400mbar. The bars indicate the deviations of the single measurements from the mean value. The solid lines give the results for the exponential fits.

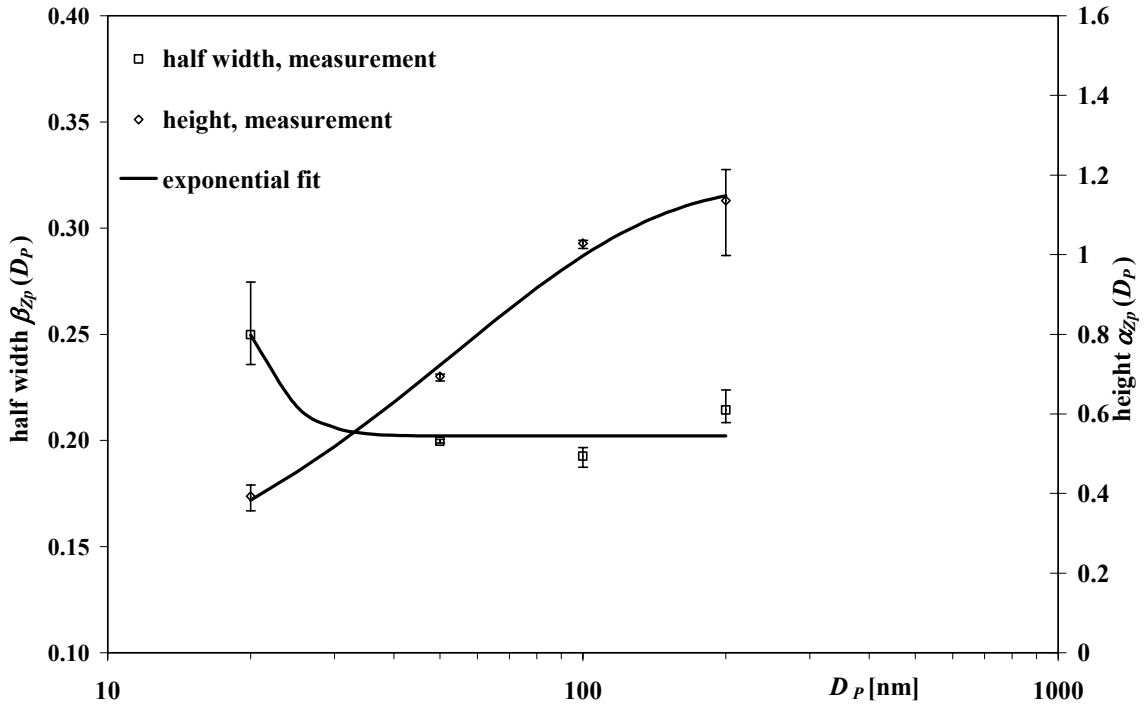

Figure A9.3: α_{Zp} and β_{Zp} as a function of D_P for p = 600mbar. The bars indicate the deviations of the single measurements from the mean value. The solid lines give the results for the exponential fits.

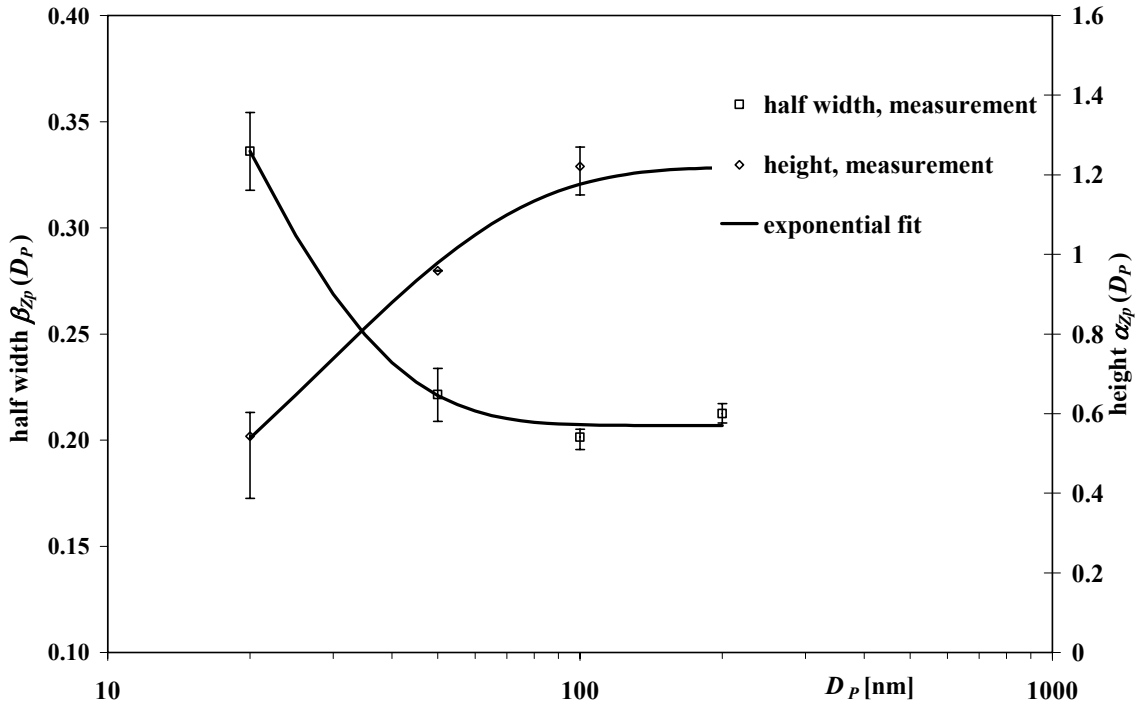

Figure A9.4: α_{Zp} and β_{Zp} as a function of D_P for p = 1000mbar. The bars indicate the deviations of the single measurements from the mean value. The solid lines give the results for the exponential fits.

A10 Photographs

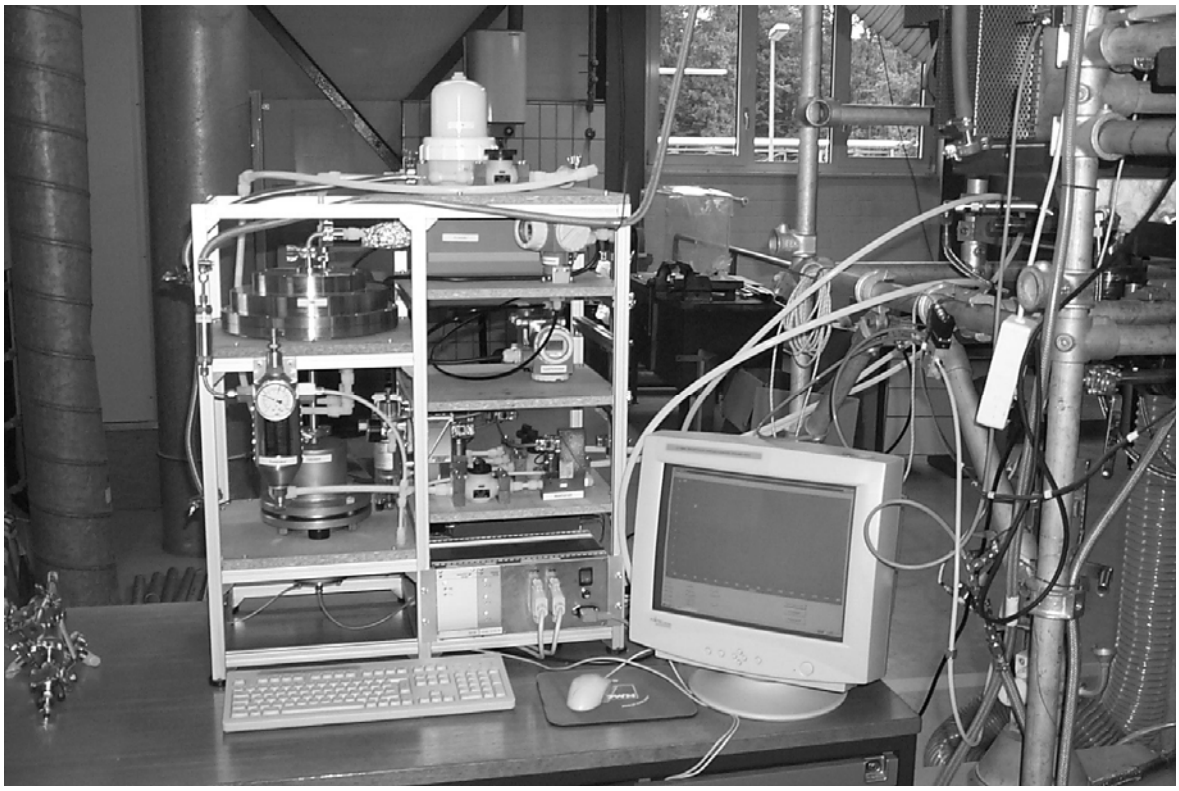

Figure A10.1: Photograph of the new LPDMPS

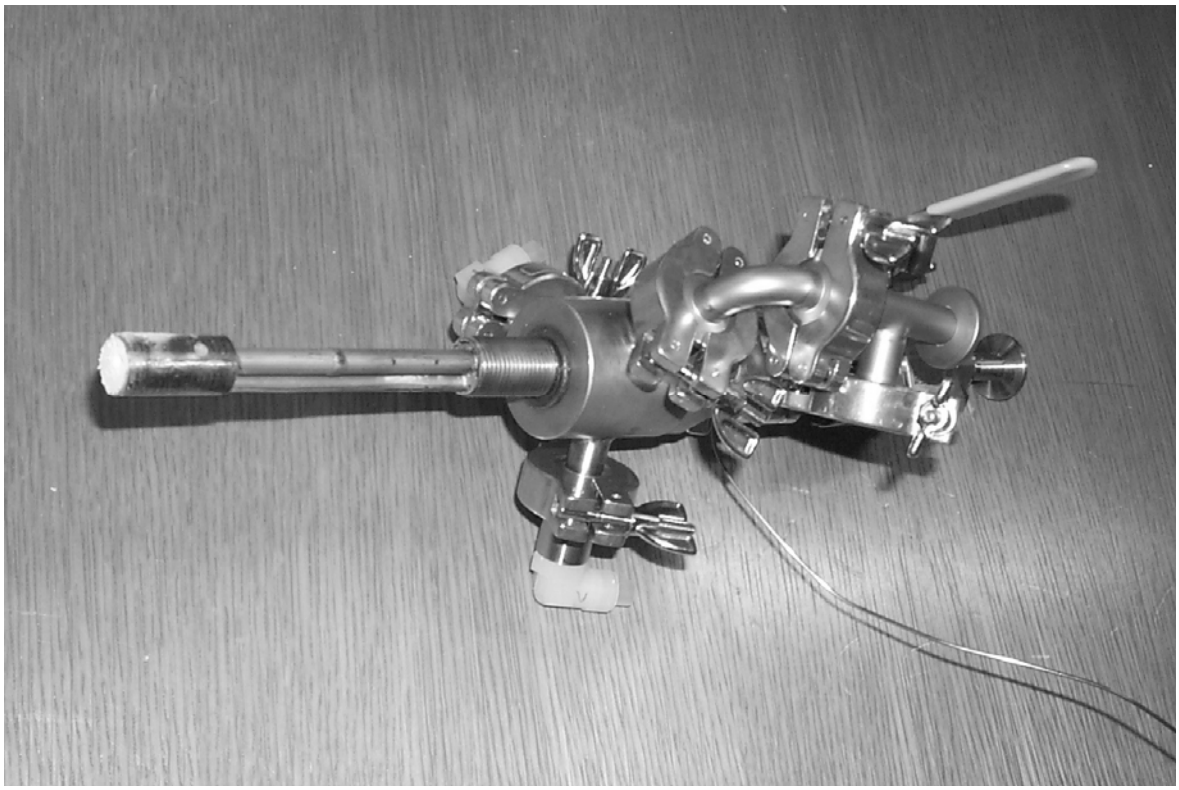

Figure A10.2: Photograph of the sampling probe

The tide rises, the tide falls

The tide rises, the tide falls,
The twilight darkens, the curlew calls;
Along the sea-sands damp and brown
The traveller hastens toward the town,
And the tide rises, the tide falls.

Darkness settles on roofs and walls,
But the sea in the darkness calls and calls;
The little waves, with their soft white hands,
Efface the footprints in the sands,
And the tide rises, the tide falls.

The morning breaks; the steeds in their stalls
Stamp and neigh, as the hostler calls;
The day returns, but nevermore
Returns the traveller to the shore,
And the tide rises, the tide falls.

Henry Wadsworth Longfellow, 1807 - 1882